

RWTH AACHEN UNIVERSITY

MASTER THESIS

---

# Automated Framework for EFT-Based Analyses of Resonant Leptoquark Production at the LHC

---

Author:

Tamilarasan Ketheeswaran

Supervisor:

Prof. Dr. Michael Krämer

Dr. Felix Wilsch

1st Examiner:

Prof. Dr. Michael Krämer

2nd Examiner:

Prof. Dr. Robert Harlander

A thesis submitted in fulfillment of the requirements  
for the degree of Master of Physics RWTH Aachen University

in the

Research Group Prof. Krämer

Institut für Theoretische Teilchenphysik und Kosmologie

October 15, 2025

“கற்றது கை மண் அளவு. கல்லாதது உலகளவு.”

- ஒளவெய்யார்

RWTH AACHEN UNIVERSITY

## *Abstract*

Fakultät für Mathematik, Informatik und Naturwissenschaften  
 Institut für Theoretische Teilchenphysik und Kosmologie

Master of Physics RWTH Aachen University

### **Automated Framework for EFT-Based Analyses of Resonant Leptoquark Production at the LHC**

by Tamilarasan Ketheeswaran

In this thesis, we present an automated framework for Effective Field Theory (EFT) analysis and apply it to leptoquarks (LQ) as a case study. To streamline the process, we developed an algorithm to automate the derivation of Feynman rules, implemented as an extension for MATCHETE. MATCHETE is a MATHEMATICA package used for matching effective field theories. Having both the matching and the generation of Feynman rules in one package significantly simplifies the analysis of BSM models and their EFTs by eliminating the need for intermediate steps. After exporting the Feynman rules to the Universal Feynman Output (UFO) format, they can be used in Monte Carlo generators, such as MADGRAPH5\_AMC@NLO. Additionally, we discuss the implementation of electroweak symmetry breaking in MATCHETE for the LQ model and the SMEFT at dimension 6, which is crucial for deriving Feynman rules in the broken phase of the theory.

We demonstrate this EFT analysis framework for the scalar leptoquark  $\tilde{S}_1 \sim (\bar{3}, 1, 4/3)$  coupling to bottom quarks ( $b$ ) and tau leptons ( $\tau$ ), by comparing BSM and EFT cross sections for the hadronic processes  $pp \rightarrow \tau\tau$  and  $pp \rightarrow \tau\tau b$ , and assessing the EFT validity across different values of the leptoquark coupling and over the mass range  $1 - 10$  TeV.



# Contents

<b>Abstract</b>	<b>iii</b>
<b>Introduction</b>	<b>1</b>
<b>1 From the Standard Model to New Physics</b>	<b>3</b>
1.1 The Standard Model . . . . .	3
1.2 Effective Field Theory . . . . .	4
1.3 Standard Model Effective Field Theory . . . . .	7
<b>2 MATCHETE: Matching Effective Theories Efficiently</b>	<b>9</b>
2.1 Toy Model: Implementation in MATCHETE . . . . .	9
2.2 Toy Model: Deriving the EFT . . . . .	10
2.3 Toy Model: Deriving Feynman Rules . . . . .	11
2.4 General Procedure to derive Feynman Rules . . . . .	16
2.5 The <code>FeynmanRules</code> Algorithm . . . . .	18
<b>3 Scalar Leptoquark <math>\tilde{S}_1</math></b>	<b>19</b>
3.1 Hints towards New Physics . . . . .	19
3.2 Theory and Definition . . . . .	19
3.3 MATCHETE: Model Definition and Matching . . . . .	22
3.4 Feynman Rules for $\tilde{S}_1$ . . . . .	24
<b>4 Scalar Leptoquark <math>\tilde{S}_1</math>: EFT and BSM convergence</b>	<b>27</b>
4.1 MG5 Settings . . . . .	28
4.2 Overview of Hadronic Interactions and Validation with ATLAS . . . . .	32
4.3 Hadronic Interaction without a final state $b$ -quark: $pp \rightarrow \tau^+\tau^-$ . . . . .	34
4.4 Hadronic Interaction with one final state $b$ -quark: $pp \rightarrow \tau^+\tau^- b$ . . . . .	45
<b>Conclusion</b>	<b>59</b>
<b>Acknowledgements</b>	<b>61</b>

<b>A The FeynmanRules Algorithm</b>	<b>63</b>
A.1 Step 1: Preprocess . . . . .	64
A.2 Step 2: Filter by Field Content . . . . .	67
A.3 Step 3: Combinatorics . . . . .	68
A.4 Step 4: Indices and Contraction . . . . .	72
<b>B MATCHETE: Electroweak Symmetry Breaking for <math>\tilde{S}_1</math></b>	<b>73</b>
B.1 EWSB in the Standard Model . . . . .	73
B.2 EWSB in the Standard Model EFT . . . . .	77
B.3 Generating the UFO Files . . . . .	79
<b>C Scalar Leptoquark <math>\tilde{S}_1</math>: EFT and BSM convergence</b>	<b>81</b>
C.1 Hadronic Interaction without a final $b$ -quark: $pp \rightarrow \tau^+ \tau^-$ . . . . .	82
C.2 Hadronic Interaction with one final state $b$ -quark: $pp \rightarrow \tau^+ \tau^- b$ . . . . .	85
<b>D Numerical Stability of Monte Carlo Simulations</b>	<b>89</b>
<b>Bibliography</b>	<b>93</b>

# List of Abbreviations

<b>BSM</b>	Beyond the Standard Model
<b>EFT</b>	Effective Field Theory
<b>EWSB</b>	Electroweak Symmetry Breaking
<b>IR</b> -Theory	Infrared-Theory
<b>LQ</b>	Lepto-Quark
<b>LFU</b>	Lepton Flavor Universality
<b>LHC</b>	Large Hadron Collider
<b>MG5</b>	<b>MADGRAPH5_AMC@NLO</b>
<b>SLQ</b>	Scalar Lepto-Quark
<b>SM</b>	Standard Model
<b>SMEFT</b>	Standard Model Effective Field Theory
<b>SSB</b>	Spontaneous Symmetry Breaking
<b>UFO</b>	Universal Feynman Output
<b>UV</b> -Theory	Ultraviolet-Theory
<b>5FS</b>	5 Flavor Scheme



*Dedicated to my Family*



# Introduction

The Standard Model (SM) of particle physics provides a remarkably successful description of phenomena across a wide range of energies. Nevertheless, it leaves several fundamental questions unanswered, such as the origin of neutrino masses, the nature of dark matter, and the baryon asymmetry in the Universe. These open issues motivate the search for physics beyond the Standard Model (BSM). In the current absence of new particle resonances or experimental signatures, the scale at which new physics (NP) appears is expected to lie beyond the reach of present collider experiments.

Rather than focusing on specific BSM models, one can adopt a model-independent framework based on effective field theories (EFTs). This approach enables us to capture the low-energy effects of NP at experimentally accessible scales. Every EFT-based analysis begins with the construction of an appropriate EFT. To this end, Chapter 1 provides a brief overview of the SM and outlines the principles to construct an EFT. We then discuss how the SM can be systematically extended within this framework.

For quantitative studies, EFT analyses rely on numerical simulations of cross sections, which can be performed using Monte Carlo tools such as `MADGRAPH5_AMC@NLO` (MG5) [1, 2]. These tools require the theoretical model to be provided in the Universal Feynman Output (UFO) format [3], which contains, among other parameters and definitions, the Feynman rules derived from the theory. The standard approach is to employ `FEYNRULES` [4], a `MATHEMATICA`-based package that automates the generation of UFO files from a given Lagrangian. However, `FEYNRULES` exhibits limitations when dealing with EFTs, particularly in the computation of higher-dimensional operators.

The EFT analysis presented in this thesis aims to investigate EFT validity by comparing simulated cross sections obtained from both the BSM and EFT models. We make use of `MATCHETE`, a `MATHEMATICA` package that performs matching between BSM Lagrangians to their corresponding EFTs [5]. In the current workflow, the BSM theory is first matched to its EFT using `MATCHETE`. The Feynman rules for both the EFT and BSM theories are then generated via `FEYNRULES` and subsequently exported to MG5. However, the intermediate step involving `FEYNRULES` is tedious and motivates the development of a more direct approach.

To address this, in Chapter 2 we develop an extension of `MATCHETE` that computes the Feynman rules directly from the matched BSM and EFT theories. This improvement eliminates the need for the intermediate step, thereby simplifying the overall workflow. The

second part of this thesis demonstrates this new framework through a dedicated case study. Specifically, we apply the workflow to a scalar leptoquark (LQ)  $\tilde{S}_1 \sim (\bar{3}, 1, 4/3)$  [6]. In Chapter 3.1, we give an overview of the theoretical background of the  $\tilde{S}_1$  and its implementation in MATCHETE. The Feynman rules are also validated against the rules generated by FEYNRULES [6].

Finally, in Chapter 4, we present the results of the MG5 simulations for the hadronic processes  $pp \rightarrow \tau\tau$  and  $pp \rightarrow \tau\tau b$ . We conduct a convergence study of EFTs truncated at dimensions six and eight, comparing them to the BSM model. To this end, we quantify the region of validity of the EFTs by analyzing the differences arising from matching order and the impact of varying leptoquark couplings and masses.

# Chapter 1

# From the Standard Model to New Physics

## 1.1 The Standard Model

The Standard Model (SM) is a quantum field theory that describes the strong, weak, and electromagnetic interactions of all known fundamental particles. The gauge group of the SM  $G_{SM}$  is given by

$$SU(3)_C \times SU(2)_L \times U(1)_Y.$$

Here  $SU(3)_C$  is the gauge group of quantum chromodynamics (QCD) and  $SU(2)_L \times U(1)_Y$  is the electroweak (EW) sector. The matter fields in the SM consist of three flavour generations of quarks and leptons [7, 8]:

- **Quarks:** Left-handed doublets  $q_{iL} = \begin{pmatrix} u_i \\ d_i \end{pmatrix}_L$  and right-handed singlets  $u_{iR}, d_{iR}$ .
- **Leptons:** Left-handed doublets  $\ell_{iL} = \begin{pmatrix} \nu_i \\ e_i \end{pmatrix}_L$  and right-handed singlets  $e_{iR}$ .

where  $i = 1, 2, 3$  is the generation index. The SM also includes:

- **Gauge bosons:**

$$- G_\mu^a \text{ for } SU(3)_C \quad - W_\mu^i \text{ for } SU(2)_L \quad - B_\mu \text{ for } U(1)_Y$$

- **Higgs boson:** Scalar field  $\phi$  responsible for electroweak symmetry breaking (EWSB) and mass generation.

After EWSB, the  $W_\mu^i$  and  $B_\mu$  bosons mix to give:

- $W^\pm$  and  $Z$  bosons (massive)
- Photon  $\gamma$  (massless)

With the fields above, the SM Lagrangian can be written as:

$$\mathcal{L}_{\text{SM}} = \mathcal{L}_{\text{gauge}} + \mathcal{L}_{\text{fermion}} + \mathcal{L}_{\text{Higgs}} + \mathcal{L}_{\text{Yukawa}}. \quad (1.1)$$

Here, the gauge sector is given by

$$\mathcal{L}_{\text{gauge}} = -\frac{1}{4}G_{\mu\nu}^a G^{a\mu\nu} - \frac{1}{4}W_{\mu\nu}^i W^{i\mu\nu} - \frac{1}{4}B_{\mu\nu} B^{\mu\nu}, \quad (1.2)$$

where  $G_{\mu\nu}^a$ ,  $W_{\mu\nu}^i$ , and  $B_{\mu\nu}$  are the field strength tensors for  $SU(3)_C$ ,  $SU(2)_L$ , and  $U(1)_Y$  respectively. The fermion sector is

$$\mathcal{L}_{\text{fermion}} = \sum_{\psi} \bar{\psi} i\gamma^\mu D_{(\psi)\mu} \psi, \quad (1.3)$$

where the sum runs over all quark and lepton fields.  $D_{(\psi)\mu}$  is the covariant derivative of the field  $\psi$ . The Higgs sector is defined as

$$\mathcal{L}_{\text{Higgs}} = (D_\mu \phi)^\dagger (D^\mu \phi) - V(\phi), \quad V(\phi) = -\mu^2 \phi^\dagger \phi + \lambda (\phi^\dagger \phi)^2, \quad (1.4)$$

where  $\lambda > 0$ . Lastly, the Yukawa sector is given by

$$\mathcal{L}_{\text{Yukawa}} = -y_u^{ij} \bar{q}_{iL} \tilde{\phi} u_{jR} - y_d^{ij} \bar{q}_{iL} \phi d_{jR} - y_e^{ij} \bar{\ell}_{iL} \phi e_{jR} + \text{h.c.}, \quad (1.5)$$

where  $\tilde{\phi} = i\sigma_2 \phi^*$ , and  $y_{u,d,e}^{ij}$  are the Yukawa matrices responsible for fermion mass generation after electroweak symmetry breaking.

## 1.2 Effective Field Theory

Effective Field Theories (EFTs) rest on a separation of scales: when observables probe energies  $E$  far below a heavy threshold  $\Lambda$  (i.e.  $E \ll \Lambda$ ), the detailed dynamics of heavy fields need not be resolved. Or, to put it differently, if we have interactions involving light and heavy fields and the energy is much lower than the heavy field's mass, we can describe the effects of the heavy fields on the light fields without including the heavy fields explicitly in the description.

As an illustrative example, we can consider Fermi's theory of the weak interaction [9]. Using Fermi's theory of the weak interaction, the muon decay  $\mu^- \rightarrow e^- \bar{\nu}_e \nu_\mu$  can be explained via a four-fermion vertex, in which the muon decays into  $e^- \bar{\nu}_e \nu_\mu$ . Today, however, we know that the  $Z$ ,  $W^\pm$  bosons are the mediators of the weak interaction, and the muon decay, in fact, is correctly described via the exchange of the  $W^-$  boson [10]. The question now arises: how is Fermi's theory able to make such accurate predictions?

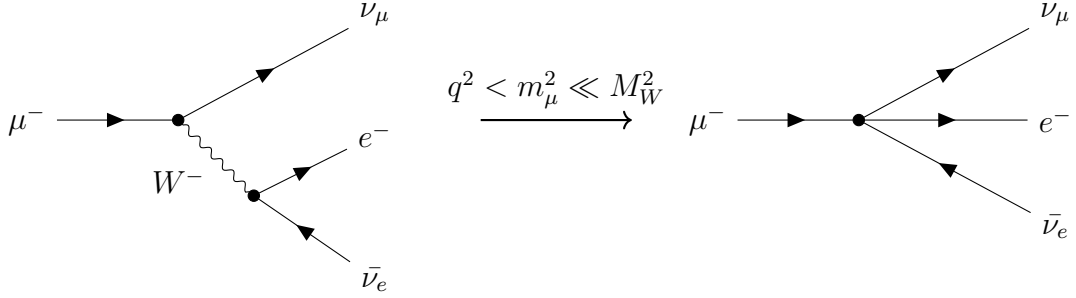


FIGURE 1.1: Feynman diagram of  $\mu^-$  decay. Theory including  $W^-$  (left) and Fermi’s theory (right)

To answer lies in Figure 1.1, where we show the description of the full theory on the left-hand side, including the heavy field  $W^-$ , and on the right-hand side the description via Fermi’s theory. From momentum conservation, it is obvious that the four-momentum of the initial muon is split between the  $W^-$  and the  $\nu_\mu$ . Suppose the four-momentum of the  $W^-$  is  $q_\alpha$ , then  $q^2 < m_\mu^2$ . At the same time, we know the propagator of the  $W^-$  scales as

$$\propto \frac{1}{q^2 - M_W^2}.$$

Given the ratio  $m_\mu^2/M_W^2 \sim 10^{-6}$ , as per [10], we can infer that the ratio  $q^2/M_W^2$  must be of the same order or even smaller. Therefore, we can expand the fraction above as

$$-\frac{1}{M_W^2} \left( \frac{1}{1 - q^2/M_W^2} \right) \approx -\frac{1}{M_W^2} \quad (1.6)$$

and truncate at the lowest order. In principle, this corresponds to reducing the degrees of freedom of the heavy  $W^-$  boson, as the propagator corresponds to a single constant. This then corresponds to a contact interaction as shown on the right-hand side in Figure 1.1. The next order of the expansion would be of order  $\sim 10^{-6}$  relative to the leading order, which is why Fermi’s theory is accurate enough to be verified experimentally.

It is evident that this description only works as long as  $q^2 \ll M_W^2$ . If the energy scale approaches the mass of the heavy field, the expansion breaks, and we need to include the degree of freedom associated with the  $W^-$  field.

Next, we discuss how an EFT is constructed in general.

### 1.2.1 Constructing an EFT

There are two main strategies to construct an EFT: the *top-down* and the *bottom-up* approach [9, 11].

In the **top-down** approach, the ultraviolet (UV) theory is known. To construct an EFT of the UV theory, the procedure is as follows:

1. **Identifying the relevant degrees of freedom.** Specify which particles remain dynamical at the energy scale of interest. Heavy particles are integrated out, and their effects are encoded as higher-dimensional contact interactions among the light fields.

If, however, the UV theory is unknown and we want to construct a model-independent framework, we employ the **bottom-up** approach:

1. **Specify the symmetries.** The effective Lagrangian must respect all symmetries expected to hold at low energies, including Lorentz invariance, gauge symmetries, and possibly approximate global symmetries such as flavour or custodial symmetry.
2. **Write down all allowed operators.** Construct all possible operators built from the light fields and consistent with these symmetries, organized in an expansion in mass dimension:

$$\mathcal{L}_{\text{EFT}} = \mathcal{L}_{\text{ren}} + \sum_i \frac{C_i^{(5)}}{\Lambda} \mathcal{O}_i^{(5)} + \sum_j \frac{C_j^{(6)}}{\Lambda^2} \mathcal{O}_j^{(6)} + \dots, \quad (1.7)$$

where  $\mathcal{L}_{\text{ren}}$  contains all renormalizable terms (dimension  $\leq 4$ ), and  $\mathcal{O}_i^{(d)}$  are higher-dimensional operators of mass dimension  $d > 4$ , with Wilson coefficients  $C_i^{(d)}$  encoding the effects of heavy physics in a model-independent way. The Wilson coefficients remain free parameters to be constrained by experiments.

After integrating out the heavier particles or enumerating all possible operators, redundancies may remain. These operator redundancies can be removed using integration by parts, field redefinitions, equations of motion, Fierz identities, and Dirac structure reduction [11].

When working with EFTs, several key aspects should be kept in mind:

- EFTs are valid only below the cutoff scale  $\Lambda$ . As energies approach  $\Lambda$ , heavy degrees of freedom become relevant, and the EFT description breaks down.
- Although non-renormalizable, EFTs remain predictive: higher-dimensional operators are suppressed by powers of  $\Lambda$ , making the theory effectively renormalizable order by order in the expansion.
- All operators consistent with the symmetries should, in principle, be included, since renormalization group (RG) evolution can generate additional operators through mixing even if they are absent at the matching scale.

- EFTs are insensitive to the detailed structure of the UV theory. Different UV completions can produce the same operator basis but with distinct correlations among the Wilson coefficients, leading to potential UV-IR degeneracies.

EFTs thus provide a systematic framework for studying low-energy phenomena of UV theories. In what follows, we will employ the *bottom-up* approach to promote the SM to the Standard Model effective field theory (SMEFT), and later use the *top-down* approach to match a leptoquark (LQ) model onto it.

## 1.3 Standard Model Effective Field Theory

Starting from the SM as the IR limit of a UV theory, we first identify the relevant degrees of freedom, namely the SM fields. We then assume that the EFT respects the SM gauge symmetry  $G_{SM}$  and that EWSB is realized linearly. Furthermore, the cutoff scale  $\Lambda$  is assumed to be well above the electroweak scale,  $\Lambda \gg \Lambda_{EW} \sim 10^2$  GeV. The EFT extension of the SM can then be expressed as

$$\mathcal{L}_{\text{SMEFT}}(\psi, H, A) = \mathcal{L}_{\text{SM}}(\psi, H, A) + \sum_{d=5}^{\infty} \frac{1}{\Lambda^{d-4}} \sum_{i=1}^{n_d} C_i^{(d)} Q_i^{(d)}(\psi, H, A), \quad (1.8)$$

where  $\psi$ ,  $H$ , and  $A$  denote SM fermions, Higgs, and gauge fields, respectively. By convention, the  $C_i^{(d)}$  are taken dimensionless. In practical applications, we truncate the sum above at a certain order  $d$  and work in a complete, non-redundant operator basis [11].

**Operators at Dimension 5 and 6:** At dimension  $d = 5$ , after removing redundancies, only a single operator remains (the Weinberg operator), which, after electroweak symmetry breaking, generates Majorana masses for left-handed neutrinos [12]. At  $d = 6$ , a larger but finite set arises. As pointed out by Grzadkowski *et al.* [13], the number of operators at dimension six can be reduced to 59 operators that conserve baryon and lepton number.

See Isidori, Wilsch, and Wyler [11] for a comprehensive introduction to SMEFT.



## Chapter 2

# MATCHETE: Matching Effective Theories Efficiently

Central to this thesis is the development of a tool that derives Feynman rules efficiently using the MATCHETE framework [5]. MATCHETE is a MATHEMATICA package that performs one-loop matching. For a comprehensive introduction to MATCHETE, we refer to [5]. This chapter outlines the relevant features of MATCHETE using a simple model consisting of a heavy scalar field and a multiplet of light scalar fields.

## 2.1 Toy Model: Implementation in Matchete

The model consists of a single real heavy scalar field  $\Phi$  coupled to a multiplet of light real scalar fields  $\phi^a$  labelled by flavour  $a = 1, 2, 3$ .

The UV Lagrangian contains the kinetic and mass terms for the light and heavy scalars, together with the interaction that is linear in the heavy field:

$$\mathcal{L}_{\text{UV}} = \underbrace{\frac{1}{2}(\partial_\mu \phi^a)^2 - \frac{1}{2}m^2 \phi^a \phi^a}_{\mathcal{L}_\phi} + \underbrace{\frac{1}{2}(\partial_\mu \Phi)^2 - \frac{1}{2}M^2 \Phi^2}_{\mathcal{L}_\Phi} - g \underbrace{\phi^a \Phi}_{\mathcal{L}_{\text{int}}} . \quad (2.1)$$

where  $m \ll M$  and  $g$  a real coupling constant. To implement this model in MATCHETE, we first define the flavour Flavour and the fields  $\phi, \Phi$ :

```
In[2]:= DefineFlavorIndex[Flavour, 3, IndexAlphabet -> {"a", "b", "c"}];
DefineField[\phi, Scalar, Indices -> Flavour, Mass -> {Light, m},
            SelfConjugate -> True];
DefineField[\Phi, Scalar, Mass -> {Heavy, M}, SelfConjugate -> True];
```

Now using the `FreeLag[]` routine, we can generate the free Lagrangians of the fields:

```
In[3]:= Lphi = FreeLag[\phi];
```

```
In[4]:= LPhi = FreeLag[\Phi];
```

Next, we define the coupling constant  $g$

```
In[5]:= DefineCoupling[g, SelfConjugate -> True];
```

and the interaction term by

```
In[6]:= Lint = -g[]*\phi[a]^2*\Phi[];
```

Putting all terms together, we have implemented Equation (2.1) in MATCHETE

```
In[7]:= LUV = Lphi + LPhi + Lint;
```

## 2.2 Toy Model: Deriving the EFT

To derive the EFT, at tree level, the heavy field can be eliminated using its classical equation of motion derived from Equation (2.1) [14]:

$$(\square + M^2)\Phi = -g(\phi^a\phi^a). \quad (2.2)$$

Expanding for  $E \ll M$  (with  $\square = \partial^2 \sim p^2 \sim E^2$ ) gives

$$\Phi = -\frac{g}{M^2}(\phi^a\phi^a) + \frac{g}{M^4}\square(\phi^a\phi^a) + \mathcal{O}(M^{-6}). \quad (2.3)$$

Inserting Equation (2.3) into Equation (2.1) and making use of IbP relations, we find

$$\mathcal{L}_{\text{EFT}} = \frac{1}{2}(\partial_\mu\phi^a)^2 - \frac{1}{2}m^2\phi^{a2} + \frac{g^2}{2M^2}\phi^{a2}\phi^{b2} + 2\frac{g^2}{M^4}(\phi^a\partial_\mu\phi^a)(\phi^b\partial_\mu\phi^b) + \mathcal{O}\left(\frac{1}{M^6}\right). \quad (2.4)$$

Since  $[g] = [M] = 1$  and  $[\phi^a] = 1$ , the operator proportional to  $g^2/M^4$  has dimension four and is therefore renormalisable. The term  $\sim (\phi^a\partial_\mu\phi^a)(\phi^b\partial_\mu\phi^b)$  is of mass-dimension six, so the term proportional to  $g^2/M^4$  represents the EFT at dimension  $d = 6$ .

The matching can be performed automatically with MATCHETE's `Match` routine, offering a convenient alternative to the analytic derivation.

```
In[8]:= LEFT = Match[LUV, LoopOrder -> 0, EFTOrder -> 6]//NiceForm
```

```
Out[8]= 
$$\frac{1}{2}(\partial_\mu\phi^a)^2 - \frac{1}{2}m^2\phi^{a2} + \frac{1}{2}g^2\frac{1}{M^2}\phi^{a2}\phi^{b2} + 2g^2\frac{1}{M^4}\phi^a\partial_\mu\phi^a\phi^b\partial_\mu\phi^b$$

```

This coincides precisely with the Equation (2.4). The arguments `LoopOrder` specify the loop order, and `EFTOrder` the order in the power counting of the EFT to which matching is performed.

## 2.3 Toy Model: Deriving Feynman Rules

This chapter presents how Feynman rules can be derived using the path integral approach, as outlined in [15].

To demonstrate the procedure, the derivation is carried out using the example of the four-point scalar vertex from the toy model Lagrangian in Equation (2.4).<sup>1</sup> The interaction term

$$\mathcal{L}_{\text{int}} = +\frac{g^2}{2M^2} \phi^{a2} \phi^{b2} \equiv -\lambda \phi^{a2} \phi^{b2}, \quad \text{with } \lambda \equiv -\frac{g^2}{2M^2}, \quad (2.5)$$

leads to the following Feynman diagram:

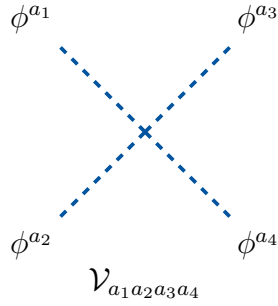


FIGURE 2.1: Quartic scalar contact interaction from  $\lambda(\phi^a \phi^a)(\phi^b \phi^b)$  with vertex  $\mathcal{V}_{a_1 a_2 a_3 a_4}$ .

### Free Action

To derive the Feynman rules, we start with the free action of the real scalar multiplet  $\phi_a$

$$S_0 = \sum_{a=1}^3 \frac{1}{2} \int d^4x \phi_a(x) \left( -\square - m^2 + i\epsilon \right) \phi_a(x). \quad (2.6)$$

This can be rewritten as

$$S_0 = \frac{1}{2} \int d^4x \int d^4y \phi_a(x) \left( -\square_x - m^2 + i\epsilon \right) \delta^{(4)}(x-y) \delta_{ab} \phi_b(y), \quad (2.7)$$

where the sum over repeated indices is implicit. The propagator  $D(x-y)$  (Green's function) is defined as

$$\begin{aligned} \left( -\square_x - m^2 + i\epsilon \right) D_{ab}(x-y) &= i \delta^{(4)}(x-y) \delta_{ab} \\ iD_{ab}^{-1}(x-y) &= \left( -\square_x - m^2 + i\epsilon \right) \delta^{(4)}(x-y) \delta_{ab}. \end{aligned} \quad (2.8)$$

---

<sup>1</sup>We restrict ourselves to the renormalisable part, i.e., the interaction term without the derivatives.

Therefore, we have

$$S_0 = \frac{1}{2} \int d^4x \int d^4y \phi_a(x) iD^{-1}(x-y) \delta_{ab} \phi_b(y), \quad (2.9)$$

or in shorthand notation

$$iS_0 = -\frac{1}{2} \phi_a D^{-1} \phi_a. \quad (2.10)$$

### Free Generating Functional

Next, we move to the calculation of the free generating functional  $Z_0[J]$ . For that, we first define the functional integral measure for the three-component real scalar multiplet  $\phi = (\phi^1, \phi^2, \phi^3)$  as:

$$\mathcal{D}\phi \equiv \prod_{a=1}^3 \mathcal{D}\phi^a.$$

With the expression for the free action  $S_0$ , the free generating functional  $Z_0[J]$  is given by

$$Z_0[J] = \int \mathcal{D}\phi \exp \left\{ -\frac{1}{2} \phi_a D^{-1} \phi_a + i J_a \phi_a \right\}, \quad (2.11)$$

where  $i J_a \phi_a$  is shorthand notation for

$$i J_a \phi_a \equiv i \int d^4x J_a(x) \phi_a(x). \quad (2.12)$$

Now shifting  $\phi_a$  by

$$\phi_a(x) \longrightarrow \phi_a(x) + i \int d^4y D_{ab}(x-y) J_b(y) \equiv \phi_a + i(DJ)_a, \quad (2.13)$$

leaves us with

$$Z_0[J] = \int \mathcal{D}\phi \exp \left\{ -\frac{1}{2} \phi_a D^{-1} \phi_a - \frac{1}{2} J_a (DJ)_a \right\}, \quad (2.14)$$

where

$$J_a (DJ)_a = \int d^4x \int d^4y J_a(x) D_{ab}(x-y) J_b(y). \quad (2.15)$$

Since the  $\frac{1}{2} J_a (DJ)_a$  does not depend on the field  $\phi$ , it can be moved out of the integral. This way, the free generating functional can be written as

$$Z_0[J] = Z_0[0] \exp \left\{ -\frac{1}{2} J_a (DJ)_a \right\}. \quad (2.16)$$

### Generating Functional including Interaction Term

The generating functional  $Z[J]$ , including the interaction term is given by

$$Z[J] = \int \mathcal{D}\phi \exp \{iS_0[\phi] + iS_{\text{int}}[\phi] + iJ_d\phi_d\}, \quad (2.17)$$

where

$$S_{\text{int}} = \int d^4x \mathcal{L}_{\text{int}} = -\lambda \int d^4x \phi_a^2 \phi_b^2. \quad (2.18)$$

As  $\lambda$  is chosen to be small such that a perturbative expansion is possible, we expand the part of the exponential containing the interaction term as

$$e^{iS_{\text{int}}} = 1 + (-i)\lambda \int d^4x (\phi_a \phi_a)(\phi_b \phi_b) + \dots. \quad (2.19)$$

Here, each field can be substituted with

$$\phi_a(x) \rightarrow \frac{\delta}{i\delta J_a(x)}, \quad (2.20)$$

as  $\delta/\delta J$  would produce an  $i\phi$  from the  $e^{iJ\phi}$  in  $Z[J]$ . Then, after writing the expansion again as an exponential, it can be moved out of the integral:

$$\begin{aligned} Z[J] &= e^{iS_{\text{int}}[\frac{\delta}{i\delta J}]} \int \mathcal{D}\phi \exp \left\{ -\frac{1}{2} \phi_c D^{-1} \phi_c + iJ_d \phi_d \right\} \\ &= Z_0[0] e^{iS_{\text{int}}[\frac{\delta}{i\delta J}]} \exp \left\{ -\frac{1}{2} J_c (DJ)_c \right\}. \end{aligned} \quad (2.21)$$

### Four-Point Green's Function

As the next step, we calculate the four-point Green's function for the Feynman diagram in Figure 2.1:

$$\begin{aligned} \langle 0 | T\{\phi_{a_1}(x_1)\phi_{a_2}(x_2)\phi_{a_3}(x_3)\phi_{a_4}(x_4)\} | 0 \rangle &= \frac{1}{Z[J]} \left. \frac{\delta^4 Z[J]}{i\delta J_{a_1}(x_1)i\delta J_{a_2}(x_2)i\delta J_{a_3}(x_3)i\delta J_{a_4}(x_4)} \right|_{J=0} \\ \langle 0 | T\{\phi_1\phi_2\phi_3\phi_4\} | 0 \rangle &= \left. \frac{1}{Z[0]} \frac{\delta}{i\delta J_1} \frac{\delta}{i\delta J_2} \frac{\delta}{i\delta J_3} \frac{\delta}{i\delta J_4} Z[J] \right|_{J=0}. \end{aligned}$$

Inserting  $Z[J]$  from Equation (2.21), one finds

$$\frac{Z_0[0]}{Z[0]} \left. \frac{\delta}{\delta J_1} \frac{\delta}{\delta J_2} \frac{\delta}{\delta J_3} \frac{\delta}{\delta J_4} \exp \left( iS_{\text{int}} \left[ \frac{\delta}{i\delta J} \right] \right) \exp \left\{ -\frac{1}{2} J_c (DJ)_c \right\} \right|_{J=0}. \quad (2.22)$$

In what follows, we employ the relations

$$\begin{aligned} \frac{\delta}{\delta J_a(x_i)} (DJ)_b(x) &= \int d^4x \int d^4y \delta^{(4)}(y - x_i) \delta_{ac} D_{bc}(x - y) \\ &= \int d^4x D_{ba}(x - x_i) \\ &\equiv \int d^4x D_{ba}(x - x_i) = \delta_{ab} \int d^4x D_{xx_i}, \end{aligned} \quad (2.23)$$

and

$$\begin{aligned} \frac{\delta}{\delta J_a(x_i)} J_b(x) (DJ)_b(x) &= + \int d^4x \int d^4y \delta^{(4)}(x - x_i) \delta_{ab} D_{bc}(x - y) J_c(y) \\ &\quad + \int d^4x \int d^4y J_b(x) D_{bc}(x - y) \delta_{ac} \delta^{(4)}(y - x_i) \end{aligned} \quad (2.24)$$

$$\begin{aligned} &= + \int d^4y D_{ac}(x_i - y) J_c(y) + \int d^4x J_b(x) D_{ba}(x - x_i) \\ &= 2 \int d^4y D_{ac}(x_i - y) J_c(y) \\ &\equiv 2(DJ)_a(x_i). \end{aligned} \quad (2.25)$$

The factor 2 arises from relabeling the integrals and using the identity  $D(x - y) = D(y - x)$ .<sup>2</sup> Now, if the functional derivatives from the interaction term in Equation (2.22)

$$\exp \left( iS_{\text{int}} \left[ \frac{\delta}{i\delta J} \right] \right) = \left[ 1 + (-i\lambda) \int d^4x \left( \frac{\delta}{\delta J_a(x)} \right)^2 \left( \frac{\delta}{\delta J_b(x)} \right)^2 + \dots \right], \quad (2.26)$$

act on  $\exp \left\{ -\frac{1}{2} J_c D J_c \right\}$ , the first derivative gives us the following contribution

$$\frac{\delta}{\delta J_c(x)} \exp \left\{ -\frac{1}{2} J D J \right\} = -(DJ)_c(x) \exp \left\{ -\frac{1}{2} J D J \right\}.$$

Any subsequent derivatives will give rise to two kinds of contributions: either by acting on a  $(DJ)$  factor or on the exponential,

$$\frac{\delta}{\delta J_c(x)} \left[ (DJ)_d(x) e^{-\frac{1}{2} J D J} \right] = \left[ \frac{\delta}{\delta J_c(x)} (DJ)_d(x) \right] e^{-\frac{1}{2} J D J} + (DJ)_d(x) \frac{\delta}{\delta J_c(x)} e^{-\frac{1}{2} J D J}.$$

1. **Internal double contractions (vacuum/tadpole factors).** If a derivative hits a  $(DJ)$  at the same interaction point  $x$ , we get:

$$\frac{\delta}{\delta J_c(x)} (DJ)_d(x) = \int d^4x D(x - x) \delta_{cd}. \quad (2.27)$$

---

<sup>2</sup>In case of fermions and ghosts, an additional minus sign would enter in Equation (2.24) from the product rule for Grassmann variables. However, the minus sign is then canceled due to  $D(x - y) = -D(y - x)$ .

This result is independent of the external points and factorizes as an overall vacuum factor. Combined with the prefactor  $Z_0[0]$ , it yields  $Z[0] = Z_0[0] (1 + \text{vacuum bubbles})$ , thereby canceling the  $Z[0]$  in the denominator.

2. **Tree contribution.** At first order in Equation (2.26), the four derivatives from  $S_{\text{int}}$  acting on the exponential pull down four linear factors  $(DJ)_i$ , all connected to the same interaction point  $x$ . When the four external derivatives in Equation (2.22) act on these four  $(DJ)$  factors, they produce the propagators  $D(x_1-x) \cdots D(x_4-x)$ , connecting the external points with the vertex. Any term in which an external derivative acts on the exponential instead leaves a bare  $J$ , which vanishes upon setting  $J \rightarrow 0$ .

Following this rule and keeping only the **tree contributions**, we have

$$(-i\lambda) \frac{\delta}{\delta J_1} \frac{\delta}{\delta J_2} \frac{\delta}{\delta J_3} \frac{\delta}{\delta J_4} \left[ \int_x (DJ)_a(y_1) (DJ)_a(y_2) (DJ)_b(y_3) (DJ)_b(y_4) \right] e^{-\frac{1}{2} JDJ} \Big|_{J=0} \quad (2.28)$$

$$= (-i\lambda) \int_x \sum_{\text{all } 4! \text{ assignments}} D_{x_1x} D_{x_2x} D_{x_3x} D_{x_4x} \times (\delta_{aa_i} \delta_{aa_j}) (\delta_{ba_k} \delta_{ba_\ell}). \quad (2.29)$$

Additionally we can further simplify the Kronecker Deltas into  $(\delta_{aa_i} \delta_{aa_j}) (\delta_{ba_k} \delta_{ba_\ell}) = (\delta_{a_ia_j} \delta_{a_ka_\ell})$ . The four external indices can be assigned in  $4!$  ways to the Kronecker Deltas, of which only three are unique, due to commutativity and symmetry of the Kronecker Delta. This leaves us with the overall factor

$$8(\delta_{a_1a_2} \delta_{a_3a_4} + \delta_{a_1a_3} \delta_{a_2a_4} + \delta_{a_1a_4} \delta_{a_2a_3}). \quad (2.30)$$

Putting everything together:

$$\begin{aligned} & \langle 0 | T\{\phi_{a_1}(x_1) \phi_{a_2}(x_2) \phi_{a_3}(x_3) \phi_{a_4}(x_4)\} | 0 \rangle \\ & \stackrel{\text{Tree level}}{=} -i(8\lambda) \underbrace{\left[ \delta_{a_1a_2} \delta_{a_3a_4} + \delta_{a_1a_3} \delta_{a_2a_4} + \delta_{a_1a_4} \delta_{a_2a_3} \right]}_{\text{Feynman Rule}} \int d^4x \underbrace{D_{x_1x} D_{x_2x} D_{x_3x} D_{x_4x}}_{\text{Propagators}}. \end{aligned} \quad (2.31)$$

### Shortcut to the Feynman Rules

While the derivation as done above yields the correct Feynman rules, there is a shortcut to obtain them directly from the Lagrangian. Starting from Equation (2.28), we see that each functional derivative acts on the  $(DJ)_{y_i}$  factors as

$$\begin{aligned} \frac{\delta}{\delta J_{a_i}(x_i)} (DJ)_b(x) &= i \int d^4y D_{ab}(x-y) \frac{\delta J_b(y)}{\delta J_{a_i}(x_i)} \\ &= \int d^4y D_{ab}(x-y) \delta^{(4)}(y-x_i) \delta_{ba_i}. \end{aligned} \quad (2.32)$$

Here, the  $\delta^{(4)}(y - x_i)$  connects the contact vertex to the external points, and  $\delta_{ba_i}$  yields the contribution for the Feynman rules. As the Dirac distributions always link the propagators from the vertex to the external points, the propagators factorise as

$$\prod_{i=1}^4 D(x - x_i). \quad (2.33)$$

Therefore, we solely focus on the Kronecker deltas. In general, these Kronecker deltas encode the structure of the entire field, including Lorentz, gauge, and flavor indices. Therefore, to obtain the Feynman rules, we take a shortcut and consider only contributions from the indices, not the positions.

$$i \frac{\delta^4}{\delta J_{a_1} \delta J_{a_2} \delta J_{a_3} \delta J_{a_4}} [(-\lambda)(J_a)^2(J_b)^2] = (-8i\lambda) (\delta_{a_1 a_2} \delta_{a_3 a_4} + \delta_{a_1 a_3} \delta_{a_2 a_4} + \delta_{a_1 a_4} \delta_{a_2 a_3}). \quad (2.34)$$

This reproduces the combinatorial factors of the quartic interaction. At this point, after doing the replacement  $iJ_i \rightarrow \phi_i$ , we identify the term in the bracket as the interaction term  $\mathcal{L}_{\text{int}}$ :

$$(-\lambda)(J_a)^2(J_b)^2 \longrightarrow (-\lambda)(\phi_a)^2(\phi_b)^2 = \mathcal{L}_{\text{int}}[\phi]. \quad (2.35)$$

Consequently, the Feynman rule of the quartic interaction can be directly obtained by taking the derivatives of the interaction Lagrangian:

$$i \frac{\delta^4 \mathcal{L}_{\text{int}}[\phi]}{\delta \phi_{a_1} \delta \phi_{a_2} \delta \phi_{a_3} \delta \phi_{a_4}} = -i(8\lambda) (\delta_{a_1 a_2} \delta_{a_3 a_4} + \delta_{a_1 a_3} \delta_{a_2 a_4} + \delta_{a_1 a_4} \delta_{a_2 a_3}). \quad (2.36)$$

## 2.4 General Procedure to derive Feynman Rules

Let  $\mathcal{L}_{\text{int}}$  be the interaction part of the Lagrangian:

$$\mathcal{L}_{\text{int}} = \sum_k c_k \mathcal{O}_k[\varphi_i, \dots \partial_\mu \varphi_i, \dots], \quad (2.37)$$

where  $c_k$  is the coupling and  $\mathcal{O}_k$  denotes a product of fields and their derivatives. The fields may be scalars, fermions, vectors, or ghosts.

The derivation of a vertex factor, including the Feynman rule, starts by specifying the Green's function,

$$G^{(n)}(p_1, \dots, p_n) = \langle 0 | T\{\varphi_{i_1}(p_1) \dots \varphi_{i_n}(p_n)\} | 0 \rangle, \quad (2.38)$$

where each  $\varphi_{i_a}(p_a)$  denotes an external field with indices  $i_a$  and momenta  $p_a$ . Here, we

restrict ourselves to the tree-level contribution of the Green's function and neglect higher-order effects.

The shortcut procedure for obtaining the vertex factor is then:

1. **Select relevant terms:** Identify all  $\mathcal{O}_k$  in  $\mathcal{L}_{\text{int}}$  whose field content matches exactly that of the chosen correlator. Terms with additional or missing fields are discarded.
2. **Combinatorial factor:** For each selected term, if it contains  $n_\alpha$  identical copies of a given field species  $\varphi_\alpha$ , calculate

$$\frac{\delta^{n_\alpha} \mathcal{L}_{\text{int}}}{\delta \varphi_{\alpha_1} \delta \varphi_{\alpha_2} \dots \delta \varphi_{\alpha_{n_\alpha}}}. \quad (2.39)$$

For Grassmann-type fields, keep in mind the signs from permutations. (see Appendix A.3 for detailed explanation).

3. **Momentum factors from derivatives:** Each derivative acting on a field  $\partial^\mu \varphi_\alpha$  contributes a factor of  $-ip_\alpha^\mu$ , where  $p_\alpha^\mu$  is the momentum carried by the external leg<sup>3</sup>:

$$\partial^\mu \varphi_\alpha(p) \longrightarrow -i p_\alpha^\mu \varphi_\alpha(p). \quad (2.40)$$

4. **Assemble the vertex:** Assemble the vertex by multiplying the original coupling  $c_k$  by the combinatorial factor, all momentum factors, the Grassmann sign (if applicable), and an overall factor of  $i$ . Any free indices remain explicit in  $V_{i_1 \dots i_n}$  and are contracted with the corresponding external legs.

This shortcut yields the same tree-level factors as the complete path-integral expansion. A detailed explanation and the implementation in MATCHETE are given in Appendix A.

---

<sup>3</sup>This stems from the quantization of fields in position space:  $\varphi = \int \frac{d^3 p}{(2\pi)^3} \frac{1}{\sqrt{2\omega_p}} (a_p e^{-ipx} + a_p^\dagger e^{+ipx})$ . Assuming that all particle momenta are ingoing, we need the  $\propto a_p e^{-ipx}$  contribution. A partial derivative on this part then yields  $\partial_\mu \varphi \rightarrow -ip_\mu^\mu \varphi$ .

## 2.5 The FeynmanRules Algorithm

In this section, we illustrate the use of the `FeynmanRules[Lagrangian, input]` routine, which calculates the Feynman rules at tree level.

For the input, we need a Lagrangian and a Green's Function. Returning to the toy-model EFT from Section 2.2, for the `Lagrangian` we use `LEFT`. The Green's function corresponding to Figure 2.1 is

$$G^{(4)}(p_1, p_2, p_3, p_4) = \langle 0 | T\{\phi_{a1}(x_1)\phi_{a2}(x_2)\phi_{a3}(x_3)\phi_{a4}(x_4)\} | 0 \rangle.$$

In MATCHETE, the Green's function is implemented via

```
In[9]:= input = {ϕ[a1], ϕ[a2], ϕ[a3], ϕ[a4]}
```

The specification of a Green's function is required because the ordering of fields in the correlator determines the overall sign of the Feynman rule from anticommuting fields such as fermions or ghosts. For purely bosonic fields, this ordering is irrelevant. In addition to the overall sign, the field labels/indices defined in the correlator are directly carried over to the external legs in the routine's output. The Feynman rules are then computed using<sup>4</sup>

```
In[10]:= Output = FeynmanRules[LEFT, input]//NiceForm
```

```
Out[10]= 16ig^2 1/M^2 (δ_{a1a4}δ_{a2a3} + δ_{a1a3}δ_{a2a4} + δ_{a1a2}δ_{a3a4}) EXT[φ₁]^{a1} EXT[φ₂]^{a2} EXT[φ₃]^{a3} EXT[φ₄]^{a4}
```

Here,  $\text{EXT}[\varphi_i]^{a_i}$  denotes the external-leg insertion: for scalars it reduces to a factor of 1, for fermions to the corresponding spinor  $u(p)$  or  $v(p)$  (or their adjoints), and for vectors to the polarization vector  $\epsilon_\mu(p)$  or its conjugate. Comparing with the results in Equation (2.36), and keeping  $\lambda \equiv -\frac{2g^2}{M^2}$  in mind, we find that these two expressions coincide.

In case no `input` is provided:

```
In[11]:= FeynmanRules[Lagrangian]
```

computes the Feynman rules for all the terms in the Lagrangian.

---

<sup>4</sup>Again, we restrict ourselves to the renormalizable part.

# Chapter 3

## Scalar Leptoquark $\tilde{S}_1$

### 3.1 Hints towards New Physics

Despite the success of the Standard Model (SM), discrepancies in the flavor sector have emerged in recent years, as highlighted in [16]. The SM predicts that all EW interactions with charged leptons are identical ( up to mass effects) [17]. This would also predict universality in the process

$$b \rightarrow c \ell \nu_\ell,$$

where  $\ell \in \{e, \mu, \tau\}$ . This can be probed by comparing branching ratios of the  $B$ -meson decays

$$R_D = \frac{\mathcal{B}(B \rightarrow D\tau\nu)}{\mathcal{B}(B \rightarrow D\ell\nu)} \quad \text{and} \quad R_{D^*} = \frac{\mathcal{B}(B \rightarrow D^*\tau\nu)}{\mathcal{B}(B \rightarrow D^*\ell\nu)}, \quad \text{where } \ell = e, \mu. \quad (3.1)$$

Measurements, however, display a persistent  $\sim 3.2\sigma$  tension with SM predictions [18, 19] hinting towards a violation of lepton flavour universality (LFU). This tension could be explained by the introduction of leptoquark particles, which couple differently to the respective leptons.[20]. Since such a particle has not been directly observed at the LHC, it is expected to have a mass beyond the energy scale of the SM ( $\Lambda_{EW} \sim 10^2$  GeV).

### 3.2 Theory and Definition

The defining property of a scalar leptoquark (SLQ) is that it couples quarks and leptons, i.e., it permits quark-lepton-LQ interaction vertices. Of the several possibilities for incorporating LQs into the SM, each is characterised by its quantum numbers under  $SU(3)_C \times SU(2)_L \times U(1)_Y$  and their interaction terms [20]. Of the candidates summarised by Dorsner *et al.* in [20], we focus on the  $\tilde{S}_1$  with quantum numbers  $(\bar{\mathbf{3}}, \mathbf{1}, 4/3)$ , which allows us to couple the down-type quarks with leptons:

$$\mathcal{L}_{\text{int}} = + \tilde{y}_{1ij}^{RR} \bar{d}_R^{Ci} \tilde{S}_1 e_R^j + \tilde{z}_{1ij}^{RR} \bar{u}_R^{Ci} \tilde{S}_1^* u_R^j + \text{h.c.} \quad (3.2)$$

From the quantum numbers, we know  $\tilde{S}_1$  is an  $SU(2)_L$  singlet ( $T_3 = 0$ ) with hypercharge  $Y = 4/3$ . Therefore, after EWSB, its electric charge is

$$Q = T_3 + Y = \frac{4}{3}.$$

The Equation (3.2) contains two interaction structures. The first term, proportional to  $\tilde{y}_{1ij}^{RR}$ , couples down-type quarks to leptons. The second term, on the other hand, couples two up-type quarks. However, the  $\tilde{z}_{1ij}^{RR}$  term, which corresponds to a diquark coupling that violates baryon number, would lead to proton decay, as discussed in [21]. Since no such decay has been experimentally observed, we set this coupling to zero and focus solely on the leptoquark interaction  $\tilde{y}_{1ij}^{RR}$ .

For further simplification, we set all entries of  $\tilde{y}_{1ij}^{RR}$  to zero, except for the third-generation diagonal element,  $\tilde{y}_{133}^{RR} \equiv \lambda_t$ .<sup>1</sup> This approach leaves us with a coupling between the  $\tau$ -lepton and the  $b$ -quark:

$$\mathcal{L}_{\text{int},\tilde{S}_1} = \lambda_t \bar{b}_R^C \tilde{S}_1 \tau_R + \text{h.c..} \quad (3.3)$$

Adding the kinetic, mass and interaction term of  $\tilde{S}_1$  to the SM Lagrangian  $\mathcal{L}_{\text{SM}}$  yields the BSM Lagrangian  $\mathcal{L}_{\text{SM+LQ}}$ :

$$\mathcal{L}_{\text{SM+LQ}} = \mathcal{L}_{\text{SM}} + (D_\mu \tilde{S}_1)^\dagger (D_\mu \tilde{S}_1) - M_{\tilde{S}_1}^2 \tilde{S}_1^\dagger \tilde{S}_1 + \lambda_t \bar{b}_{Ra}^C \tilde{S}_1^a \tau_R + \text{h.c..} \quad (3.4)$$

By expanding the covariant derivatives in Equation (3.4), coupling terms of the  $\tilde{S}_1$  to photons and gluons arise. However, as the coupling constant of the strong interaction dominates that of the electromagnetic interaction, we neglect the couplings of the  $\tilde{S}_1$  to the  $\gamma$  and  $Z$ -Bosons. Accordingly, the Lagrangian in Equation (3.4) allows for the interactions depicted in Figure 3.1, together with their Hermitian conjugate:

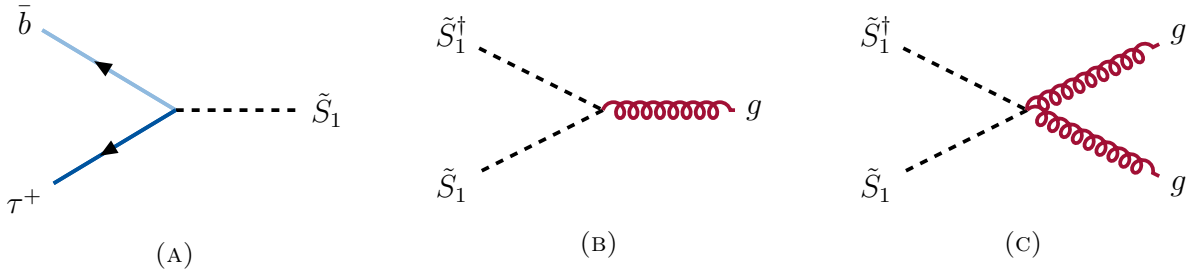


FIGURE 3.1: Feynman rules for interactions involving  $\tilde{S}_1$ . (A) vertex coupling  $\tau$ -lepton and  $b$ -quark. (B) QCD 3-point scalar vertex  $\tilde{S}_1 \tilde{S}_1^\dagger g$ . (C) QCD 4-point scalar vertex  $\tilde{S}_1 \tilde{S}_1^\dagger gg$ .

<sup>1</sup>Note that this LQ will not explain the anomaly from Equation (3.1) because there is no  $b \rightarrow c \ell \nu_\ell$  process mediated by the  $\tilde{S}_1$ . In this thesis, we use the  $\tilde{S}_1$  to study the production of the LQ at the LHC.

**Description:** (A) The Yukawa-like vertex is drawn with two arrows exiting the vertex to reflect that the interaction contains two incoming antifermions, so fermion flow must be tracked carefully. (B) and (C) are the QCD three- and four-point interactions of two scalar leptoquarks with either one or two gluons, respectively.

As of this date, no LQ has been observed. Therefore, the allowed mass range for an SLQ is pushed beyond the SM energy scale, making an EFT analysis with heavy scale  $M_{\tilde{S}_1}$  appropriate. As an illustrative example, in Figure 3.2, we show how the tree-level exchange of  $\tilde{S}_1$  in  $\bar{b}b \rightarrow \tau^+\tau^-$  matches onto a local four-fermion operator at low energies

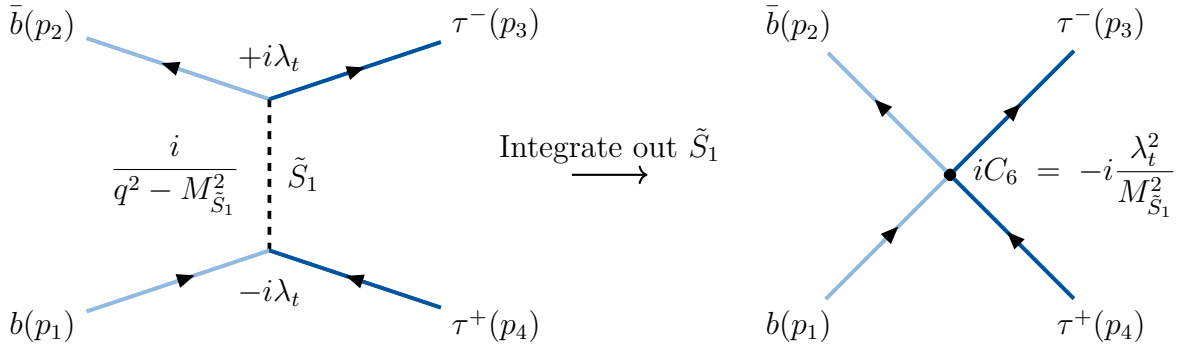


FIGURE 3.2: Tree-level exchange of a scalar leptoquark  $\tilde{S}_1$  in  $b\bar{b} \rightarrow \tau^+\tau^-$  (left) and the corresponding EFT contact interaction obtained after integrating out  $\tilde{S}_1$  (right). For  $|q^2| \ll M_{\tilde{S}_1}^2$ , the induced dimension-six operator is described by the Wilson coefficient  $C_6 = -\lambda_t^2/M_{\tilde{S}_1}^2$ .

In the full theory, the amplitude from  $\tilde{S}_1$  exchange scales with

$$(i\lambda_t) \frac{i}{q^2 - M_{\tilde{S}_1}^2} (-i\lambda_t) \simeq -\frac{i\lambda_t^2}{M_{\tilde{S}_1}^2} \quad \text{for } |q^2| \ll M_{\tilde{S}_1}^2. \quad (3.5)$$

At low energies, where the behaviour of a contact interaction of strength  $\sim \frac{i\lambda_t^2}{M_{\tilde{S}_1}^2}$  is reproduced by the local operator

$$\mathcal{L}_{\text{EFT}} \supset -\frac{\lambda_t^2}{M_{\tilde{S}_1}^2} (\bar{b}_R^C \tau_R) (\bar{\tau}_R b_R^C). \quad (3.6)$$

Equation (3.6) can be further simplified using the Fierz identity into

$$\mathcal{L}_{\text{EFT}} \supset -\frac{\lambda_t^2}{2M_{\tilde{S}_1}^2} (\bar{b} \gamma_\mu P_R b) (\bar{\tau} \gamma^\mu P_R \tau). \quad (3.7)$$

### 3.3 MATCHETE: Model Definition and Matching

In this section, we work through the implementation of the  $\tilde{S}_1$  leptoquark in MATCHETE. The `Match` routine from MATCHETE is designed to match UV theories to the EFTs in the unbroken phase. Consequently, we need to implement the model in the unbroken phase. As evident from Equation (3.4), the leptoquark is an extension of the SM. Therefore, we begin by importing the SM into our notebook.<sup>2</sup>

```
In[2]:=  $\mathcal{L}_{\text{SM}} = \text{LoadModel}["\text{SM}"]$ 
```

This way, we only need to add our BSM physics part to  $\mathcal{L}_{\text{SM}}$ . Next, we define the  $\tilde{S}_1$  with  $\tilde{S}_1 = (\bar{\mathbf{3}}, \mathbf{1}, 4/3)$ , transforming in the antifundamental representation of  $SU(3)_C$  and with hypercharge  $\frac{4}{3}$ . Here, however, we define the particle to have hypercharge  $-\frac{4}{3}$  and to transform in the fundamental representation.<sup>3</sup> Keeping this in mind, we implement it in MATCHETE as

```
In[3]:= DefineField[SS1, Scalar, Indices -> {SU3c[fund]},  
Charges -> {U1Y[-4/3]}, Mass -> {Heavy, MS1}];
```

The mass is set to `MS1`, and the name `SS1` is chosen to represent the particle in the unbroken phase. Later, `S1` will be used to denote the field in the broken phase. Next, we define the coupling  $\lambda_t$  from Equation (3.3). We first define it as an  $n_f \times n_f$  matrix<sup>4</sup>

```
In[4]:= DefineCoupling[λ, SelfConjugate -> True, Indices -> {Flavor, Flavor}];
```

After symmetry breaking, we will set all contributions, except  $\lambda_{33} = \lambda_t$ , to 0. The interaction from Equation (3.3) is implemented as

```
In[5]:=  $\mathcal{L}_{\text{int}} = \text{PlusHc}[\lambda[i, j] \text{ Bar}@CConj@d[a, i] ** e[j] \text{ Bar}@SS1[a]];$ 
```

Again, `i, j` are Flavor indices, and `a` is the  $SU(3)_C$  color index. The `PlusHc` automatically generates the hermitian conjugate. The BSM Lagrangian, as defined in Equation (3.4), is then implemented by

```
In[6]:=  $\mathcal{L}_{\text{BSM}} = \mathcal{L}_{\text{SM}} + \text{FreeLag}[SS1] + \mathcal{L}_{\text{int}};$ 
```

To calculate the EFT to order `n`, we use the following routines

```
In[7]:=  $\mathcal{L}_{\text{EFT}} = \text{GreensSimplify}[\text{Match}[\mathcal{L}_{\text{BSM}}, \text{LoopOrder} -> 0, \text{EFTOrder} -> n],$   
 $\text{ReductionIdentities} -> \text{FourDimensional}];$ 
```

<sup>2</sup>For the implementation of the full SM, cf. [5].

<sup>3</sup>At the time of implementation, MATCHETE did not yet support declaring fields in the anti-fundamental of  $SU(3)_C$ . The workaround of defining it using antiparticle parameters circumvents this limitation.

<sup>4</sup>We set  $n_f = 3$ , as there are three flavors.

The routine `GreensSimplify` reduces the matched EFT using IbP and algebraic identities. The option `ReductionIdentities -> FourDimensional` applies simplification relations valid only in four dimensions, such as Fierz and gamma-matrix reductions. While it has no effect at dimension 6, it further simplifies the operator basis at dimension 8.

For analysis in MG5, the Lagrangian must be expressed in the broken phase after EWSB, as we are interested in the interactions of the physical (mass-eigenstate) fields. EWSB is trivial for the scalar leptoquark  $\tilde{S}_1$ , as it is an  $SU(2)_L$  singlet. The details of preparing the model for MG5 are technical and not instructive; they are therefore delegated to Appendix B.

## 3.4 Feynman Rules for $\tilde{S}_1$

### 3.4.1 Feynman Rules for BSM Theory

In Figure 3.1, we have presented the additional Feynman diagrams that result from the BSM model. Here, we show their Feynman rules obtained by the `FeynmanRules` algorithm.<sup>5</sup>

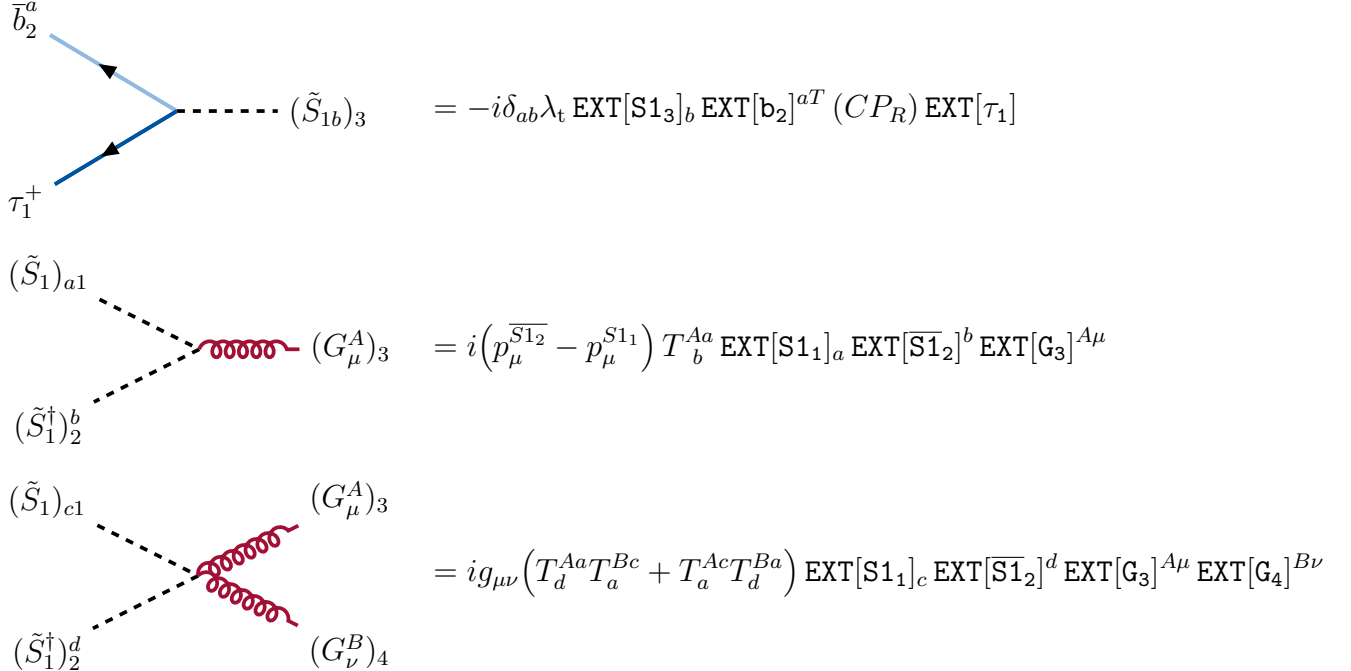


FIGURE 3.3: Left: Feynman diagrams. Right: corresponding Feynman rules. Conventions: all particles incoming;  $a, b, c, d$  are fundamental color indices,  $A, B$  adjoint;  $T^A$  are  $SU(3)_c$  generators.

### 3.4.2 Feynman Rules for EFT Theory at Dimension 6

After matching the EFT up to dimension 6, and using the Fierz identity, the following Feynman rules arise for the four-fermion vertex coinciding with Equation (3.7)

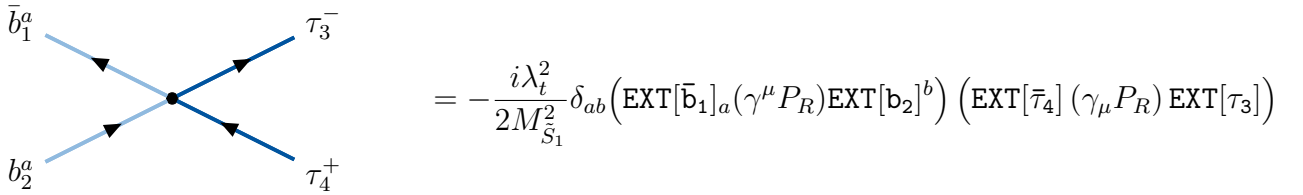
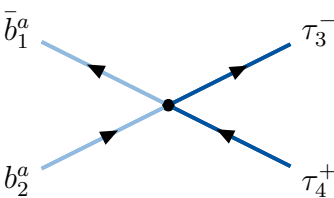


FIGURE 3.4: Effective four-fermion interaction by matching up to dimension 6. Left: EFT diagram. Right: corresponding Feynman rule.

<sup>5</sup>Even though in MATCHETE the  $\tilde{S}_1$  was defined with its antiparticle parameters, here we opt to display it using the original convention for clarity.

### 3.4.3 Feynman Rules for EFT Theory at Dimension 8

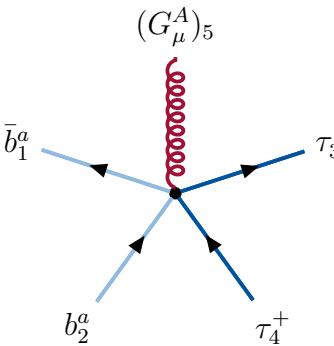
After matching up to dimension 8, we also receive additional contributions beyond the four-fermion vertex. In this thesis, referring to the EFT at dimension 8 means discussing the EFT truncated at dimension 8, which therefore includes operators from dimension 6. Starting with the four-fermion interaction, we have:



$$\begin{aligned} &= -\frac{i\lambda_t^2}{2M_{\tilde{S}_1}^4} \delta_{ab} \left( M_{\tilde{S}_1}^2 - (p_\nu^{b_2} + p_\nu^{\tau_3}) (p_\nu^{\bar{b}_1} + p_\nu^{\bar{\tau}_4}) \right) \\ &\quad \times (\text{EXT}[\bar{b}_1]_a (\gamma^\mu P_R) \text{EXT}[b_2]^b) (\text{EXT}[\bar{\tau}_4] (\gamma_\mu P_R) \text{EXT}[\tau_3]) \end{aligned}$$

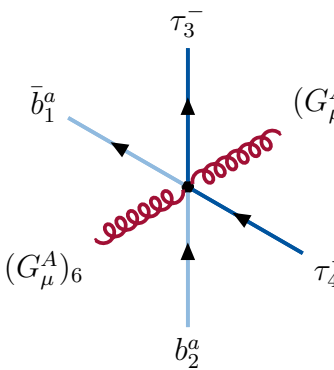
FIGURE 3.5: Effective four-fermion interaction by matching up to dimension 8. Left: EFT diagram. Right: corresponding Feynman rule.

Next, the following two Feynman diagrams are not covered at dimension 6, as their mass dimensions are 8.



$$\begin{aligned} &(G_\mu^A)_5 \\ &= -\frac{i\lambda_t^2}{2M_{\tilde{S}_1}^4} \left( p_\mu^{b_2} + p_\mu^{\tau_3} - p_\mu^{\bar{b}_1} - p_\mu^{\bar{\tau}_4} \right) T_b^{Aa} \text{EXT}[G_5]^{A\mu} \\ &\quad \times (\text{EXT}[\bar{b}_1]_a (\gamma^\mu P_R) \text{EXT}[b_2]^b) (\text{EXT}[\bar{\tau}_4] (\gamma_\mu P_R) \text{EXT}[\tau_3]) \end{aligned}$$

FIGURE 3.6: Effective four-fermion and one gluon interaction by matching up to dimension 8. Left: EFT diagram. Right: corresponding Feynman rule.



$$\begin{aligned} &(G_\mu^A)_5 \\ &= -\frac{i\lambda_t^2}{2M_{\tilde{S}_1}^4} \eta_{\mu\nu} (T_a^{Aa} T_b^{Ba} + T_a^{Ba} T_b^{Aa}) \text{EXT}[G_5]^{A\mu} \text{EXT}[G_6]^{B\nu} \\ &\quad \times (\text{EXT}[\bar{b}_1]_a (\gamma^\mu P_R) \text{EXT}[b_2]^b) (\text{EXT}[\bar{\tau}_4] (\gamma_\mu P_R) \text{EXT}[\tau_3]) \end{aligned}$$

FIGURE 3.7: Effective four-fermion and two gluons interaction by matching up to dimension 8. Left: EFT diagram. Right: corresponding Feynman rule.



## Chapter 4

# Scalar Leptoquark $\tilde{S}_1$ : EFT and BSM convergence

In this chapter, we investigate how the EFTs of the  $\tilde{S}_1$  converge towards the BSM theory. As mentioned in Section 1.2, in the limit  $E \ll \Lambda$ , the EFT is expected to reproduce the same predictions of the underlying theory. For our case, the relevant scale  $\Lambda$  is set by the leptoquark mass  $M_{\tilde{S}_1}$ , such that increasing  $M_{\tilde{S}_1}$  corresponds to extending the range of validity of the EFT approximation. To test this, we vary  $M_{\tilde{S}_1}$  and compare cross sections for different hadronic processes. Additionally, we will investigate how changing the coupling constant  $\lambda_t$  affects convergence.

For this purpose, we use MG5 [1], which enables automated generation and simulation of cross sections. The structure of this chapter is as follows. We first discuss the settings used in MG5. We then proceed to the analysis of the convergence of the EFT series. Here, we will perform an in-depth analysis of the two hadronic processes  $pp \rightarrow \tau\tau (+b)$  and examine their dependence on the mass  $M_{\tilde{S}_1}$  and the coupling  $\lambda_t$ .

## 4.1 MG5 Settings

Before turning to hadronic processes, we need to specify the parameters of our MG5 simulation. The simplest channel in which a  $\tilde{S}_1$  is produced at LHC is the  $b\bar{b} \rightarrow \tau^+\tau^-$  channel. At leading order, the process arises from a single diagram (see Figure 4.3), making it particularly well-suited for testing the setup.

In a typical MG5 simulation, two types of input cards are required, namely the `run_card` and the `param_card` [1]. The `run_card` collects all settings related to the numerical setup of the event generation, including the choice of parton distribution functions (PDFs), the number of generated events, and parameters for the Monte Carlo integration (such as cuts, scales, and phase-space sampling strategies). The `param_card`, on the other hand, specifies the physical model parameters: particle masses, decay widths, and couplings, and thereby the BSM and EFT parameters.

To obtain consistent results, we first fine-tune the `run_card`. Following [22], we use the NNPDF3.0NNLO PDF set [23], which in MG5 is accessed via `lhaid = 261000` [1, 24]. We work in the five-flavor scheme, where  $b$  quarks are treated as partons inside the proton. In the `param_card`, we vary the coupling  $\lambda_t \in \{1.0, 1.7, 2.5\}$ . Additionally, we fix the random seed for numerical integration to 30 to ensure reproducibility.<sup>1</sup> Unless otherwise specified, 10.000 events are generated by default. We also investigate how different values of `dynamical_scale_choice` (DSC) affect the simulations. In MG5, DSC sets the renormalization and factorization scales used for the simulation. They are set dynamically from the event kinematics, and the possible options are given below.<sup>2</sup>

Value	<code>dynamical_scale_choice</code> (DSC) meaning	
1	total transverse energy of the event	$\sum_{i=1}^N \frac{E_i \cdot p_{T,i}}{\sqrt{p_{x,i}^2 + p_{y,i}^2 + p_{z,i}^2}}.$
2	sum of the transverse mass	$\sum_{i=1}^N \sqrt{m_i^2 + p_{T,i}^2}.$
3	sum of the transverse mass divide by 2	$\frac{1}{2} \sum_{i=1}^N \sqrt{m_i^2 + p_{T,i}^2}.$
4	partonic center of mass energy	$\sqrt{\hat{s}}.$

TABLE 4.1: Values supported for `dynamical_scale_choice`. Table from [2].

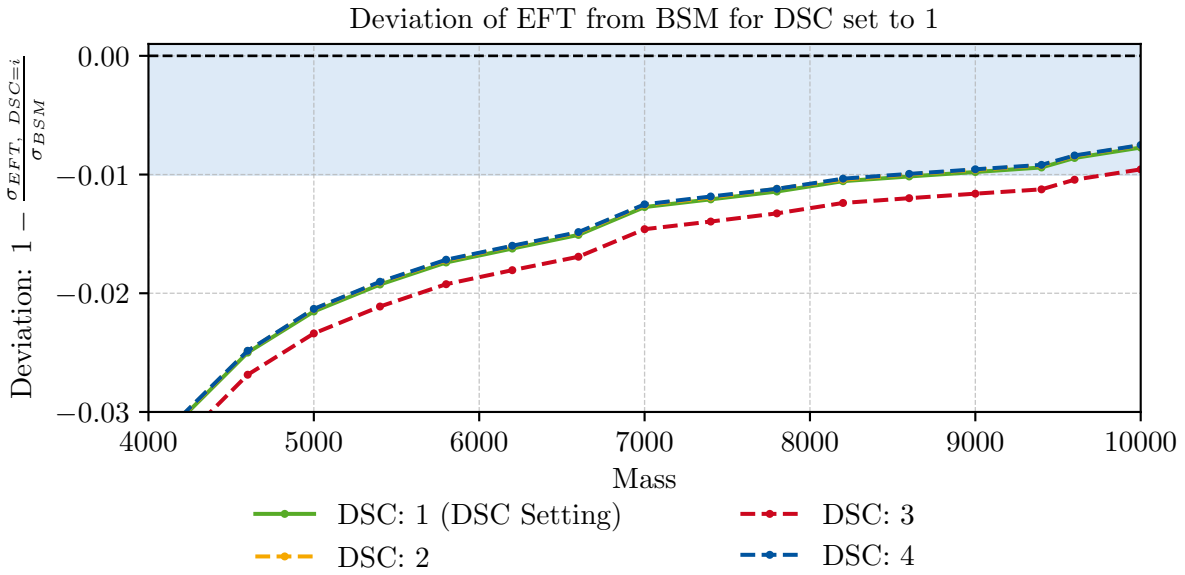
While all choices are theoretically valid, they lead to slightly different cross sections for both the EFT and the BSM theory. In MG5, the output also provides cross sections corresponding to alternative scale choices obtained through a reweighting procedure. Since this does not

<sup>1</sup>In Appendix D, we have investigate the numerical stability for different seeds.

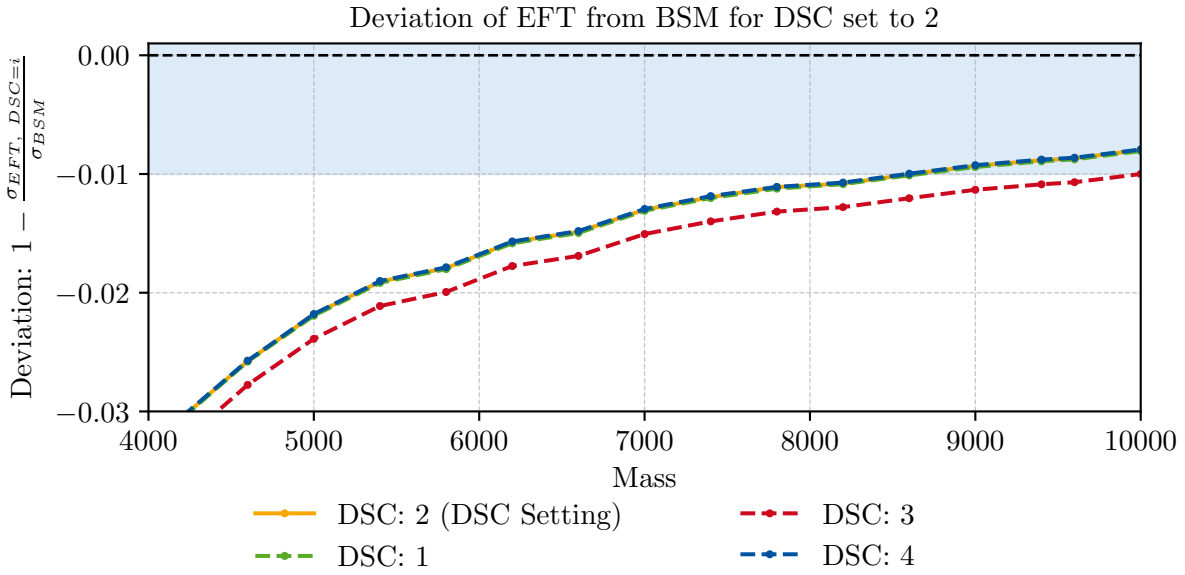
<sup>2</sup>The default `dynamical_scale_choice = -1` sets the central scale from the transverse mass of the final-state partons obtained via  $k_T$  clustering [2, 25]. As noted in [25], this choice is diagram-dependent, which will bias EFT BSM comparisons. It also produced the largest discrepancies in our convergence tests. We therefore exclude it from our analysis.

fully capture the scale dependence, the reweighted values may differ slightly from those obtained through explicit calculations.

To quantify the effect of choosing different DSC, we compute the cross section of  $b\bar{b} \rightarrow \tau^+\tau^-$  for each DSC, comparing explicit and reweighted results in both the EFT at dimension 6 and BSM cases. The relative deviation of EFT from BSM predictions is shown in Figure 4.1. Solid lines represent explicit results; dashed lines, reweighted results. We chose not to include the uncertainty band of the DSC choices for clarity.<sup>3</sup>



(A) Results for `dynamical_scale_choice = 1`. (DSC 2 coincides almost perfectly with DSC 4)



(B) Results for `dynamical_scale_choice = 2`.

<sup>3</sup>We have checked that the scale uncertainties provided by MG5 are larger than the deviations between the individual DSC settings.

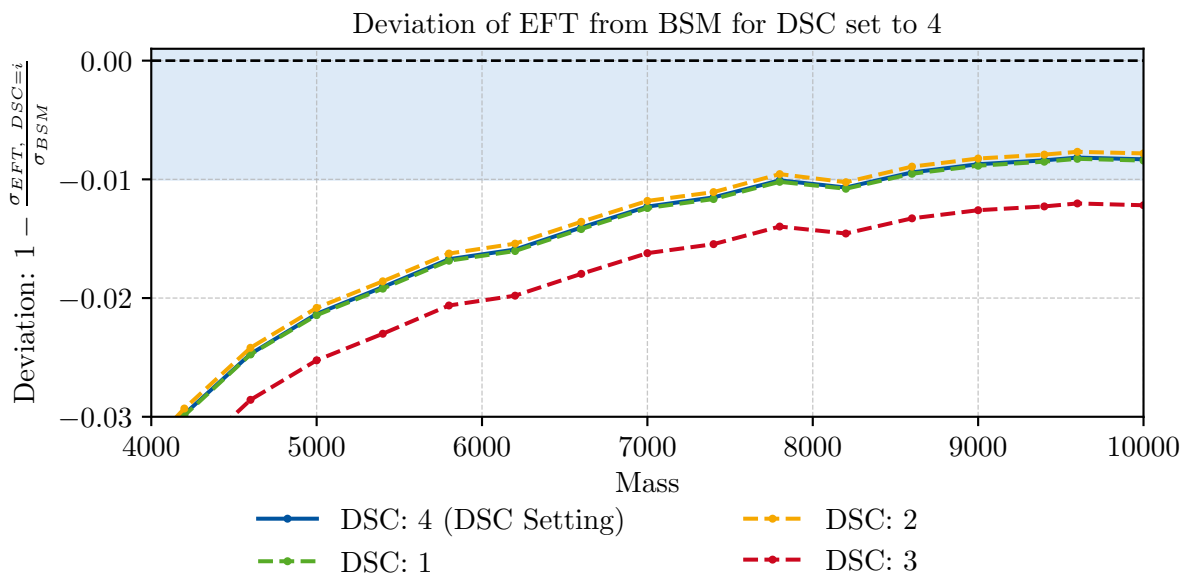
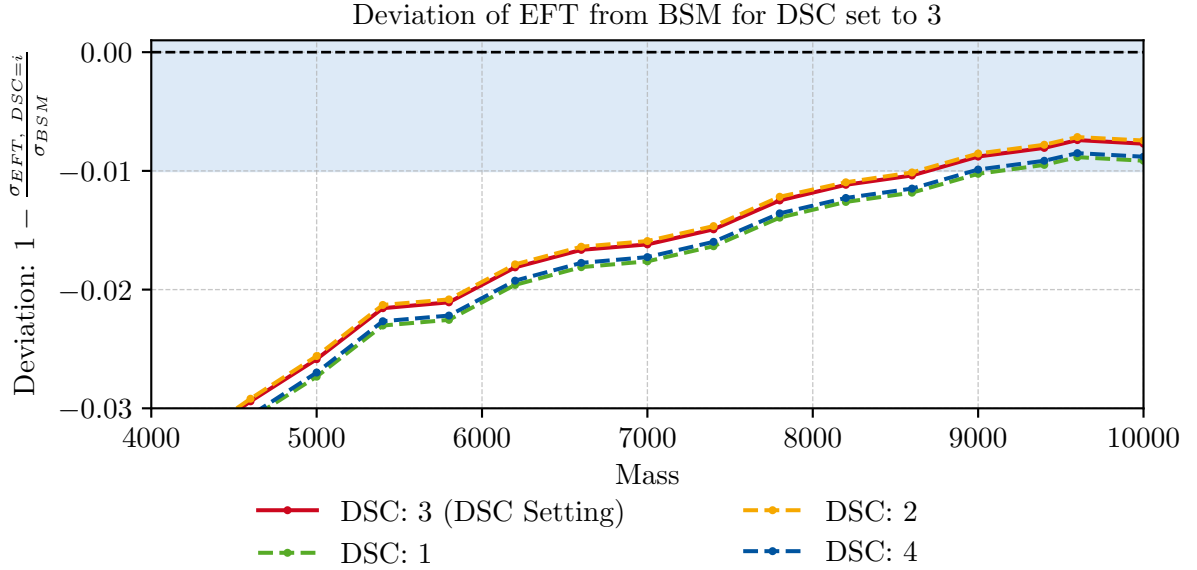


FIGURE 4.1: Deviation of the EFT (order 6) prediction from the full BSM theory for  $b\bar{b} \rightarrow \tau^+\tau^-$  for different `dynamical_scale_choices`. Solid lines represent the explicit setting chosen for cross-section simulation, dashed lines denote reweighted results. The shaded blue region marks deviations below 1%.

The results in Figure 4.1 are overall very similar, with only minor variations. The case `dynamical_scale_choice = 3` shows a slightly larger deviation. In the following, we adopt `dynamical_scale_choice = 4`, motivated by its physical interpretation as the partonic center-of-mass energy  $\sqrt{\hat{s}}$ .

The final parameter choices are summarized in Table 4.2 and Table 4.3. Unless explicitly stated otherwise, these settings are used throughout the remainder of this thesis.

Description	run_card	Value
Setting own PDF set	pdlable	lhapdf
PDF set NNPDF3.0NNLO	lhaid	261000
Phase Space Integration Strategy	sde_strategy	1
Dynamical Scale Choice (COE of parton $\sqrt{\hat{s}}$ )	dynamical_scale_choice	4
Random Seed	iseed	30

TABLE 4.2: Parameters set in the `run_card`. All other values are left with MG5 default.

Description	param_card	Value
Mass of $\tilde{S}_1$	MS1	$M_{\tilde{S}_1}$
BSM coupling $\lambda_t$	Lambdat	$\lambda_t \in \{1.0, 1.7, 2.5\}$
Mass of Leptons $e, \mu, \tau$	Me, MMu, MTau	0
Mass of light quarks $u, d, s, c, b$	Mu, Md, Ms, Mc, Mb	0
Top Mass $M_t$	Mt	172.00

TABLE 4.3: Parameters set in the `param_card`. All other values are left with MG5 default.

## 4.2 Overview of Hadronic Interactions and Validation with ATLAS

For the hadronic processes, we consider processes involving two protons  $p$  in the initial state and two  $\tau$ -leptons, as well as zero, one, or two  $b$ -quarks in the final state. To put it more specifically,

$$1. pp \rightarrow \tau^+ \tau^- \quad 2. pp \rightarrow \tau^+ \tau^- b \quad 3. pp \rightarrow \tau^+ \tau^- \bar{b} \quad 4. pp \rightarrow \tau^+ \tau^- \bar{b} b$$

Throughout, we adopt the five-flavor scheme (5FS), where the bottom quark is treated as a massless parton inside the proton<sup>4</sup>. In this scheme,  $b$  and  $\bar{b}$  parton densities arise from the sea-quarks, while the (massive) top quark is absent from the initial state.

Because our Lagrangian preserves  $CP$ , processes 2 and 3 are  $CP$ -conjugate and therefore have identical partonic cross sections. In  $pp$  collisions, differences might arise from  $b\bar{b}$  PDF asymmetries, which we neglect here. We therefore restrict ourselves to the explicit simulation of process 2. [7, 26]

### Comparison with ATLAS

ATLAS has published cross-section results for leptoquark production, including the scalar LQ  $\tilde{S}_1$  [22]. Their study is not conducted using EFTs, but serves as a good comparison for our simulations. To maintain consistency, we utilize the same PDF set as in [22]. Since this paper does not specify the DSC, we set DSC = 4 and use MG5’s DSC scale-variation estimation as the uncertainty.

Figure 4.2 shows ATLAS and our results from the MATCHETE implementation for processes 2, 3, and 4. Including the DSC uncertainty, the results agree for  $\lambda_t = 1.7$  and 2.5. The main difference appears at low  $M_{\tilde{S}_1}$  for  $\lambda_t = 1.0$  and converges as the mass increases. This can be (partially) explained by numerical instabilities. The final state with two  $b$ -quarks suffers from numerical issues due to small cross sections. Moreover, for  $M_{\tilde{S}_1} \gtrsim 3$  TeV, MG5 yields numerical underflow errors, suggesting limited accuracy even at lower masses. Consequently, we will not further analyze the process containing two  $b$ -quarks in the final state in this thesis.

As [22] does not specify the exact process simulated, nor the `run_card` and `param_card` options, we cannot match the precise simulation conditions. As a cross-check, we reran the simulations with the UFO model file from Dorsner *et al.* [6]. The results matched ours perfectly, ruling out implementation errors.

---

<sup>4</sup>For a proper five-flavor scheme, we need to implement this already in the UFO-file, such that MG5 can make use of the symmetries in calculating processes. Additionally, we can include the  $b, \bar{b}$  as a parton into the proton via `define p = p b b~`.

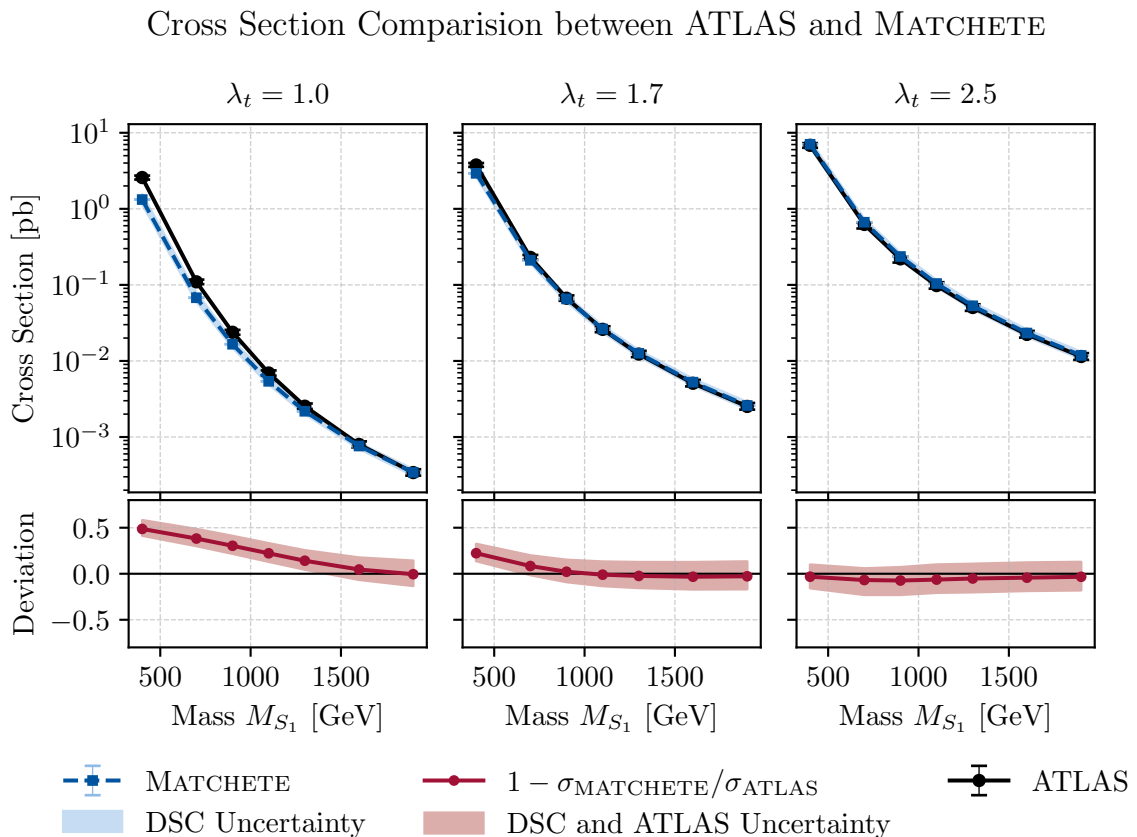


FIGURE 4.2: Comparison of cross section  $\sigma$  from ATLAS (black) with MATCHETE (blue) implementation, including the DSC Uncertainty given by MG5, for  $\lambda_t = 1.0, 1.7$  and  $2.5$ . In the lower plot, the deviation  $1 - \sigma_{\text{MATCHETE}}/\sigma_{\text{ATLAS}}$  including the propagated uncertainty is presented. Results are shown for leptoquark masses between 400 GeV and 1900 GeV.

### 4.3 Hadronic Interaction without a final state $b$ -quark:

$$pp \rightarrow \tau^+ \tau^-$$

In the previous section, we have already stated that the interaction  $b\bar{b} \rightarrow \tau^+\tau^-$  has exactly one Feynman diagram:

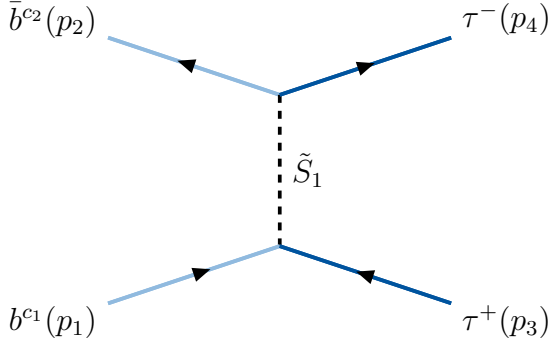


FIGURE 4.3: Tree-level  $\tilde{S}_1$  exchange in  $b\bar{b} \rightarrow \tau^+\tau^-$ . Here,  $p_i$  denotes momenta and  $c_i$  the color indices of the initial quarks.

In the diagram above, we see that the fermion-flow (arrow) is not continuous at each vertex due to charge-conjugated spinors.<sup>5</sup> Nevertheless, the external states contain a fermion and an antifermion both in the initial and final states, so the total fermion number is conserved. We now compute the averaged squared amplitude  $\overline{|\mathcal{M}|^2}$  in the BSM theory and in the EFTs truncated at dimensions 6 and 8, and show how the conservation is made explicit.

#### Theoretical Result

Using MATCHETE, we derived the Feynman rules for the BSM theory in Section 3.4.1. For the diagram shown above, the corresponding amplitude reads

$$i\mathcal{M}_{\text{BSM}} = -i\lambda_t^2 \left[ \bar{u}_\tau(p_4) P_R (C \bar{v}_b(p_2)^T) \right] \frac{\delta_{c_2 c_1}}{t - M_{\tilde{S}_1}^2} \left[ (u_b(p_1)^T C^\dagger) P_R v_\tau(p_3) \right]. \quad (4.1)$$

Here,  $C$  denotes the charge-conjugation matrix with  $C^\dagger = C^{-1}$ , and  $P_{R/L} = \frac{1 \pm \gamma_5}{2}$  are the chiral projection operators.<sup>6</sup>  $\delta_{c_2 c_1}$  is the Kronecker delta contracting the initial-state color indices  $c_1$  and  $c_2$ . The Mandelstam variable

$$t = (p_1 - p_3)^2 = (p_2 - p_4)^2,$$

<sup>5</sup>To make the fermion flow explicit, we slightly changed the convention of Feynman diagrams. In the diagrams, we distinguish between fermions and antifermions.

<sup>6</sup>The subtleties that arise when dealing with fermion-number-violating diagrams are discussed in [27].

corresponds to the momentum exchanged by the scalar leptoquark  $\tilde{S}_1$ . In Equation (4.1), we see that each bracket violates fermion number. However, this expression can be simplified using the Fierz identities:

$$i\mathcal{M}_{\text{BSM}} = -i \frac{\lambda_t^2}{2} \frac{\delta_{c_2 c_1}}{t - M_{\tilde{S}_1}^2} [\bar{u}_\tau(p_4) \gamma_\mu P_R v_\tau(p_3)] [(u_b(p_1)^T C^{-1}) \gamma^\mu P_R (C \bar{v}_b(p_2)^T)]. \quad (4.2)$$

Using the relations

$$C^{-1}(\gamma_\mu P_{R/L})C = -(\gamma_\mu P_{L/R})^T, \quad P_{R/L}^T = P_{R/L}, \quad P_{R/L}\gamma_\mu = \gamma_\mu P_{L/R}, \quad (4.3)$$

the amplitude further simplifies to

$$\begin{aligned} i\mathcal{M}_{\text{BSM}} &= +i \frac{\lambda_t^2}{2} \frac{\delta_{c_2 c_1}}{t - M_{\tilde{S}_1}^2} [\bar{u}_\tau(p_4) \gamma_\mu P_R v_\tau(p_3)] [u_b(p_1)^T (\gamma^\mu P_L)^T \bar{v}_b(p_2)^T] \\ &= -i \frac{\lambda_t^2}{2} \frac{\delta_{c_2 c_1}}{t - M_{\tilde{S}_1}^2} [\bar{u}_\tau(p_4) \gamma_\mu P_R v_\tau(p_3)] [\bar{v}_b(p_2) \gamma^\mu P_R u_b(p_1)]. \end{aligned} \quad (4.4)$$

Now, the apparent fermion-flow violation at each vertex is no longer visible. The resulting expression explicitly shows that the overall process conserves fermion number. The Hermitian is given by

$$\mathcal{M}_{\text{BSM}}^\dagger = -\frac{\lambda_t^2}{2} \frac{\delta_{c_2 c_1}}{t - M_{\tilde{S}_1}^2} [u_b^\dagger(p_1) P_R^\dagger \gamma^{\mu\dagger} \bar{v}_b^\dagger(p_2)] [v_\tau^\dagger(p_3) P_R^\dagger \gamma_\mu^\dagger \bar{u}_\tau^\dagger(p_4)]. \quad (4.5)$$

Using  $\gamma_0^2 = 1$ ,  $\bar{\psi}^\dagger = \gamma_0 \psi$ , and  $\gamma_0 \gamma^{\mu\dagger} \gamma_0 = \gamma^\mu$ , we obtain

$$\mathcal{M}_{\text{BSM}}^\dagger = -\frac{\lambda_t^2}{2} \frac{\delta_{c_2 c_1}}{t - M_{\tilde{S}_1}^2} [\bar{u}_b(p_1) P_L \gamma^\mu v_b(p_2)] [\bar{v}_\tau(p_3) P_L \gamma_\mu u_\tau(p_4)]. \quad (4.6)$$

Squaring the amplitude and summing over spins and colors gives

$$\sum_{\text{spins, colors}} |\mathcal{M}_{\text{BSM}}|^2 = 9 \frac{\lambda_t^4}{4(t - M_{\tilde{S}_1}^2)^2} \sum_{\text{spins}} [\bar{u}_{b_1} P_L \gamma^\nu v_{b_2}] [\bar{v}_{\tau_3} P_L \gamma_\nu u_{\tau_4}] [\bar{u}_{\tau_4} \gamma_\mu P_R v_{\tau_3}] [\bar{v}_{b_2} \gamma^\mu P_R u_{b_1}],$$

where the factor of 9 arises from the color factors. Using the completeness relations  $\sum u \bar{u} = \not{p}$  and  $\sum v \bar{v} = \not{p}$  for massless fermions, we obtain

$$\begin{aligned} \sum_{\text{spins, colors}} |\mathcal{M}_{\text{BSM}}|^2 &= 9 \frac{\lambda_t^4}{4(t - M_{\tilde{S}_1}^2)^2} \text{Tr}[\not{p}_4 \gamma_\mu P_R \not{p}_3 P_L \gamma_\nu] \text{Tr}[\not{p}_2 \gamma^\mu P_R \not{p}_1 P_L \gamma^\nu] \\ &= 9 \frac{\lambda_t^4}{4(t - M_{\tilde{S}_1}^2)^2} \text{Tr}[\not{p}_4 \gamma_\mu \not{p}_3 \gamma_\nu P_R] \text{Tr}[\not{p}_2 \gamma^\mu \not{p}_1 \gamma^\nu P_R]. \end{aligned} \quad (4.7)$$

Evaluating the traces and contracting indices yields  $16(p_1 \cdot p_3)(p_2 \cdot p_4)$ , and therefore

$$\sum_{\text{spins, colors}} |\mathcal{M}_{\text{BSM}}|^2 = 9 \frac{4\lambda_t^4}{(t - M_{\tilde{S}_1}^2)^2} (p_1 \cdot p_3)(p_2 \cdot p_4). \quad (4.8)$$

After averaging over initial spins ( $1/4$ ) and colors ( $1/9$ ), and since  $2p_1 \cdot p_3 = 2p_2 \cdot p_4 = -t$ , we obtain:

**Averaged Squared Amplitude  
(BSM theory):**

$$\overline{|\mathcal{M}_{\text{BSM}}|^2} = \frac{\lambda_t^4}{4} \frac{t^2}{(t - M_{\tilde{S}_1}^2)^2}.$$

(4.9)

We now turn to the EFT cases. For the EFT truncated at dimension 6, the Feynman diagram with its corresponding Feynman rule, after using Fierz identity, is shown in Figure 3.4. Here, with the initial and final states as defined in Figure 4.3, we get

$$i\mathcal{M}_{\text{EFT}, D=6} = -\frac{i\lambda_t^2}{2M_{\tilde{S}_1}^2} \delta_{c_2 c_1} [\bar{u}_\tau(p_4) \gamma_\mu P_R v_\tau(p_3)] [\bar{v}_b(p_2) \gamma^\mu P_R u_b(p_1)]. \quad (4.10)$$

Again, this matrix element conserves fermion number. Comparing this with Equation (4.4), we observe that the expression is identical, only the propagator is replaced by a constant coupling. The squared and spin-color-summed amplitude, therefore, becomes

$$\sum_{\text{spins, colors}} |\mathcal{M}_{\text{EFT}, D=6}|^2 = 9 \frac{4\lambda_t^4}{M_{\tilde{S}_1}^4} (p_1 \cdot p_3)(p_2 \cdot p_4), \quad (4.11)$$

and after averaging over initial states:

**Averaged Squared Amplitude  
(EFT truncated at  $D = 6$ ):**

$$\overline{|\mathcal{M}_{\text{EFT}, D=6}|^2} = \frac{\lambda_t^4}{4} \frac{t^2}{M_{\tilde{S}_1}^4}.$$

(4.12)

For the EFT truncated at dimension 8, the Feynman rule from Figure 3.5, for our initial and final states, gives

$$\begin{aligned} i\mathcal{M}_{\text{EFT}, D \leq 8} &= -\frac{i\lambda_t^2}{2M_{\tilde{S}_1}^4} \delta_{c_2 c_1} (M_{\tilde{S}_1}^2 - (p_1 - p_3) \cdot (p_2 - p_4)) [\bar{u}_\tau(p_4) \gamma_\mu P_R v_\tau(p_3)] [\bar{v}_b(p_2) \gamma^\mu P_R u_b(p_1)] \\ &= -\frac{i\lambda_t^2}{2M_{\tilde{S}_1}^4} \delta_{c_2 c_1} (M_{\tilde{S}_1}^2 + t) [\bar{u}_\tau(p_4) \gamma_\mu P_R v_\tau(p_3)] [\bar{v}_b(p_2) \gamma^\mu P_R u_b(p_1)]. \end{aligned} \quad (4.13)$$

The Lorentz and color structures match those of the BSM case. Hence, we can directly infer

$$\sum_{\text{spins, colors}} |\mathcal{M}_{\text{EFT}, D \leq 8}|^2 = 9 \frac{4\lambda_t^4}{M_{\tilde{S}_1}^8} (M_{\tilde{S}_1}^2 + t)^2 (p_1 \cdot p_3)(p_2 \cdot p_4). \quad (4.14)$$

Averaging over initial spins and colors yields:

**Averaged Squared Amplitude  
(EFT truncated at  $D = 8$ ):**

$$\boxed{\overline{|\mathcal{M}_{\text{EFT}, D \leq 8}|^2} = \frac{\lambda_t^4}{4} \frac{(M_{\tilde{S}_1}^2 + t)^2}{M_{\tilde{S}_1}^8} t^2}. \quad (4.15)$$

Expanding the bracket explicitly shows that this result decomposes into the individual contributions from dimension 6 and 8 operators and their interference:

$$\begin{aligned} \overline{|\mathcal{M}_{\text{EFT}, D \leq 8}|^2} &= \frac{\lambda_t^4}{4} \frac{t^2}{M_{\tilde{S}_1}^4} + 2 \frac{\lambda_t^4}{4} \frac{t^3}{M_{\tilde{S}_1}^6} + \frac{\lambda_t^4}{4} \frac{t^4}{M_{\tilde{S}_1}^8} \\ &= \overline{|\mathcal{M}_{\text{EFT}, D=6}|^2} + \overline{2 \text{Re}(\mathcal{M}_{\text{EFT}, D=6} \mathcal{M}_{\text{EFT}, D=8}^\dagger)} + \overline{|\mathcal{M}_{\text{EFT}, D=8}|^2}. \end{aligned}$$

The first term corresponds to Equation (4.12), the averaged squared amplitude for the EFT at dimension 6. The second term is the interference between dimensions 6 and 8, while the third and last term is the pure dimension 8 contribution. The identification of these terms follows directly from the power of  $M_{\tilde{S}_1}$ .

To demonstrate the EFT-BSM correspondence explicitly, consider the expansion of the propagator in Equation (4.9) for  $t \ll M_{\tilde{S}_1}^2$ :

$$\frac{1}{t - M_{\tilde{S}_1}^2} = -\frac{1}{M_{\tilde{S}_1}^2} - \frac{t}{M_{\tilde{S}_1}^4} + \mathcal{O}\left(\frac{t^2}{M_{\tilde{S}_1}^6}\right), \quad (4.16)$$

and hence

$$\frac{1}{(t - M_{\tilde{S}_1}^2)^2} \approx \frac{1}{M_{\tilde{S}_1}^4} + \frac{2t}{M_{\tilde{S}_1}^6} + \frac{t^2}{M_{\tilde{S}_1}^8}. \quad (4.17)$$

Higher terms in the propagator expansion would generate contributions of order  $1/M_{\tilde{S}_1}^8$ . However, our EFT is truncated at dimension 8; we therefore expand the propagator only up

to  $\mathcal{O}(1/M_{\tilde{S}_1}^4)$ . Substituting this expansion into Equation (4.9) gives:

$$\begin{aligned}\overline{|\mathcal{M}_{\text{BSM}}|^2} &\approx \frac{\lambda_t^4}{4} \frac{t^2}{M_{\tilde{S}_1}^4} + 2 \frac{\lambda_t^4}{4} \frac{t^3}{M_{\tilde{S}_1}^6} + \frac{\lambda_t^4}{4} \frac{t^4}{M_{\tilde{S}_1}^8} \\ &\approx |\mathcal{M}_{\text{EFT}, D=6}|^2 + \overline{2 \operatorname{Re}(\mathcal{M}_{\text{EFT}, D=6} \mathcal{M}_{\text{EFT}, D=8}^\dagger)} + |\mathcal{M}_{\text{EFT}, D=8}|^2 \\ &\approx |\mathcal{M}_{\text{EFT}, D \leq 8}|^2.\end{aligned}$$

Perfectly reproducing the EFT expressions order by order.

In the phenomenological analysis, we will quantify the regime in which the EFT reproduces the full BSM theory by studying the relative deviation of the EFT cross sections from the exact result:

$$\text{Relative Deviation} \equiv \frac{\sigma_{\text{BSM}} - \sigma_i}{\sigma_{\text{BSM}}}, \quad \text{with } i \in \{\text{EFT, } D=6; \text{ EFT, } D \leq 8\}. \quad (4.18)$$

In general, cross sections scale  $\propto \overline{|\mathcal{M}|^2}$ . And as we have seen that the squared amplitudes all scale as  $\propto \lambda_t^4$ , the couplings cancel in the ratio. This implies that the relative deviation between the EFT and BSM cross section, for  $pp \rightarrow \tau^+ \tau^-$ , is independent of  $\lambda_t$ .

In Section 4.4, we will investigate whether this also holds for processes involving  $b$  quarks in the final states.

### Simulation Results of $pp \rightarrow \tau^+\tau^-$

We begin with the total cross sections for the BSM and EFTs as a function of the LQ mass in Figure 4.4, along with their statistical uncertainties. The plots in this section are for  $\lambda_t = 1.0$ . The corresponding plots for  $\lambda_t = 1.7, 2.5$  are given in the Appendix C.1. Here, we can see that the EFTs follow the general shape of the BSM model. Already in this plot, we can identify a mismatch between EFT and BSM at low LQ masses. To investigate this further, we move to the deviation plot in Figure 4.5. To this end, we show the relative deviation as defined in Equation (4.18) with the propagated statistical uncertainty together with a  $\pm 1\%$  band around the BSM prediction as a function of the LQ mass.

As  $M_{\tilde{S}_1}$  increases, the agreement between the EFT and the full model improves, as the expansion parameter  $E^2/M_{\tilde{S}_1}^2$  becomes small. Thus, truncations at  $D = 6$  or  $D \leq 8$  remain reliable when  $E \ll M_{\tilde{S}_1}$ . At lower masses, however, this condition fails, and the EFT deviates noticeably, for instance, at  $M_{\tilde{S}_1} = 1$  TeV we observe a deviation of about 30%.

Nevertheless, the convergence rate differs between the two EFT orders. Since the truncation at  $D \leq 8$  includes higher order terms in the  $1/M_{\tilde{S}_1}^2$  expansion, the cross section approaches the BSM prediction more quickly than at  $D = 6$ . Already for  $M_{\tilde{S}_1} \gtrsim 1400$  GeV, the  $D \leq 8$  result remains within the  $\pm 1\%$  accuracy band and the BSM prediction is within the error-bar of the EFT. For the same masses, the dimension 6 EFT, on the other hand, still deviates by about  $-17.5\%$ . Only above  $M_{\tilde{S}_1} \gtrsim 3200$  GeV does the  $D = 6$  result fall below a  $-5\%$  deviation. To examine whether the dimension 6 EFT eventually reaches the  $\pm 1\%$  level, an enlarged view of the deviation in the mass range 5000-10000 GeV is presented in Figure 4.6. Again, we see that the EFT truncated at  $D = 8$  closely matches the full BSM result. The dimension 6 approximation shows a slower convergence: above  $M_{\tilde{S}_1} \gtrsim 5200$  GeV the deviation falls below 2%, while the  $\pm 1\%$  level is only reached for  $M_{\tilde{S}_1} \gtrsim 8400$  GeV. Due to numerical fluctuations, the exact mass value at which this threshold is crossed cannot be determined with high precision.

Deviations from the BSM theory can, in principle, arise from two distinct sources. On the one hand, there is the intrinsic theoretical uncertainty associated with truncating the EFT expansion. On the other hand, numerical uncertainties in the Monte Carlo simulation, such as those induced by the choice of random seed or by limited event statistics, can generate fluctuations at the percent level.<sup>7</sup> Because the cross sections at high leptoquark masses are extremely small, the MG5 results must be treated with caution, as the reliability of the numerical integration at such small values is susceptible to fluctuations.

---

<sup>7</sup>Here, we fixed the MG5 seed to 30, alternative seeds produce visibly different patterns. They are studied in Appendix D.

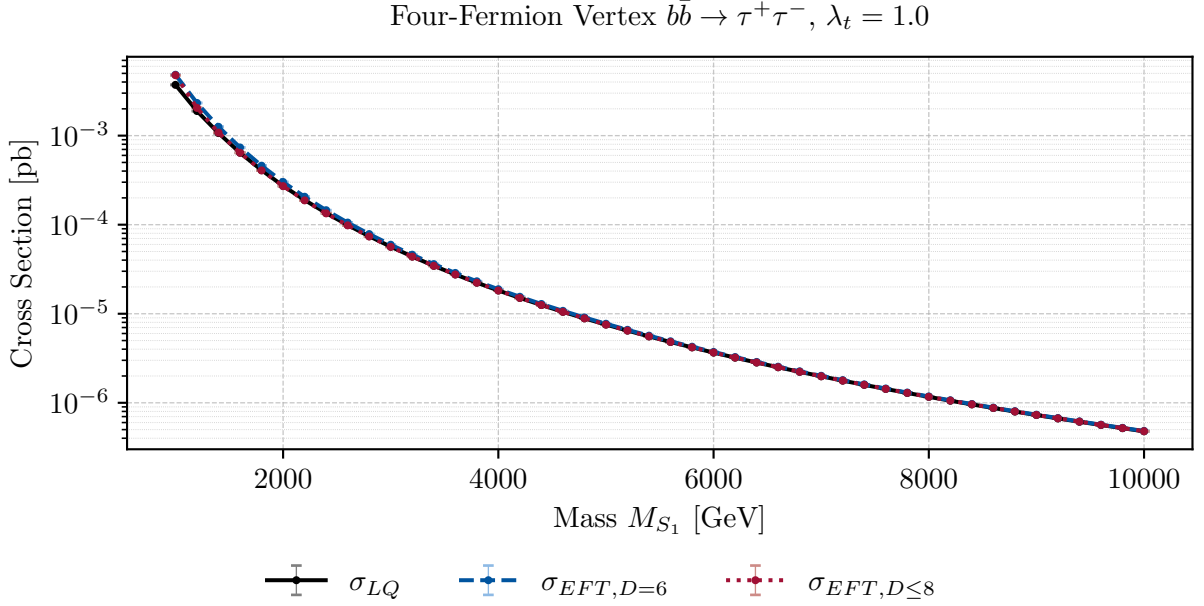


FIGURE 4.4: Comparison of  $\sigma(b\bar{b} \rightarrow \tau^+\tau^-)$  in full BSM theory (black) and in EFT at  $D = 6$  (blue) and  $D \leq 8$  (red), for  $\lambda_t = 1.0$ . Results are shown for leptoquark masses between 1 and 10 TeV. (see Figure C.1 for  $\lambda_t = 1.7, 2.5$ )

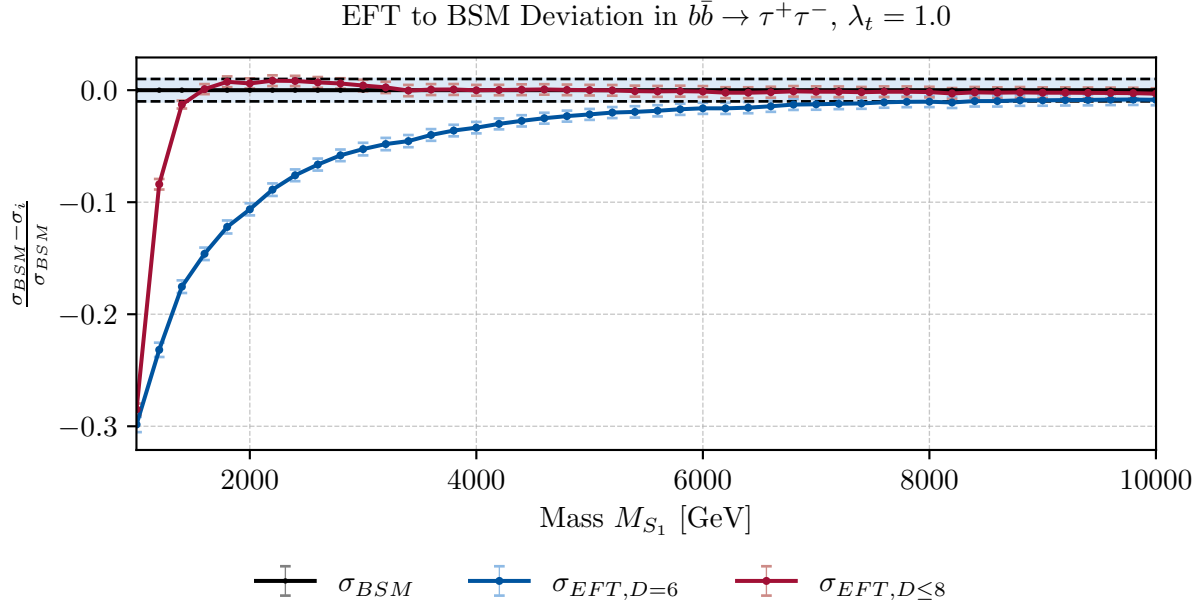


FIGURE 4.5: Relative deviation of the EFT predictions with respect to the full BSM theory with their statistical uncertainty, for  $\lambda_t = 1.0$ . The blue area indicates a deviation below 1%. (see Figure C.2 for  $\lambda_t = 1.7, 2.5$ )

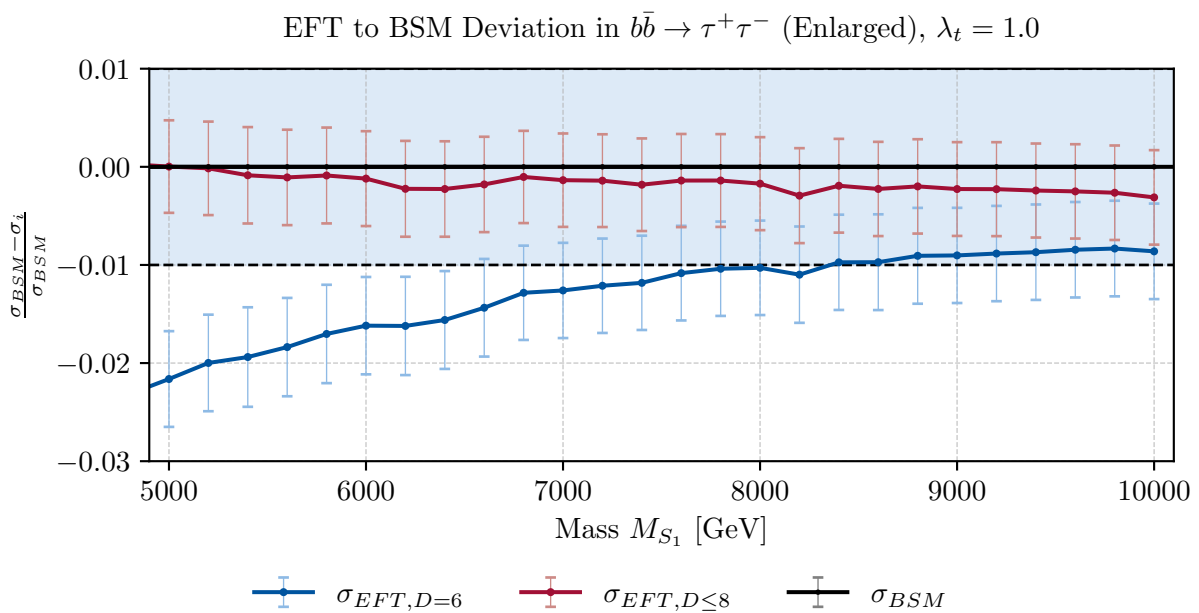


FIGURE 4.6: Relative deviation of the EFT predictions with respect to the full BSM theory and their propagated statistical uncertainty, for  $\lambda_t = 1.0$ . The blue band indicates the  $\pm 1\%$  accuracy interval. (see Figure C.3 for  $\lambda_t = 1.7, 2.5$ )

### 4.3.1 Theoretical Result: HighPT

To validate the reliability of the EFT description beyond numerical artifacts, we also make use of the HighPT tool [28], which provides an analytic result of the ratio between EFT predictions and the full BSM result. In Figure 4.7, we present our simulation results alongside the results obtained using HighPT.

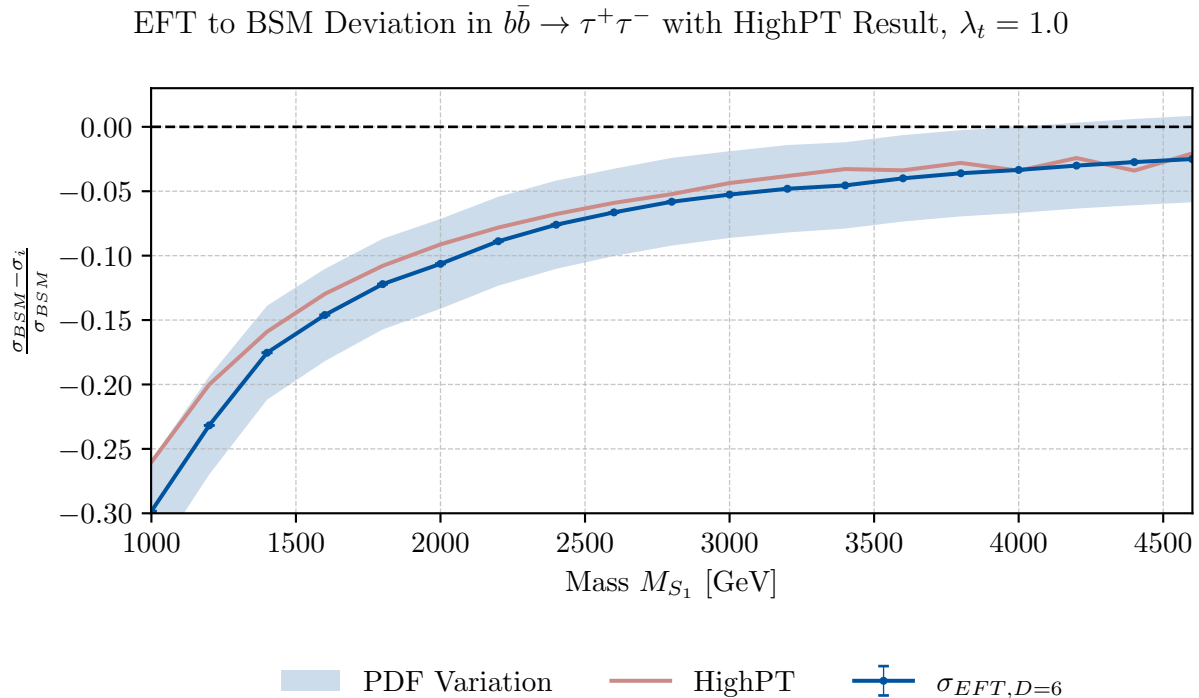


FIGURE 4.7: Relative deviation of the EFT predictions for dimension 6 (left), compared with the analytic result from HighPT. In addition to the statistical uncertainty of the cross section, MG5’s estimation of PDF dependence is presented.

Due to strong statistical instabilities of the tool for masses above  $M_{\tilde{S}_1} \gtrsim 4600\text{GeV}$ , we restrict the presentation to the lower mass range. The HighPT results reproduce the overall shape of the simulated deviations, thereby supporting the validity of our numerical analysis. In MG5, an additional estimate of the PDF dependence of the cross section is provided. This was not included in the previous plots because the same PDF set was used throughout. Since HighPT employs a different PDF set, we include the PDF-variation band for comparison. Within this PDF-variation band, the HighPT result and our simulation are consistent.

### 4.3.2 $\lambda_t$ Dependence of Relative Deviation

Finally, we explicitly want to verify the claim from Equation (4.18), that the relative deviation must be  $\lambda_t$  independent. For that, we define a function  $F(x, D)$ , the difference between the relative deviation of  $\lambda_t = x$  and  $\lambda_t = 1.0$ :

$$F(x, D) = \frac{\sigma_{\text{BSM}} - \sigma_{\text{EFT}, D}}{\sigma_{\text{BSM}}} \Big|_{\lambda_t=x} - \frac{\sigma_{\text{BSM}} - \sigma_{\text{EFT}, D}}{\sigma_{\text{BSM}}} \Big|_{\lambda_t=1.0}. \quad (4.19)$$

And plotting  $F(x, D)$  for  $x \in \{1.7, 2.5\}$  and  $D \in \{6, 8\}$ , we have:

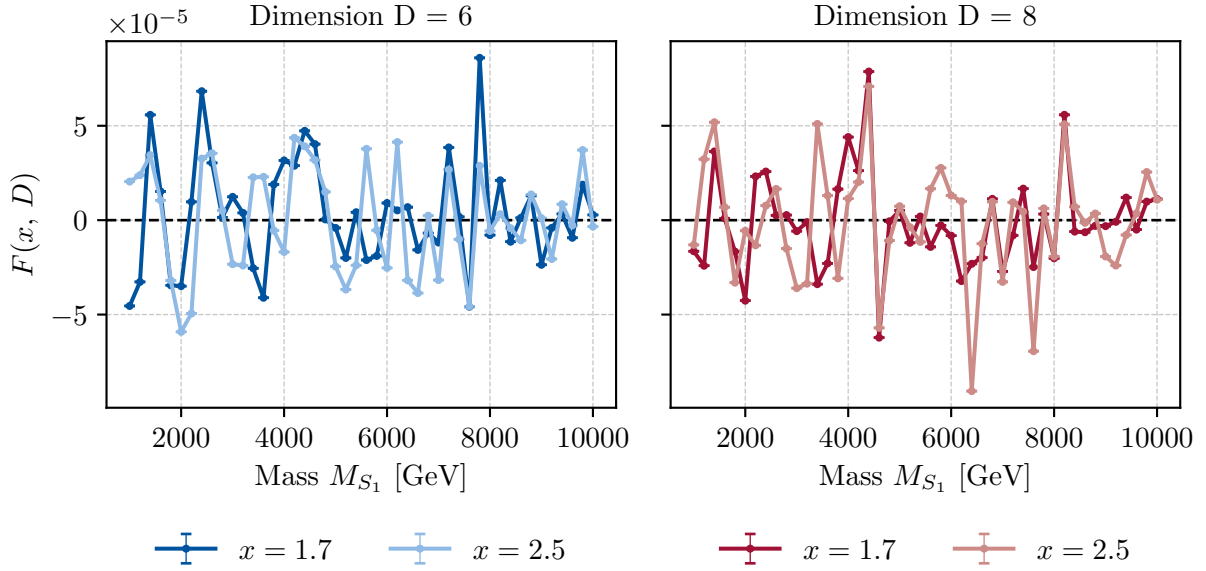


FIGURE 4.8: Comparison of the relative deviations according to Equation (4.19) for different  $\lambda_t$  for dimension 6 (left) and dimension 8 (right). For clarity, the statistical uncertainty is not shown.

The differences are consistent with zero within numerical precision, at the level of  $\mathcal{O}(10^{-5})$ , i.e. three orders of magnitude below the statistical uncertainties. Later, in the analysis of the cross section for the final state including one  $b$  quark, we will see that this  $\lambda_t$  (in)dependency can be traced back to the channel in which the  $\tilde{S}_1$  was mediated.

### 4.3.3 Differential Cross Section for Invariant Mass $m_{\tau^+\tau^-}$

In Figure 4.9, we present the (binned) differential cross sections. More precisely, we show how the invariant masses of the leptons in the final state  $m_{\tau^+\tau^-}$  affect the convergence between the EFT and BSM models for different leptoquark masses  $M_{\tilde{S}_1}$ . Differential cross sections are obtained for five  $m_{\tau^+\tau^-}$  intervals ( $0 - 500, 500 - 1000, 1000 - 1500, 1500 - 2000, 2000 - 2500$  GeV) by constraining the dilepton masses in MG5. Starting with low LQ masses and a high invariant mass, we see that both EFTs deviate largely from the BSM prediction. The reason is that in this case, the EFT expansion parameter  $E/\Lambda \sim m_{\tau\tau}/M_{\tilde{S}_1}$  ceases to be small, so the expansion is no longer reliable. Especially, if  $M_{\tilde{S}_1}$  is below  $m_{\tau^+\tau^-}$ , the EFTs strongly deviate from the BSM theory. In contrast, for smaller  $m_{\tau^+\tau^-}$  or larger  $M_{\tilde{S}_1}$ , the expansion parameter improves, and the EFT converges to the BSM model. **Note:** the cross-section scale on the  $y$ -axis differs between the  $M_{\tilde{S}_1}$  choices.

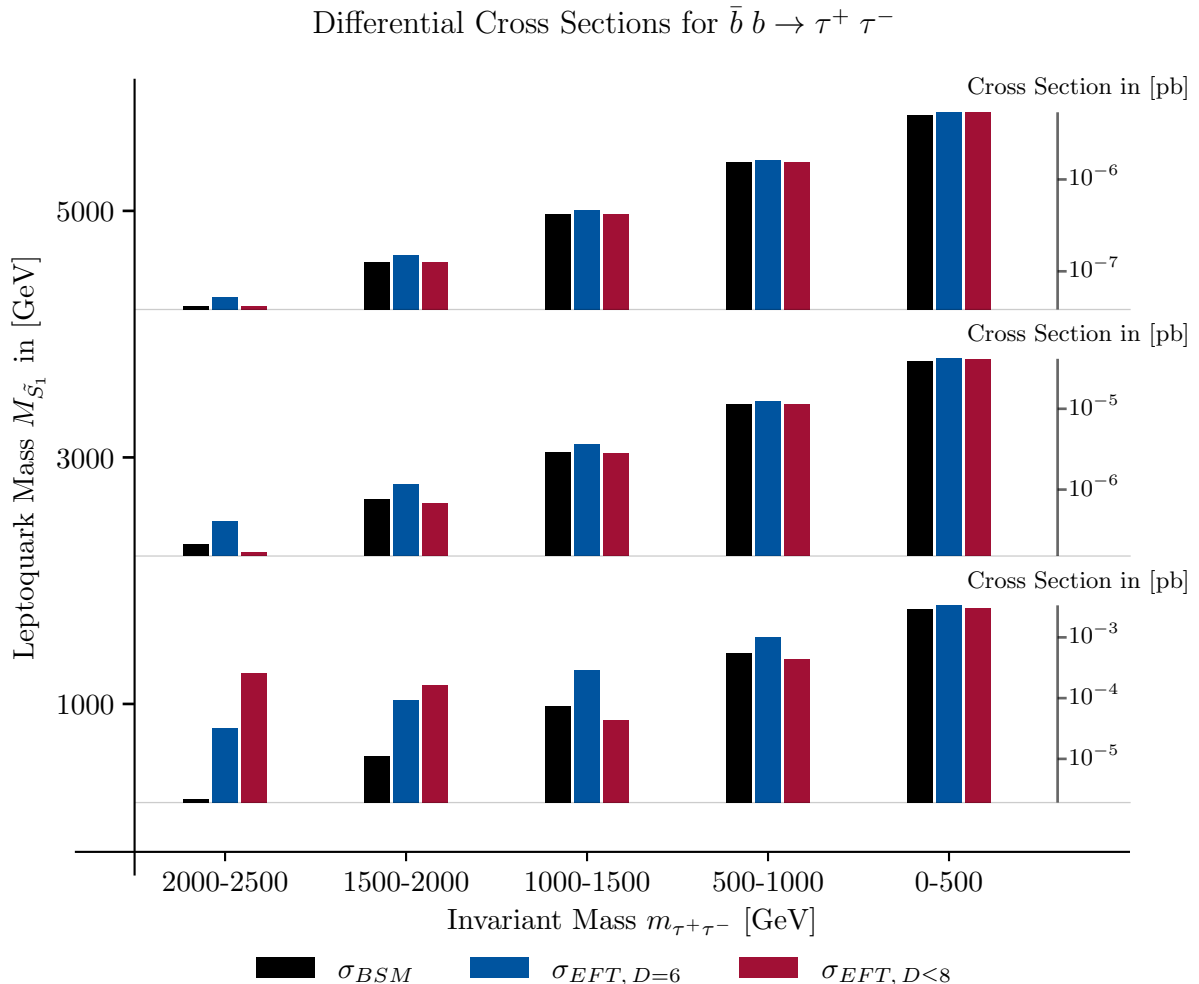


FIGURE 4.9: Binned differential  $pp \rightarrow \tau^+\tau^-$  cross sections as a function of  $m_{\tau^+\tau^-}$  for fixed  $M_{\tilde{S}_1}$ . Differential cross sections are given for BSM, EFT truncated at order 6 and at order 8 ( $\lambda_t = 1.0$ ).

## 4.4 Hadronic Interaction with one final state $b$ -quark:

$$pp \rightarrow \tau^+ \tau^- b$$

In the 5FS, three tree-level topologies contribute to  $pp \rightarrow \tau^+ \tau^- b$ . Due to  $CP$  invariance, the channel with a final-state  $\bar{b}$  has the same total cross section up to PDF effects. We therefore show only the  $b$  case, and the results apply equally to  $\bar{b}$ . Below, we present the three different diagrams in the BSM theory and the corresponding diagram in the EFT limit.

- Diagram 1: Off-shell  $b$ -quark decay.** An off-shell  $b$  decaying via the BSM interaction into  $\tau^+ \tilde{S}_1$ , followed by  $\tilde{S}_1 \rightarrow b\tau^-$ . The EFT limit replaces the  $\tilde{S}_1$  propagator with local four-fermion operators.

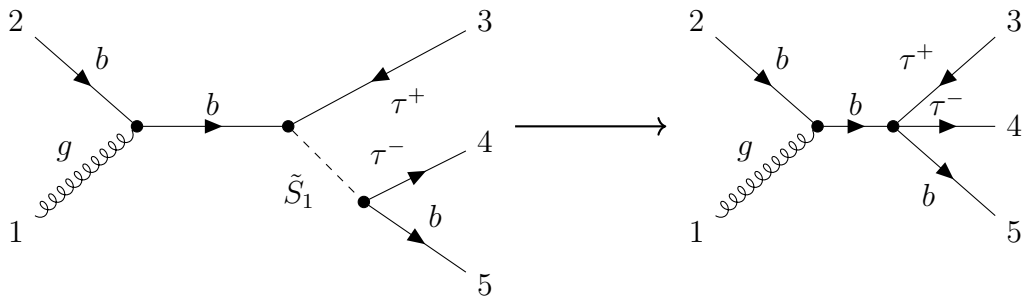


FIGURE 4.10: Diagram 1: Off-shell  $b$ -quark decay. BSM (left) and EFT (right).

- Diagram 2: Drell-Yan process.** Secondly, we have a Drell-Yan Process involving the exchange of a  $\tilde{S}_1$  in the  $t$ -channel. This topology will turn out to dominate  $pp \rightarrow \tau^+ \tau^- b$  for high  $M_{\tilde{S}_1}$ .

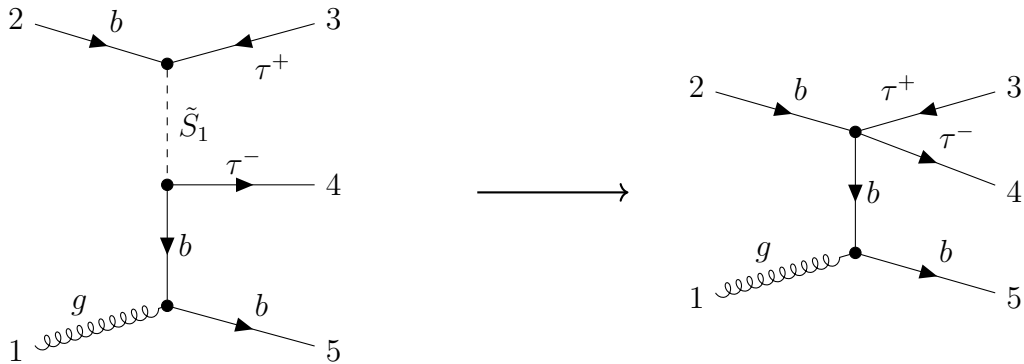


FIGURE 4.11: Diagram 2: Drell-Yan process. BSM (left) and EFT (right).

- 3. Diagram 3: Gluon-splitting** The gluon converts into two  $\tilde{S}_1$  scalars, of which one decays into the lepton-quark pair and the other is mediated in the  $t$  channel. Since two heavy propagators appear, this channel is suppressed by  $\mathcal{O}\left(\frac{1}{M_{\tilde{S}_1}^4}\right)$ .

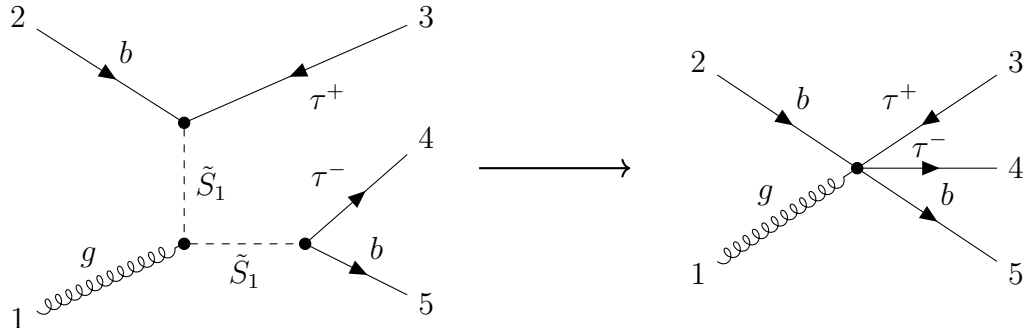


FIGURE 4.12: Diagram 3: Pair-production of two  $\tilde{S}_1$ . BSM (left) and EFT (right).

For the symmetric case with the  $\bar{b}$  quark in the final state, for all initial and intermediate particles, the antiparticle has to be taken.

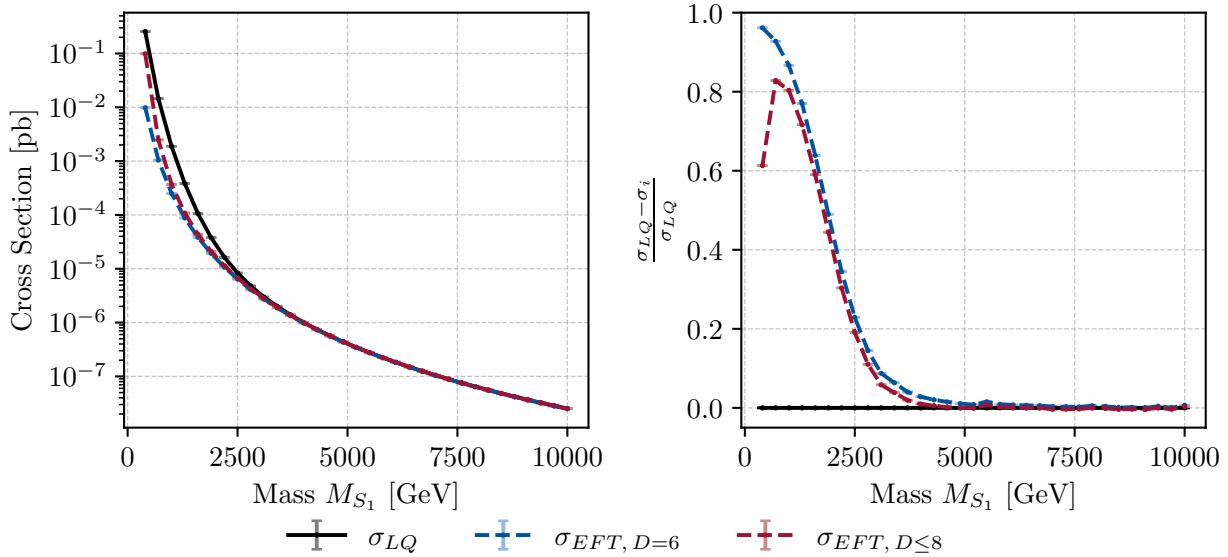
**Remark on EFT operator dimension.** The EFT diagrams in Figure 4.10 and Figure 4.11 are described by the four-fermion vertex discussed previously and are present at  $D = 6$  and  $D = 8$ . The vertex in Figure 4.12 has a higher mass dimension and is therefore only present at  $D = 8$ .

### 4.4.1 Cross Section of the Individual Processes

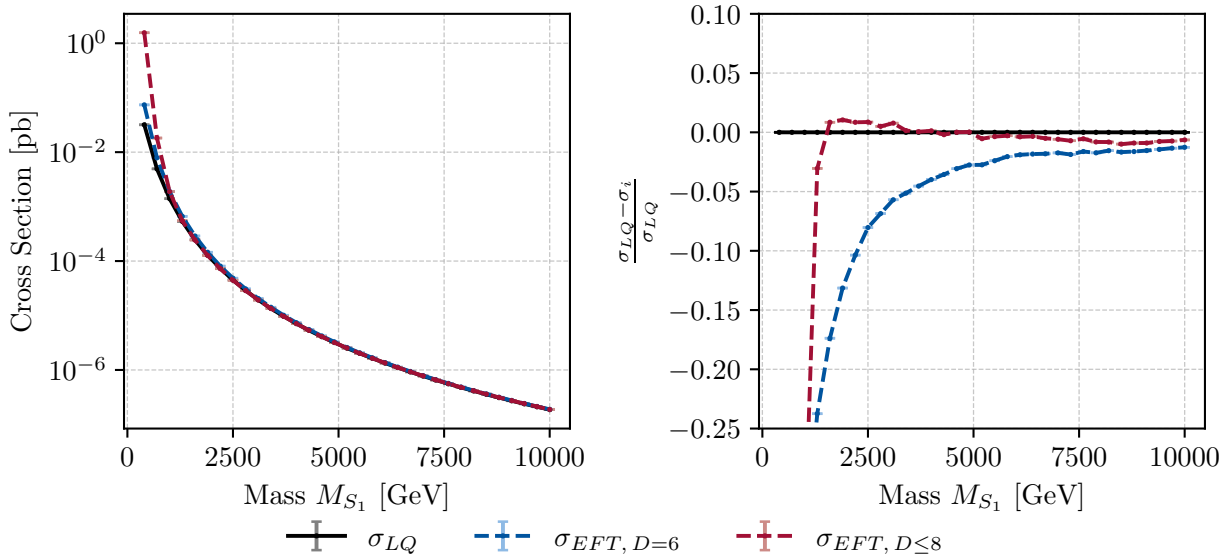
To compare the three topologies and their EFT convergence, in Figures (4.13a-4.13c), we present the absolute cross sections in the left panels and the relative deviation between EFT and BSM according to Equation (4.18) in the right panels. We use the same settings as in Table 4.2 and Table 4.3.

#### Discussion of Diagrams.

In Figure 4.13a, the EFT cross sections converge steadily to the BSM prediction  $\sigma_{LQ}$ . At dimension 8, the convergence initially worsens (at 700 GeV) before rapidly improving. With increasing  $M_{\tilde{S}_1}$ , the convergence of the dimension 6 and 8 to the BSM theory is quite similar. For the second diagram in Figure 4.13b, the contrast between the two orders is more pronounced. The EFT truncated at dimension 8 starts deviating more significantly than at dimension 6, but quickly converges to the BSM prediction. Already at  $M_{\tilde{S}_1} \simeq 1.6$  TeV the deviation falls below 2%. The  $D = 6$  expansion converges more slowly and only reaches comparable accuracy at  $M_{\tilde{S}_1} \sim 7$  TeV. Lastly, the gluon-splitting channel in Figure 4.13c shows the expected difficulty of approximating two heavy propagators by one vertex. While the prediction starts close to the BSM result at  $M_{\tilde{S}_1} = 400$  GeV, the deviation grows to above 90% around  $M_{\tilde{S}_1} \simeq 1.6$  TeV before steadily improving again, reaching 3% at  $M_{\tilde{S}_1} = 6$  TeV. Overall, the general expectations are confirmed. Both EFT orders converge towards the BSM theory as  $M_{\tilde{S}_1}$  increases, with the  $D \leq 8$  expansion consistently outperforming  $D = 6$  at high masses. In terms of hierarchy, the Drell-Yan process of Figure 4.11 dominates Figure 4.10 by roughly an order of magnitude, while the two- $\tilde{S}_1$  channel of Figure 4.12 remains subleading at large  $M_{\tilde{S}_1}$ . To examine whether the EFT convergence reaches the  $\pm 1\%$  level, in Figures (4.14a-4.14c), we provide enlarged views of the deviations. For Figure 4.14a, the  $D = 6$  and  $D \leq 8$  curves both agree with the BSM prediction within 1%. In Figure 4.14b, the curve  $D = 6$  does not quite reach the threshold value, but agrees reasonably well given the numerical uncertainties. Finally, in Figure 4.14c, the  $D \leq 8$  result remains slightly above the 1% band, which is expected, as the EFT at  $D \leq 8$  is the first order to cover the channel in the expansion.

Diagram: 1,  $\lambda_t = 1.0$ 

(A) Diagram 1

Diagram: 2,  $\lambda_t = 1.0$ 

(B) Diagram 2

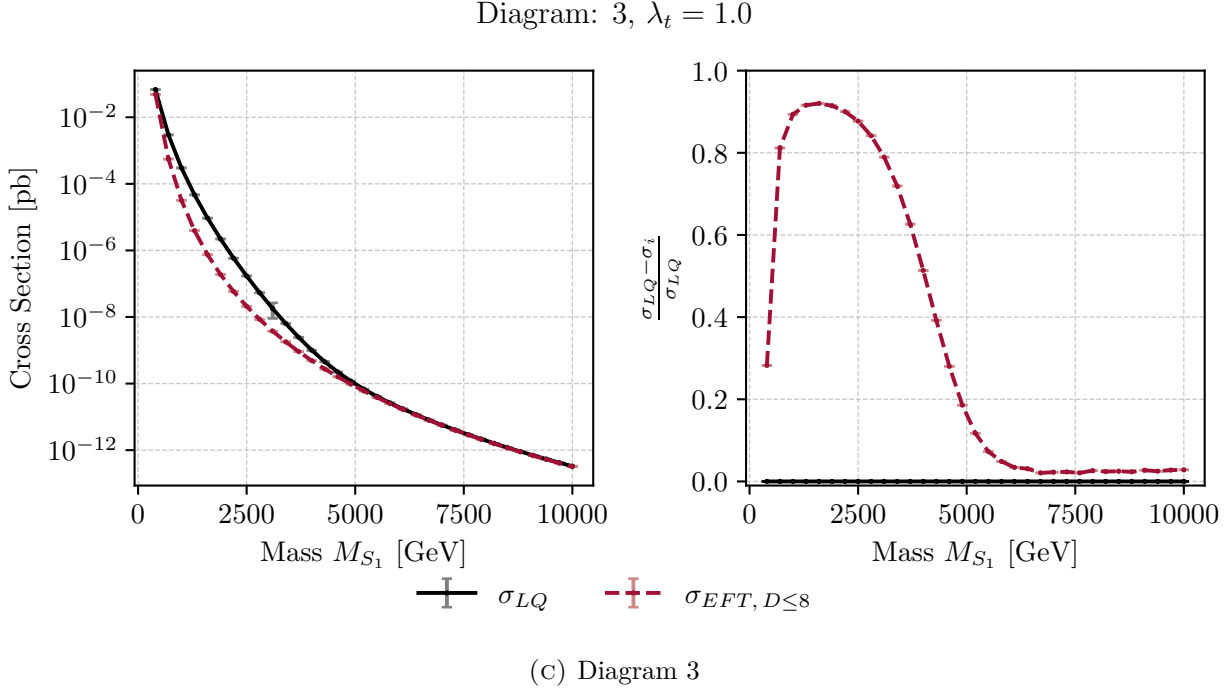
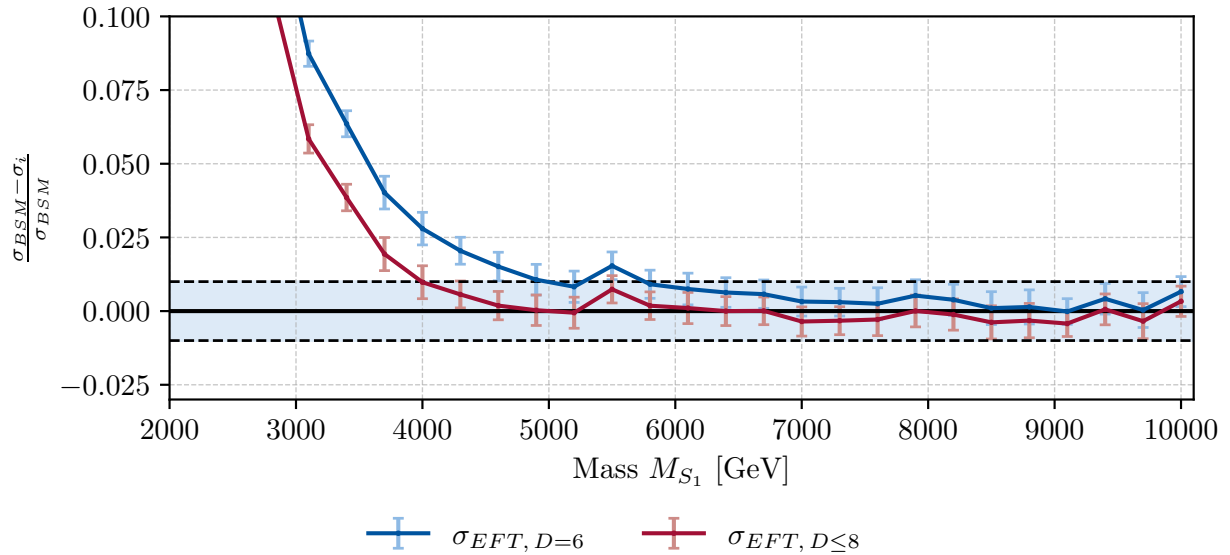
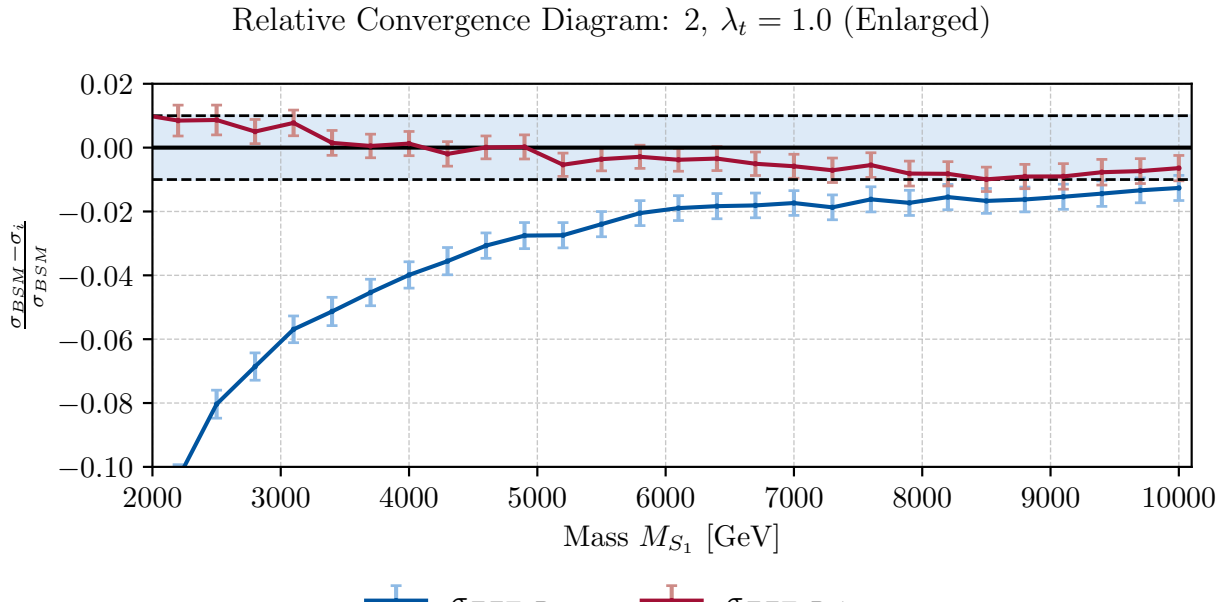


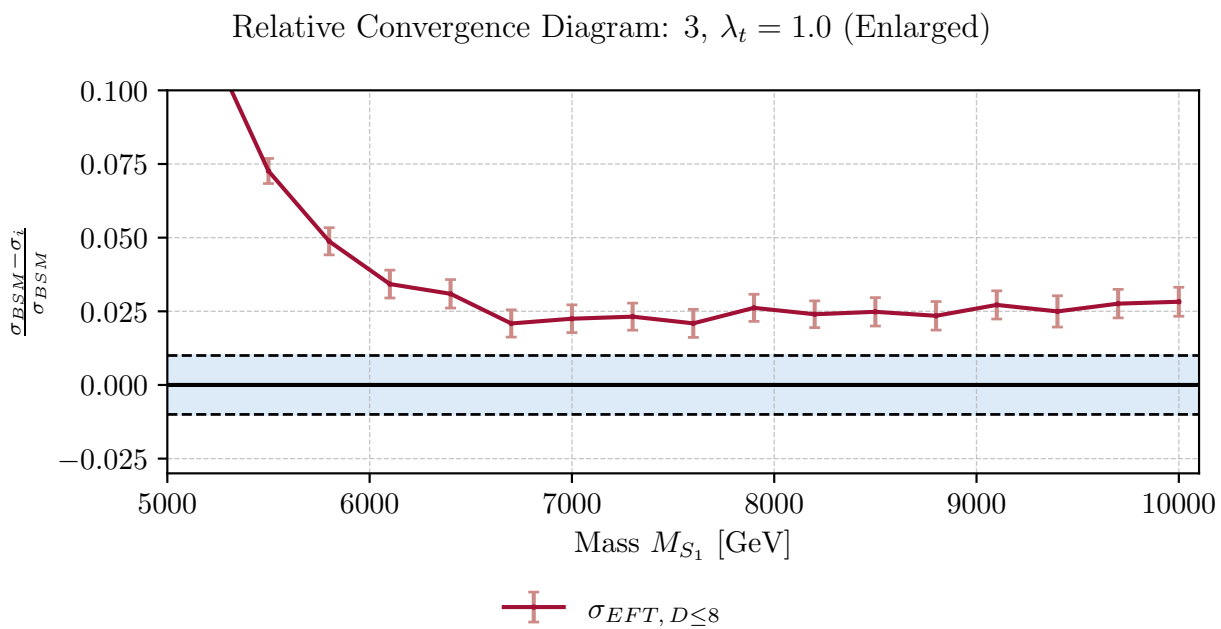
FIGURE 4.13: Comparison of cross sections for the three diagrams. On the left side, the absolute cross sections as a function of the leptoquark mass  $M_{S_1}$  for the BSM model  $\sigma_{LQ}$  and EFT at order  $D = 6$  and  $D \leq 8$ . On the right, the relative deviation  $\frac{\sigma_{LQ} - \sigma_i}{\sigma_{LQ}}$  for both EFT orders with respect to the full theory. (see Appendix C.2 for  $\lambda_t = 1.7, 2.5$ )

Relative Convergence Diagram: 1,  $\lambda_t = 1.0$  (Enlarged)





(b) Diagram 2: Relative Convergence



(c) Diagram 3: Relative Convergence with statistical uncertainties

FIGURE 4.14: Relative deviation  $\frac{\sigma_{LQ} - \sigma_i}{\sigma_{LQ}}$  for both EFT orders with respect to the full theory, including their statistical uncertainties as errorbars. (Enlarged View)

#### 4.4.2 Total Cross Section of $pp \rightarrow \tau^+ \tau^- b$

We now combine all three topologies, including their interferences, to obtain the full  $pp \rightarrow \tau^+ \tau^- b$  prediction in BSM and EFT:

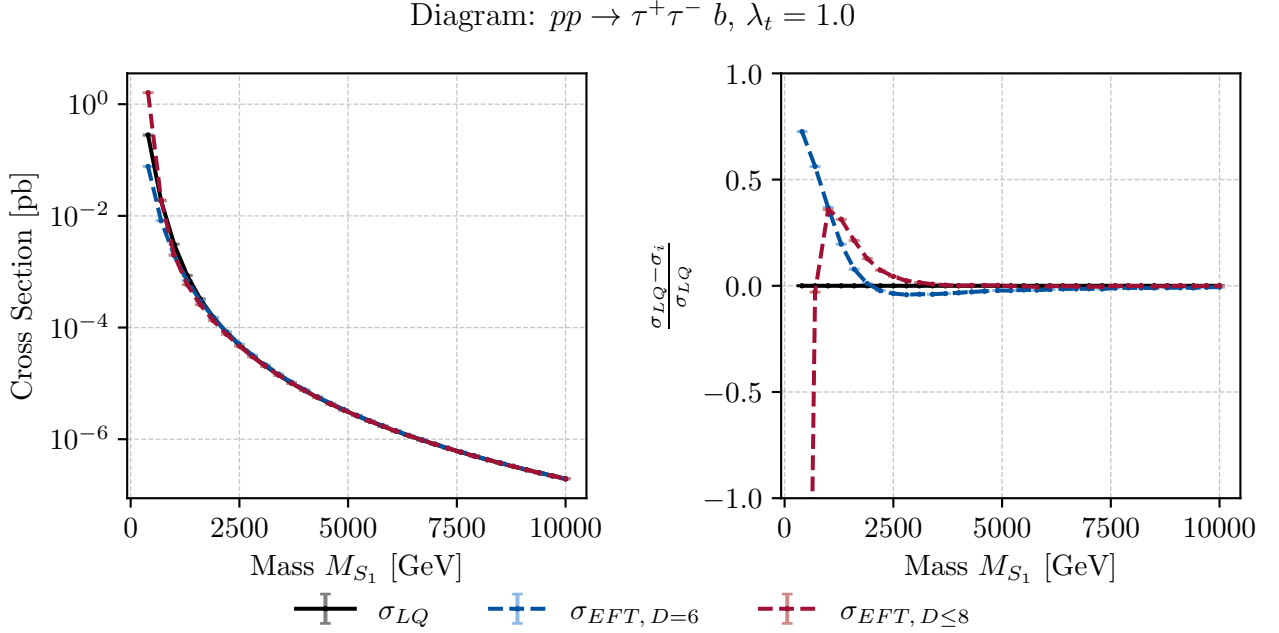


FIGURE 4.15: Comparison of cross sections for the hadronic process  $pp \rightarrow \tau^+ \tau^- b$ . On the left side, the absolute cross sections as a function of the leptoquark mass  $M_{S_1}$  for the BSM model  $\sigma_{LQ}$  and EFT at order  $D = 6$  and  $D \leq 8$ . On the right, the relative deviation  $\frac{\sigma_{LQ} - \sigma_i}{\sigma_{LQ}}$  for both EFT orders with respect to the full theory.

We observe that at low masses  $M_{S_1}$ , the dimension 8 EFT yields significantly larger deviations than the dimension 6 EFT. This behaviour was already seen in Figure 4.13b. As this diagram dominates, we expected it to affect the total cross section as well.<sup>8</sup> This behavior arises due to the additional momentum-dependent terms introduced by the dimension 8 Feynman rules. However, this discrepancy is mitigated at higher leptoquark masses above  $M_{S_1} \gtrsim 2500$  GeV, at which the dimension 8 cross sections coincide with the BSM theory (see Figure 4.16). Interestingly, within the intermediate mass range  $1100 \text{ GeV} \lesssim M_{S_1} \lesssim 2500 \text{ GeV}$ , the dimension 6 approximation provides a closer agreement with the BSM prediction than the dimension 8 approximation. This suggests the presence of an overcompensation effect in the dimension 8 corrections. Above this range, the dimension 8 converges fast to the BSM theory. Again, in Figure 4.16, we provide an enlarged view to check whether the EFT reaches the 1% threshold.

<sup>8</sup>It is worth noting that the cross section also includes interferences from the diagrams. However, any substantial deviations in the individual diagrams will likely be reflected in the total cross section as well.

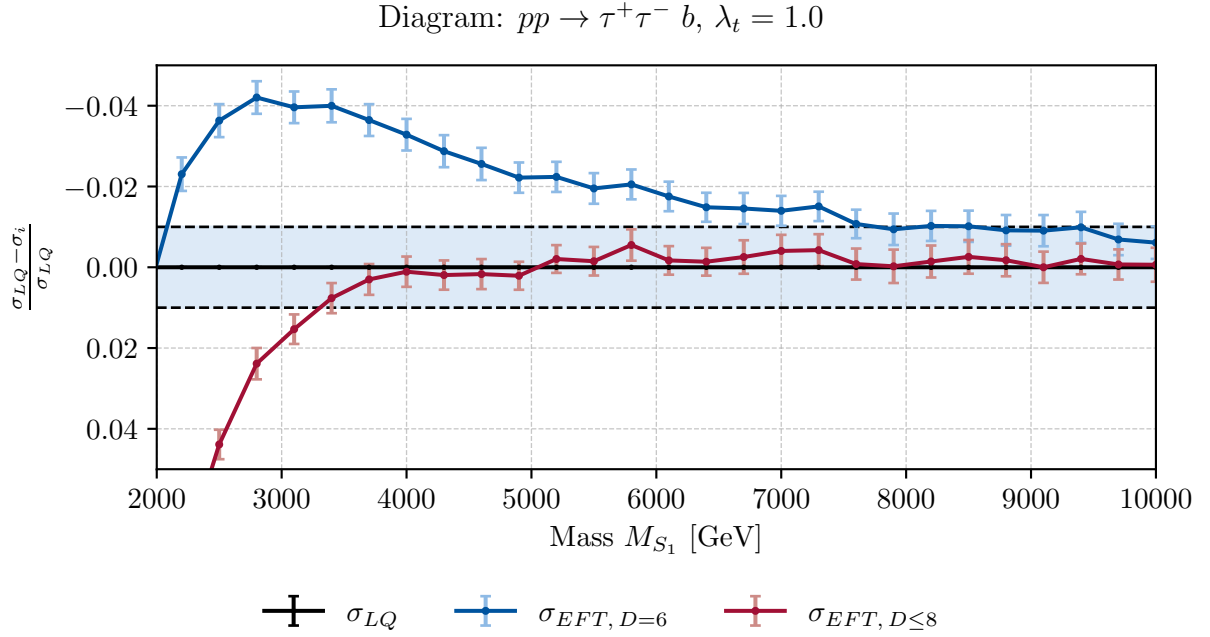


FIGURE 4.16: The relative deviation  $\frac{\sigma_{LQ} - \sigma_i}{\sigma_{LQ}}$  for both EFT orders with respect to the full theory. The light blue area indicates the area under which the deviation is below  $\pm 1\%$ .

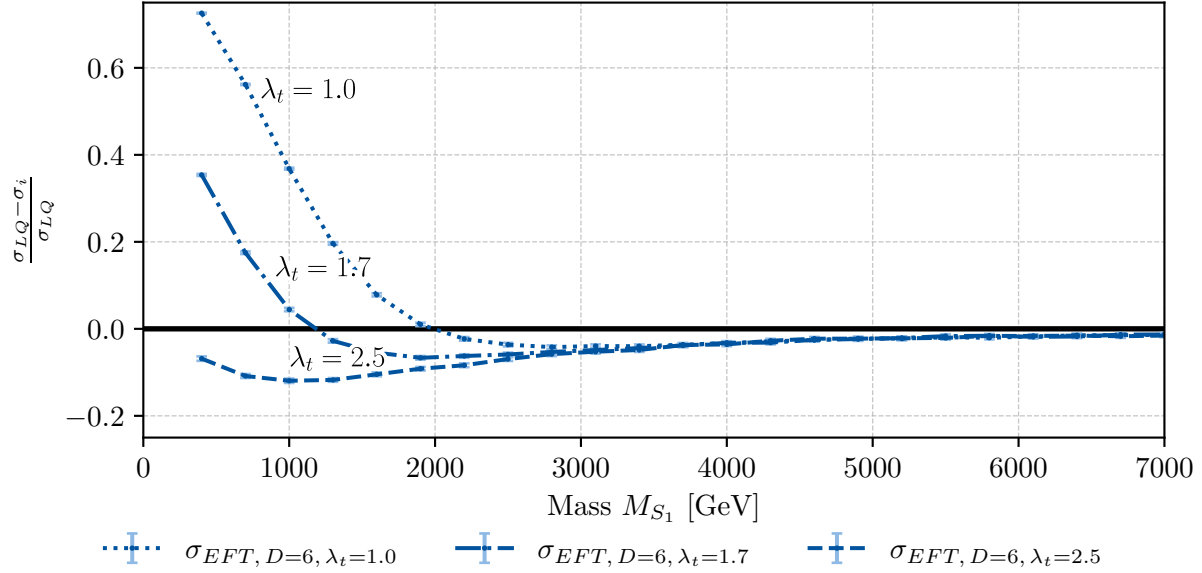
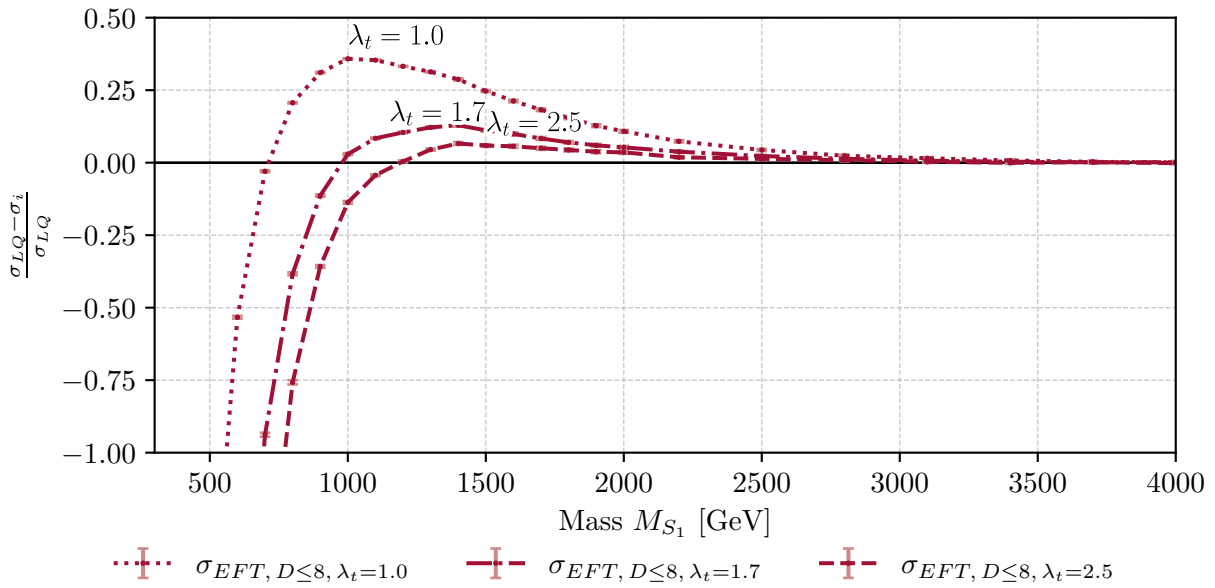
We see that the order 8 matches the BSM theory within the uncertainties above the LQ mass of  $M_{\tilde{S}_1} \gtrsim 3000$  GeV. For the order 6 expansion, the deviation is between 1 and 2%. Therefore, the EFT expansion for both dimension 6 and dimension 8 is in perfect agreement with the BSM theory.

#### 4.4.3 Cross Section dependence on $\lambda_t$

Until now, we have examined how the different channels contribute to the total cross section and how this depends on the LQ mass  $M_{\tilde{S}_1}$ , with  $\lambda_t = 1.0$  fixed. In Appendix C.2 we included the cross sections for  $\lambda_t = 1.7$  and 2.5. Now, we investigate directly how varying  $\lambda_t$  affects the BSM-EFT convergence. For the  $\bar{b}b \rightarrow \tau^+\tau^-$  channel, we already found that the convergence is independent of  $\lambda_t$  (see Section 4.3.2). For final states with an explicit  $b$ -quark,  $pp \rightarrow b\tau^+\tau^-$ , we generally expect a  $\lambda_t$ -dependence.

##### Total Cross Section of $pp \rightarrow b\tau^+\tau^-$

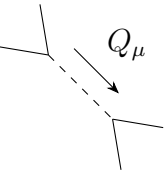
Both Figure 4.17 and Figure 4.18 support the claim that in  $pp \rightarrow \tau^+\tau^- b$  the deviation depends on  $\lambda_t$ . As  $\lambda_t$  increases, the relative deviation decreases, i.e., the EFT converges better to the full theory. To understand this dependence in detail, we now look at the cross section for the individual topologies of Figure 4.10 to 4.12.

EFT Dimension: 6, Diagram:  $pp \rightarrow \tau^+ \tau^- b$ FIGURE 4.17: Relative deviation  $\frac{\sigma_{LQ} - \sigma_i}{\sigma_{LQ}}$  for the hadronic process  $pp \rightarrow \tau^+ \tau^- b$ . Deviation of EFT at order 6 from BSM for  $\lambda_t = 1.0, 1.7, 2.5$ .EFT Dimension: 8, Diagram:  $pp \rightarrow \tau^+ \tau^- b$ FIGURE 4.18: Relative deviation  $\frac{\sigma_{LQ} - \sigma_i}{\sigma_{LQ}}$  for the hadronic process  $pp \rightarrow \tau^+ \tau^- b$ . Deviation of EFT at order 8 from BSM for  $\lambda_t = 1.0, 1.7, 2.5$ .

### Total cross section of individual processes

In Figures 4.19-4.23 we show the relative deviations of the three topologies contributing to  $pp \rightarrow \tau^+ \tau^- b$  for different  $\lambda_t$ . A clear pattern emerges: the first and third diagrams exhibit a  $\lambda_t$ -dependence, whereas the second diagram behaves analogously to the  $pp \rightarrow \tau^+ \tau^-$  case. In the second diagram, as well as in  $\bar{b}b \rightarrow \tau^+ \tau^-$ , the  $\tilde{S}_1$  is exchanged in the  $t$ -channel, and in the first and third, the  $\tilde{S}_1$  is transmitted in the  $s$ -channel. Therefore, it stands to reason that the  $\lambda_t$  dependence is connected to the propagator.

For the exchange of a scalar leptoquark  $\tilde{S}_1$  carrying momentum  $Q_\mu$  and total width  $\Gamma$ , the propagator with vertex factor reads<sup>9</sup>



$$(i\lambda_t) \Delta_{\tilde{S}_1}(Q^2) (-i\lambda_t) = (i\lambda_t) \frac{i}{Q^2 - M_{\tilde{S}_1}^2 + i M_{\tilde{S}_1} \Gamma} (-i\lambda_t). \quad (4.20)$$

The absolute value squared of the expression above, which is proportional to the squared amplitude, equals

$$|\mathcal{M}|^2 \propto \lambda_t^4 |\Delta_{\tilde{S}_1}(Q^2)|^2 = \lambda_t^4 \frac{1}{(Q^2 - M_{\tilde{S}_1}^2)^2 + M_{\tilde{S}_1}^2 \Gamma^2}. \quad (4.21)$$

In Figure 3.4 and Figure 3.5, we have seen that the Feynman rules for the EFTs scale as  $\lambda_t^2$ , and therefore  $|\mathcal{M}_{\text{EFT}}|^2 \propto \lambda_t^4$ . In the relative deviation between BSM and EFT, the  $\lambda_t^4$  is hence cancelled. However, as the decay width scales as  $\Gamma \propto |\mathcal{M}_{\text{decay}}|^2 \propto \lambda_t^2$ , it induces an additional uncancelled coupling dependency. Now there are two scenarios:

- **$\tilde{S}_1$  in  $s$ -channel:** In this channel, the LQ can go on-shell, and at resonance, we have  $Q^2 = M_{\tilde{S}_1}^2$ . This way the factor  $(Q^2 - M_{\tilde{S}_1}^2)^2$  vanishes and the denominator reduces to  $M_{\tilde{S}_1}^2 \Gamma^2$ . With  $\Gamma \propto \lambda_t^2$ , the deviation inherits a  $\lambda_t$ -dependence. For larger  $M_{\tilde{S}_1}$ , on-shell production becomes unfavorable, and the deviations for different  $\lambda_t$  converge.
- **$\tilde{S}_1$  in  $t$ -channel:** In this channel  $Q^2 < 0$  is strictly space-like and thus  $(Q^2 - M_{\tilde{S}_1}^2)^2$  never vanishes. The width term  $M_{\tilde{S}_1}^2 \Gamma^2$  is then negligible compared to  $(Q^2 - M_{\tilde{S}_1}^2)^2$ , and the deviation becomes effectively independent of  $\lambda_t$ .

In the third diagram, the gluon splits into two  $\tilde{S}_1$  lines: one can go on shell, while the other is exchanged in the  $t$ -channel. In this case, the coupling dependence from the  $s$ -channel  $\tilde{S}_1$  is suppressed by the  $t$ -channel  $\tilde{S}_1$ , leading to weaker coupling-dependencies than in the first diagram.

<sup>9</sup>For clarity, we have omitted writing the Lorentz and color structures.

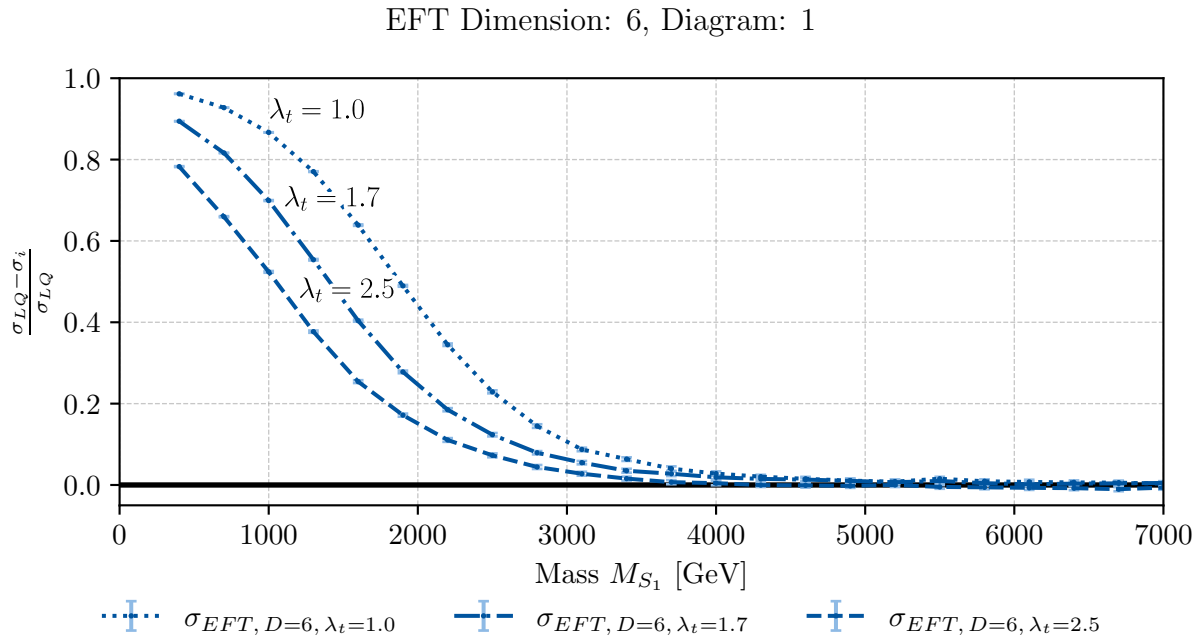


FIGURE 4.19: Relative deviation  $\frac{\sigma_{LQ} - \sigma_i}{\sigma_{LQ}}$  for Figure 4.10. Deviation of EFT at order 8 from BSM for  $\lambda_t = 1.0, 1.7, 2.5$ .

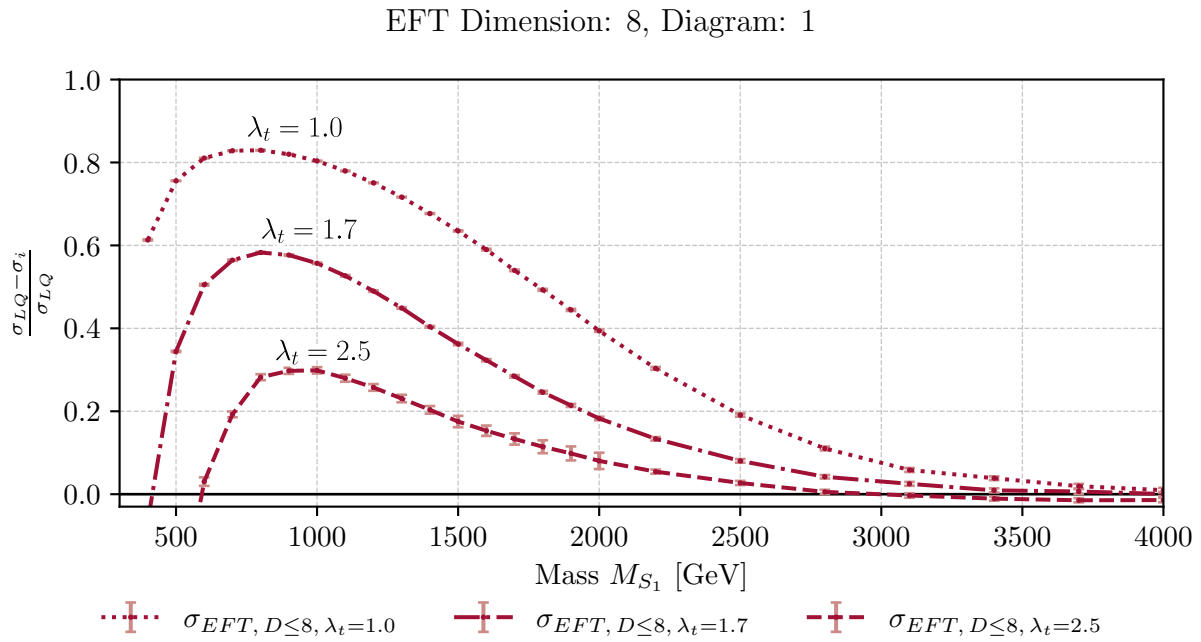


FIGURE 4.20: Relative deviation  $\frac{\sigma_{LQ} - \sigma_i}{\sigma_{LQ}}$  for Figure 4.10. Deviation of EFT at order 8 from BSM for  $\lambda_t = 1.0, 1.7, 2.5$ .

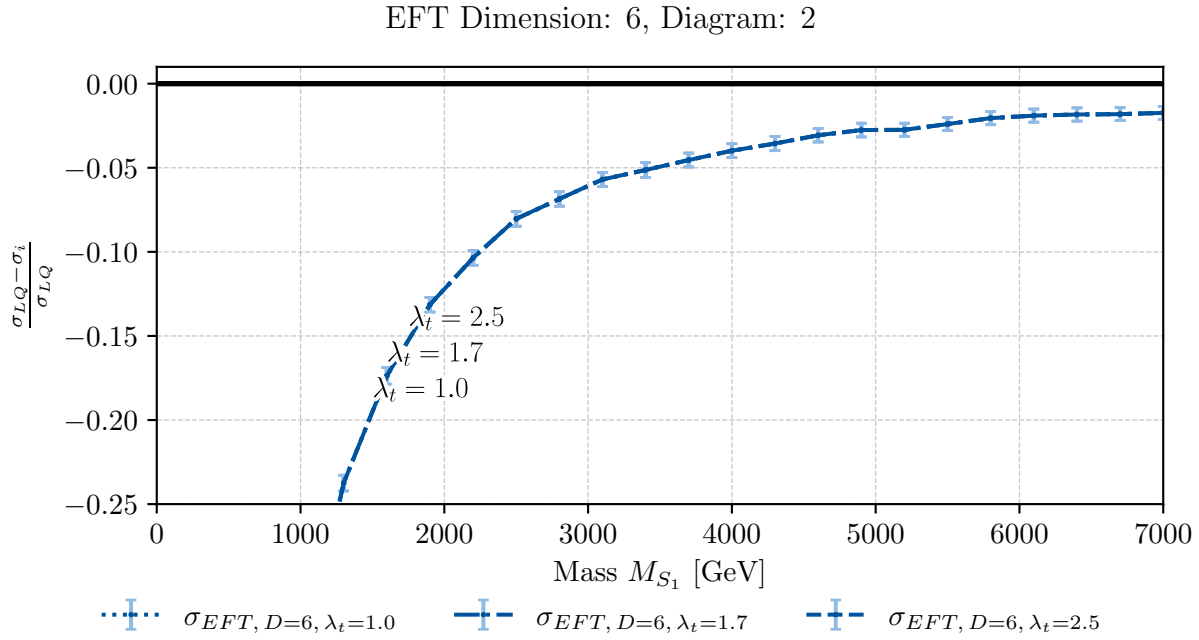


FIGURE 4.21: Relative deviation  $\frac{\sigma_{LQ} - \sigma_i}{\sigma_{LQ}}$  for Figure 4.11. Deviation of EFT at order 8 from BSM for  $\lambda_t = 1.0, 1.7, 2.5$ .

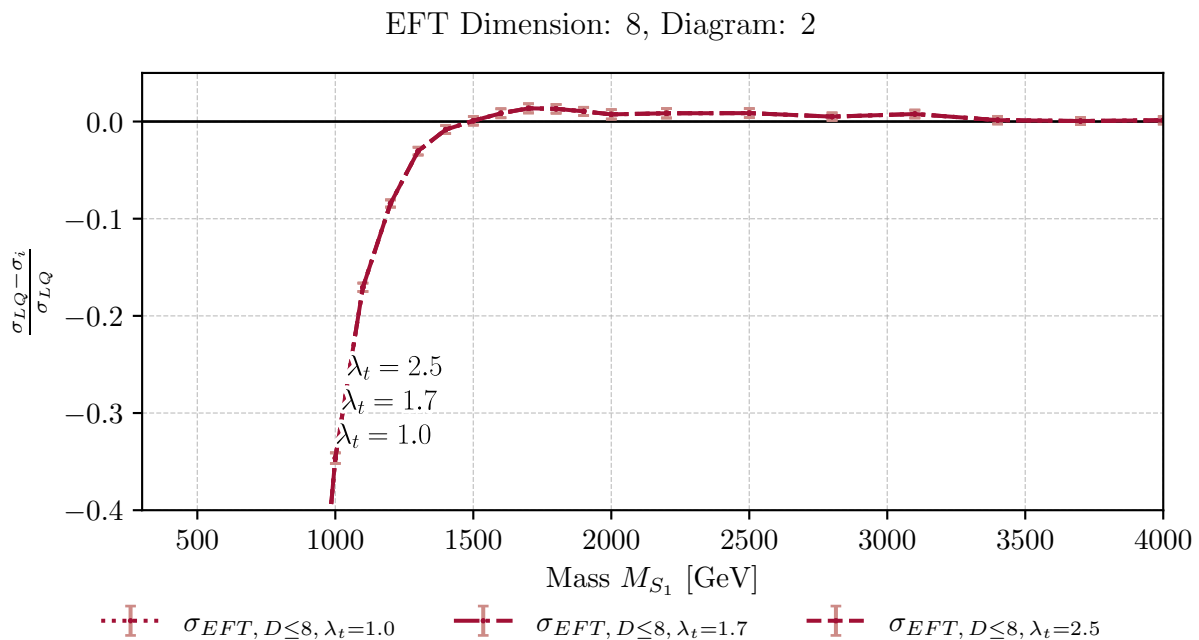


FIGURE 4.22: Relative deviation  $\frac{\sigma_{LQ} - \sigma_i}{\sigma_{LQ}}$  for Figure 4.11. Deviation of EFT at order 8 from BSM for  $\lambda_t = 1.0, 1.7, 2.5$ .

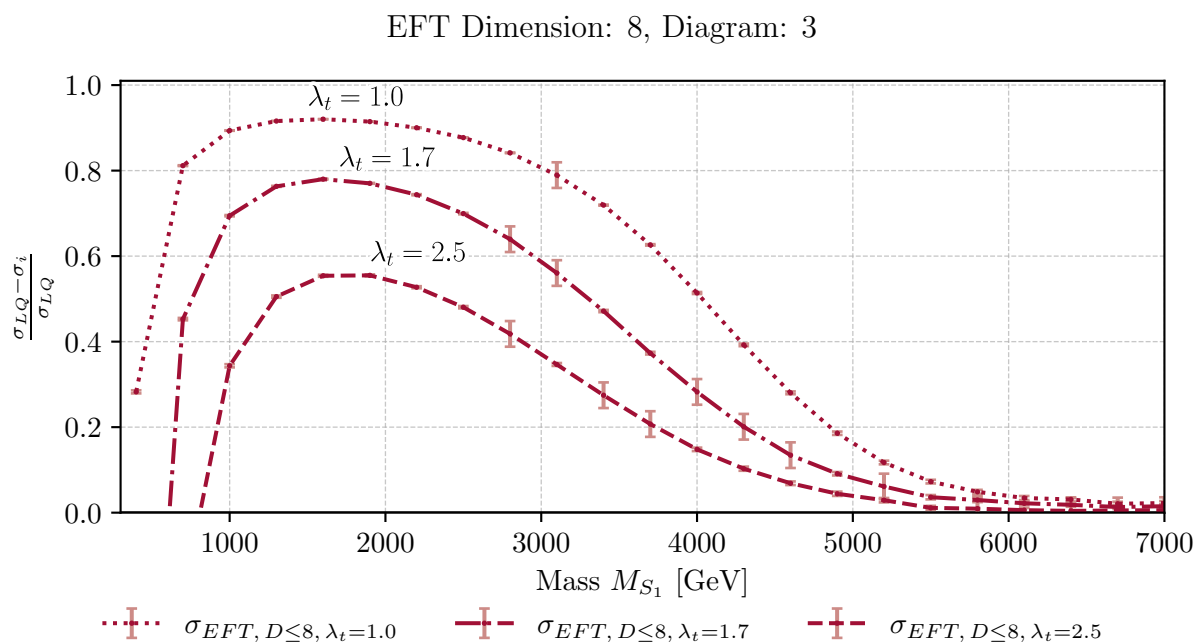


FIGURE 4.23: Relative deviation  $\frac{\sigma_{LQ} - \sigma_i}{\sigma_{LQ}}$  for Figure 4.10. Deviation of EFT at order 8 from BSM for  $\lambda_t = 1.0, 1.7, 2.5$ .



# Conclusion

The Standard Model, though remarkably successful, fails to address several fundamental open questions. These include questions such as dark matter and neutrino masses, as well as recent tensions in lepton flavor universality measurements that remain unexplained. One possible explanation for these tensions is the existence of leptoquarks, hypothetical particles that could mediate interactions between leptons and quarks. However, since no such particles have yet been discovered, their allowed parameter space has been pushed to masses well beyond the Standard Model scale. In these cases, EFT studies provide a framework to quantify the low-energy effects of heavy new particles. These studies can be done either model-independently or within the context of a specific BSM scenario.

In this thesis, we have developed an automated framework for EFT analyses and demonstrated its application to leptoquark production. To this end, we extended MATCHETE with a function that derives Feynman rules for a given Lagrangian, thereby streamlining the EFT study process.

Using the developed framework, we conducted a case study of the scalar leptoquark  $\tilde{S}_1$ . The primary objective of this analysis was to determine the domain of validity of the EFT description across different hadronic processes in high- $p_T$  LHC searches. In the study, we found that the EFT's reliability depends strongly on the mass of the heavy mediator. Increasing the mass generally improved convergence. This improvement was traced back to the expansion parameter being smaller, and therefore the EFT being a better approximation to the BSM theory. We further investigated the effects of truncating the EFT at different dimensions and saw that including higher-dimensional operators generally enhances agreement with the full theory. However, for lower leptoquark masses, the inclusion of higher-order terms can, in fact, worsen convergence when momentum-dependent contributions make the expansion parameters large. We have also observed that some diagrams generated by the BSM theory are not included in all orders of the EFTs, as the mass dimensions of the vertices may exceed the truncation order.

Interestingly, we observed that, in some instances, the EFT convergence is independent of the coupling strength between the leptoquark and SM fields. This behavior was traced back to the specific production channels of the leptoquark in the BSM theory, providing a physical explanation for the observed behavior.

Although the workflow was illustrated using a specific scalar leptoquark model, the methodology is fully general and can be applied to other BSM scenarios as well. Nonetheless, certain limitations remain. The precision of the numerical simulations may still be affected by uncertainties related to the choice of renormalization and factorization scales, as well as by the statistical accuracy of the Monte Carlo simulations.

This being said, the framework presented here can be extended. We have implemented an automated procedure for generating tree-level Feynman rules; a logical extension is to generalize the workflow to next-to-leading order. In addition, although MATCHETE currently handles electroweak symmetry breaking in the SM and the SMEFT at dimension  $D = 6$ , adding support  $D = 8$  is a natural next step.

The framework developed in this thesis, which has already been tested with operators involving the charge-conjugation matrix  $C$ , could be extended to heavy-neutrino models. While all three seesaw mechanisms generate the same Weinberg operator at low energies, their EFT-BSM convergence can differ due to the distinct gauge and Lorentz structures of the heavy mediators. Exploring these cases would provide a concrete illustration of how IR-degeneracy influences EFT analysis.

Finally, the complete MATCHETE package, together with the Feynman-rule generation algorithm developed in this thesis and all MATHEMATICA notebooks, are publicly available in my [GitHub repository](#).

## *Acknowledgements*

First and foremost, I would like to thank Felix Wilsch and Prof. Michael Krämer for the opportunity to work on this project and for their guidance throughout. I am especially grateful to Felix for the time and patience he invested whenever I was stuck or needed advice. I also thank the institute for its welcoming atmosphere and for the unforgettable debates over European flag designs, penguins, and German Bundesländer, which will always remain a fond memory.

Special thanks go to my office mates: Mareike, Matthias, Raphael, Theresa, and Luis, who always lent an ear when I was ranting about my MG5 installation or the vegetarian options at Mensa Vita on Fridays. In particular, I would like to thank my coworker, Luis Hourtz, for accompanying me on this journey and for providing the UFO implementation.

I am also grateful to Felix, Kilian, and Luis for proofreading my thesis multiple times and providing invaluable feedback.

I would also like to thank my aunt and her family in Fribourg for hosting me during my exchange year at EPFL. They welcomed me with open arms and more food than I could imagine, making me feel completely at home.

To all my friends in Aachen: thank you for making these years about more than just studying. From Beer on Campus to Döner at Elisenbrunnen, from Fridays at Great Houseparties to Inside Jokes about Kaiserplatz, from Library sessions until Midnight to Neglecting Overdue Papers, from Queueing for Robert Sauce at Templergraben cafeteria to Unplanned Vodka shots in Westpark, from taking the bus X73 to Yelling during rage cage up to Zoom calls in the morning. Everything happened with the best company I could ever wish for.

Lastly, and most importantly, I would like to thank my family. The past six years would not have been possible without their unwavering financial and emotional support. Knowing that they always had my back, in good times and bad, made all the difference.



## Appendix A

# The FeynmanRules Algorithm

In this chapter, we discuss the implementation of the algorithm that produces tree-level Feynman rules for a given Lagrangian  $\mathcal{L}$  and a specified Green's Function [input](#). In this chapter, we first provide a brief overview of the routine `FeynmanRules`. Thereafter, we discuss the implementation of each step and the conventions employed.

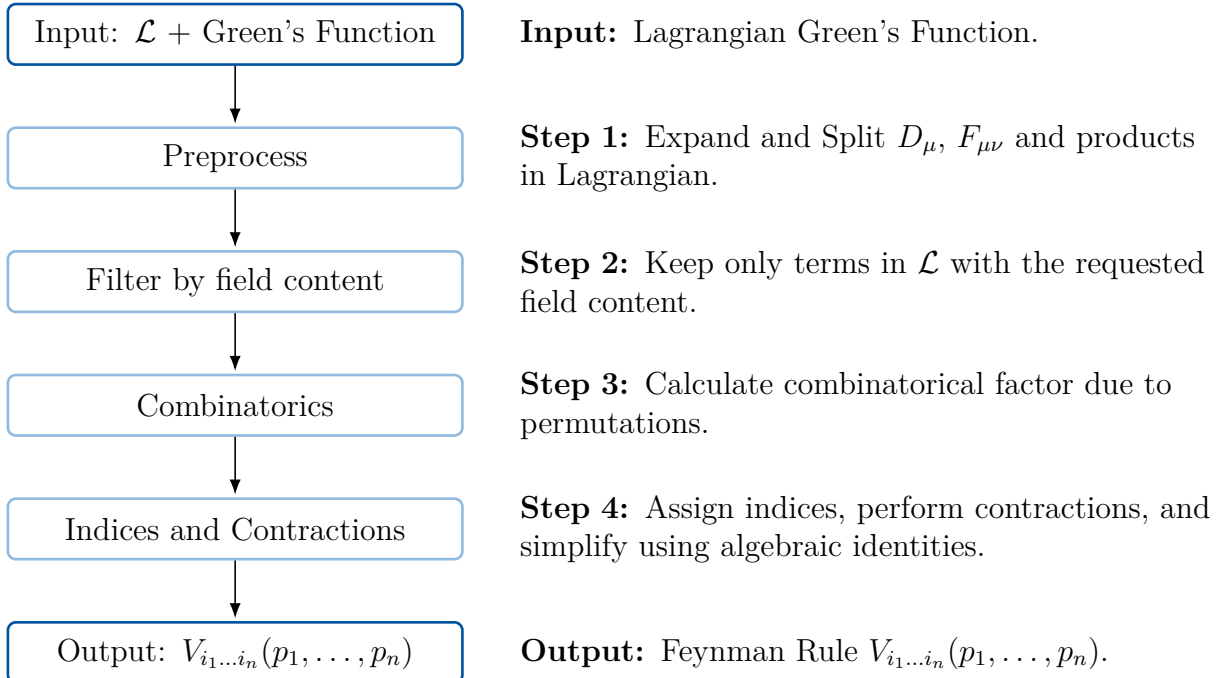
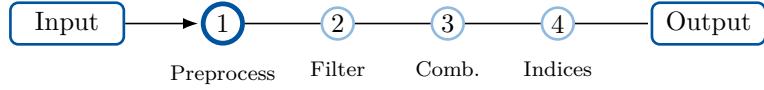


FIGURE A.1: Overview of the `FeynmanRules` Algorithm.

The outputs of the automated Feynman rule generator developed in this thesis were validated through the following checks:

1. **Independent Algorithm:** Cross-validation against an independently developed implementation by my co-worker.
2. **Literature:** Comparison of Feynman rules with known literature results [29].
3. **For LQ model:** Verification of the  $\tilde{S}_1$  Feynman rules against the FEYNRULES UFO model created by Dorsner et al. [6].

## A.1 Step 1: Preprocess



### Theoretical Formulation

MATCHETE models are generally written with covariant derivatives and field-strength tensors,

$$\mathcal{L} = \mathcal{L}(\varphi, D_\mu \varphi, F_{\mu\nu}, \dots),$$

which is ideal to ensure gauge and Lorentz invariance implicitly. For deriving Feynman rules, we instead need an explicit form in terms of partial derivatives and fields. Therefore the **Preprocess** step, rewrites

$$\mathcal{L}_{\text{int}}(\varphi, D\varphi, F) \longrightarrow \tilde{\mathcal{L}}_{\text{int}}(\varphi, \partial\varphi, A),$$

while paying attention to indices (group, Lorentz,...).

- Covariant Derivative:** For any field  $\varphi$  transforming in representation  $R_I$  of a non-Abelian group  $G_I$ , and with charges  $q_\varphi^{(J)}$  of the Abelian group  $U(1)_J$ , we define the covariant derivative as [7]

$$D_\mu \varphi = \partial_\mu \varphi - i \sum_I g_I A_\mu^{A(I)} T_{(R_I)}^{A(I)} \varphi - i \sum_J g_J q_\varphi^{(J)} A_\mu^{(J)} \varphi. \quad (\text{A.1})$$

non-Abelian part                            Abelian part

- Field-Strength Tensor:** Field-strength tensors for gauge bosons are

$$F_{\mu\nu}^A = \partial_\mu A_\nu^A - \partial_\nu A_\mu^A + g f^A{}_{BC} A_\mu^B A_\nu^C, \quad (\text{A.2})$$

with  $f^A{}_{BC} = 0$  for Abelian groups. When dealing with massive vectors that are no longer gauge fields (e.g. after SSB), we use the covariant derivatives

$$N_{\mu\nu}^A \equiv D_\mu Z_\nu^A - D_\nu Z_\mu^A, \quad (\text{A.3})$$

where the covariant derivative  $D_\mu$  is built from the unbroken gauge groups [30].

### Implementation in Matchete: `ExpandLagrangian`

In MATCHETEfields are saved as

```
In[2]:= Field[Name, Type, {Indices}, {CovariantDerivatives}]
```

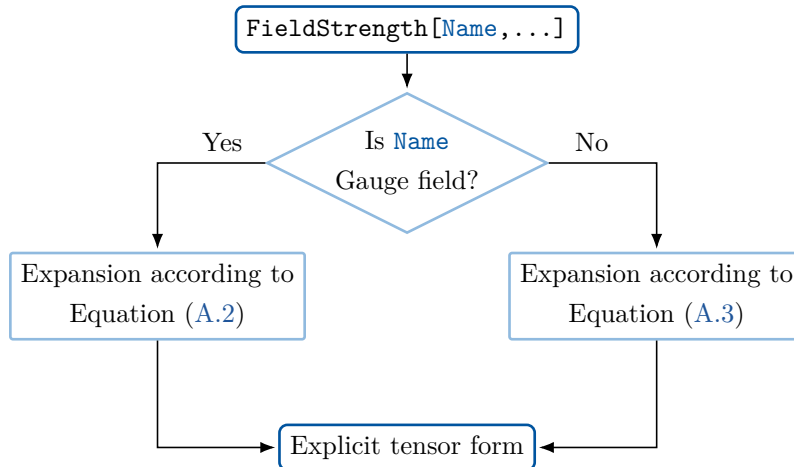
Field-strength tensors are saved as

```
In[3]:= FieldStrength[Name, {LorentzIndices}, {Indices}, {CovariantDerivatives}]
```

The list `{CovariantDerivatives}` holds any covariant derivatives acting on the field. Next, `{Indices}` holds group representations (but not Abelian charges). Additionally, for the field-strength tensor, `{LorentzIndices}` contains the two Lorentz indices of the tensor.

#### (i) Field-strength expansion (`ExpandFieldStrengthTensors`)

To expand every Field-strength tensor in the Lagrangian, we use the following steps



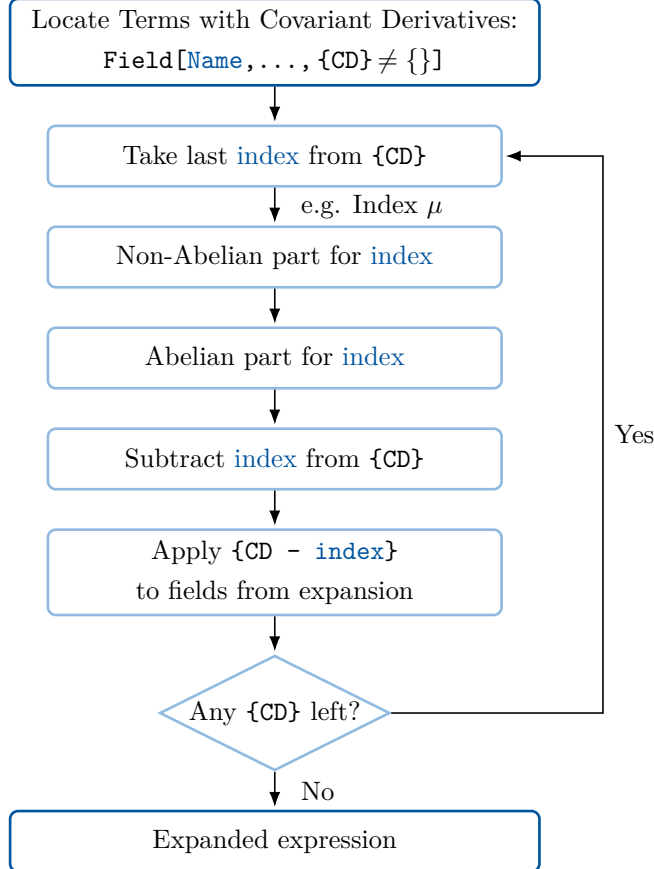
To replace every `FieldStrength[Name, ...]` by its explicit form, we need to identify whether the Field-`Name` corresponds to a gauge field or not. To do so, we find the list of groups and their corresponding gauge fields and couplings via

```
In[4]:= GetGaugeGroups[]
```

If Field-`Name` is in this list, we decompose it according to Equation (A.2).

## (ii) Covariant derivative split (`ExpandCovariantDerivatives`).

We proceed as follows to expand all the covariant derivatives in the Lagrangian.



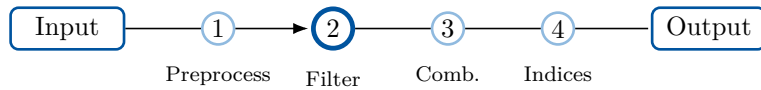
First, identify all covariant derivatives in the Lagrangian. In MATHEMATICA, we select every `Field[..., {CovariantDerivatives}]` with  $\{\text{CovariantDerivatives}\} \neq \{\}$ . We expand the last element of each such list first, since covariant derivatives generally do not commute [7]. To expand them according to Equation (A.1), we determine the relevant gauge groups and the field's transformation properties, and collect the corresponding coupling constants. For Abelian factors, we need the charges; for non-Abelian factors, the generators. Using the routine

```
In[5]:= GetFields[Name]
```

We can read off how the field `Name` transforms under its gauge groups. With these values, we expand the entries of the list `{CovariantDerivatives}` step by step. If the initial list contains multiple derivatives,  $\{\text{CovariantDerivatives}\} = \{\dots, \text{CD}_2, \text{CD}_1\}$ , we expand the last entry  $\text{CD}_1$  first. Next, for each term generated by the expansion, we apply the remaining derivatives  $\{\dots, \text{CD}_2\}$ , keeping in mind the product rule. In this way, the algorithm continues until no covariant derivatives remain in the Lagrangian.

To get the conjugate field in Equation (A.1), all we need to do is act with the `Bar[...]` routine on the term.

## A.2 Step 2: Filter by Field Content



### Theoretical Formulation

Only terms in the expanded Lagrangian that contain precisely the same fields as the specified external legs can contribute. We therefore count, for every term in the Lagrangian, the number of times each field appears and whether each occurrence is conjugated. Indices are ignored at this stage and will be managed later during externalization and contraction.

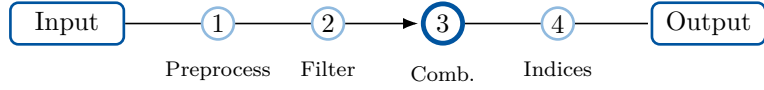
#### Implementation in Matchete: `FindCountofFields`

Let `input` be the external field list and `ExpandedLagrangian` the list of terms from  $\tilde{\mathcal{L}}$ .

1. **Collect fields from `input`.** Iterate over `input` and create list `{Name, count, isBarred}`. Each occurrence of `Field[Name, ...]` increments `count`. Because we distinguish a field from its complex conjugate, `isBarred` indicates whether the entry refers to the conjugated field. In MATCHETE, conjugation is denoted by `Bar[·]`.
2. **Collect fields per `term`.** For every `term` in `ExpandedLagrangian`, generate an analogous list `{Name, count, isBarred}` representing the fields present in that `term`.

Keep only those `terms` whose `{Name, count, isBarred}`-set is identical to that of the input.

### A.3 Step 3: Combinatorics



#### Theoretical Formulation

As mentioned earlier, the `input` list sets the Green's function order. Scalars and vectors commute with every object in the term. Fermions and ghosts are Grassmann numbers and thus anticommute.

We have seen in Section 2.3 that, in principle, we need to assign functional derivatives to the interaction term and sum over all permutations. Here, we first explain this for the case of an interaction term containing  $n$  identical commuting fields  $\phi_i$ . Given the  $n$ -point function with external points  $x_1, \dots, x_n$ , we have to evaluate

$$\frac{\delta^n}{\delta\phi_{a_1}(x_1) \cdots \delta\phi_{a_n}(x_n)} [\phi_{b_1}(y) \cdots \phi_{b_n}(y)] = \sum_{\sigma \in S_n} \prod_{k=1}^n \delta_{a_k b_{\sigma(k)}} \delta^{(4)}(x_k - y). \quad (\text{A.4})$$

On the right-hand side of the equation,  $\sum_{\sigma \in S_n}$  means we sum over every possible permutation of the list  $(1, \dots, n)$  (there are  $n!$  of them). For a given reordering  $\sigma$ , the list is  $\sigma = (\sigma(1), \dots, \sigma(n))$ . Thus  $\sigma(i)$  is simply the entry in the  $i$ -th position of that reordered list. If the  $\phi_i$  has no flavor or group structure, indices are the same for all, and  $\delta_{a_k b_{\sigma(k)}}$  equals 1 for all the cases. This then leaves us with an overall factor of  $n!$ , as there are  $n!$  elements in  $S_n$ .<sup>1</sup>

We illustrate this for  $n = 2$ :

$$\begin{aligned} \frac{\delta^2}{\delta\phi_{a_1}(x_1) \delta\phi_{a_2}(x_2)} [\phi_{b_1}(y) \phi_{b_2}(y)] &= \sum_{\sigma \in S_2} \delta_{a_1 b_{\sigma(1)}} \delta_{a_2 b_{\sigma(2)}} \delta^{(4)}(x_1 - y) \delta^{(4)}(x_2 - y) \\ &= \delta_{a_1 b_1} \delta_{a_2 b_2} \delta^{(4)}(x_1 - y) \delta^{(4)}(x_2 - y) \\ &\quad + \delta_{a_1 b_2} \delta_{a_2 b_1} \delta^{(4)}(x_1 - y) \delta^{(4)}(x_2 - y). \end{aligned}$$

This rule expands trivially for several types of commuting fields as well: First, start with the assignment of one kind, then keep the overall factor and do the assignment for the next, etc.

Generalizing this for Grassmann-odd fields, however, requires us to account for the signs that arise when anticommuting two Grassmann numbers. Suppose we start with a term

---

<sup>1</sup>This  $n!$  is commonly used to normalise vertex theories, e.g.  $\lambda/4!$  for  $\phi^4$  theories.

containing  $n$  identical anticommuting fields  $\psi_i$ :

$$\frac{\delta^n}{\delta\psi_{a_1}(x_1)\cdots\delta\psi_{a_n}(x_n)} \left[ \psi_{b_1}(y) \cdots \psi_{b_n}(y) \right] = \sum_{\sigma \in S_n} \text{sign}(\sigma) \prod_{k=1}^n \delta_{a_k b_{\sigma(k)}} \delta^{(4)}(x_k - y). \quad (\text{A.5})$$

Here  $\text{sign}(\sigma)$  is the sign that comes from applying the product rule for Grassmann numbers; each interchange of two Grassmann factors contributes a minus. It can be shown that

$$\text{sign}(\sigma) = \varepsilon_{\sigma(1)\sigma(2)\dots\sigma(n)}.$$

Two additional cases yield a sign when working with Grassmann numbers:

- Starting from a correlator with several types of functional derivatives, the formulas in (A.4) and (A.5) require the functional derivatives to be ordered so they can act consecutively. For anticommuting derivatives, it produces a sign. We therefore count the number of adjacent swaps of anticommuting fields to bring the **input** into the chosen external order. The resulting factor is

$$(-1)^{N_{\text{Swaps}}}.$$

- Consider a term in the Lagrangian with many fields, some of which are Grassmann fields. Suppose we have  $n$  functional derivatives of one Grassmann type  $\psi_i$ , and the corresponding  $\psi$ -fields in the term are not adjacent. In that case, each derivative picks up a sign for the number of Grassmann-odd factors it must pass to reach its target occurrence. Concretely, if the first derivative passes  $i$  Grassmann-odd factors and the second passes  $j$ , we get an additional factor  $(-1)^{i+j}$ . This repeats for the next field type and so on.

For example, let  $\chi, \eta, \psi$  be Grassmann-odd and  $\Phi$  be a scalar/vector. Take

$$\frac{\delta}{\delta\psi_{a_1}} \frac{\delta}{\delta\psi_{a_2}} \left[ \chi_{b_1} \eta_{b_2} \chi_{b_3} \Phi_{b_4} \psi_{b_5} \chi_{b_6} \psi_{b_7} \chi_{b_8} \eta_{b_9} \right] \quad (\text{A.6})$$

$$\rightarrow \left[ \chi_{b_1} \eta_{b_2} \chi_{b_3} \Phi_{b_4} \frac{\delta\psi_{b_5}}{\delta\psi_{a_1}} \frac{\delta\psi_{b_7}}{\delta\psi_{a_2}} \chi_{b_6} \chi_{b_8} \eta_{b_9} \right] - (a_1 \leftrightarrow a_2). \quad (\text{A.7})$$

Here  $\delta/\delta\psi_{a_2}$  must pass 5 Grassmann-odd factors to reach  $\psi_{b_7}$  (it crosses  $\chi, \eta, \chi, \psi, \chi$ ), and  $\delta/\delta\psi_{a_1}$  must pass 3 Grassmann-odd factors to reach  $\psi_{b_5}$  (it crosses  $\chi, \eta, \chi$ ), giving a global factor  $(-1)^{5+3}$ .<sup>2</sup> The additional minus in front of  $(a_1 \leftrightarrow a_2)$  comes from  $\text{sign}(\sigma)$  in (A.5).

---

<sup>2</sup>In the case where the term involves Grassmann numbers that are not Grassmann fields, the code accounts for the extra sign accordingly.

## Implementation in Matchete: `Feynman`

As the name suggests, the `Feynman` function plays a vital role. The code separately computes the combinatorial factors for different field types. The `Feynman` routine iterates over the field types: scalar, vector, fermion, and ghost. Starting with scalars

```
GatherFieldsByType[Lint, Scalar],
```

we obtain the list of all scalar fields in  $L_{\text{int}}$ , distinguishing complex  $\phi$  from  $\bar{\phi}$ . This list fixes the order in which the functional derivatives will be applied.<sup>3</sup>

For the first scalar species in the list, say  $\phi_a$ , let  $n$  be its number of occurrences in  $L_{\text{int}}$ . We create a list  $\{1, \dots, n\}$  and use the `Permutations` routine to get all its permutations. For each permutation, we create a copy of  $L_{\text{int}}$  in which the  $n$  occurrences of  $\phi$  are tagged with the  $n$  external labels (`EXT[·]`) according to the permutation. We repeat this independently for every scalar species. The output is the combinatorial factor for scalars.

**Example ( $n = 2$ ).** Assume  $L_{\text{int}}$  contains two occurrences of a real scalar  $\phi_a$  with some group index  $a$ . Concretely

$$L_{\text{int}} = \lambda(\partial_\mu \phi_a) \phi_b \mathcal{F}_{ab}^\mu.$$

Here,  $\mathcal{F}_a^\mu b$  depicts any field structure containing vectors, fermions, and even other scalars. As we have two scalars, there are  $n! = 2$  permutations. Via `Permutations` and `Range`, we get

$$\text{Permutations}[\text{Range}[2]] = \{\{1, 2\}, \{2, 1\}\}.$$

Now in  $L_{\text{int}}$ , given the permutation list, we assign the numbers to the fields  $\phi$  and put `EXT[·]` as a header, denoting that this field has been taken care of. That way, we are left with

$$\tilde{L}_{\text{int}} = \lambda(\partial_\mu \text{EXT}[\phi_1]_a) \text{EXT}[\phi_2]_b \mathcal{F}_{ab}^\mu + \lambda(\partial_\mu \text{EXT}[\phi_2]_a) \text{EXT}[\phi_1]_b \mathcal{F}_{ab}^\mu. \quad (\text{A.8})$$

Later, we will show how to adjust the term according to the field labels from the correlator, as well as how the partial derivatives will be handled. Before that, we explain the difference when dealing with fermions and vectors. In case of vectors, there is an additional Lorentz index that will be added to the `EXT[·]` argument. For fermions and ghosts, we need to incorporate the signs. We start with the signs due to permutations. To this end, for each `list of Permutations[Range[n]]`, we evaluate the corresponding entry of the rank- $n$  Levi-Civita tensor, `LeviCivitaTensor[n]`. This yields the sign associated with the permutation, which we then multiply by the respective term.

---

<sup>3</sup>For now, we ignore the order from the Green's function.

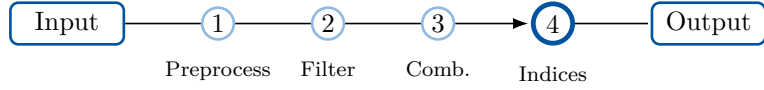
For global signs, we have two functions.

1. `ComputeGrassmannSignFromOrdering` calculates the sign due to ordering the input. It determines the number of adjacent swaps needed,  $N$ . The output is  $(-1)^N$ .
2. `newGrassmanncomparison[interactions, listfieldn]` calculates the Grassmann sign by checking the occurrences a functional derivative has to pass a Grassmann variable to end at the target field. Occurrences with `EXT[·]` are not counted.

Putting all together and iterating over all the fields, we have found the combinatorial factor for each term in the Lagrangian. Before adjusting the indices according to the external fields, we replace the partial derivatives according to Equation (2.40)

$$\partial_\mu \text{EXT}[\varphi_i]_a \rightarrow -ip_\mu^{\varphi_i} \text{EXT}[\varphi_i]_a.$$

## A.4 Step 4: Indices and Contraction



### Theoretical Formulation

After calculating the combinatorial factor of the vertex, we are left with a term where the placeholder external fields are contracted within the term. Now they need to be tied to the external leg, specified by the `input`.

For that, we first go through the `input`-list. Suppose we examine the  $k$ -th<sup>4</sup> instance of  $\phi$  in this list, which has the index  $i$ . Then, in the combinatorial factor, there will be a placeholder  $\text{EXT}[\phi_k]_a$  with a dummy-index  $a$ . The terms with the same  $k$  will be tied to each other, or put differently, the index  $i$  must be connected with  $a$ . Therefore, we do the following replacement involving Kronecker deltas

$$\text{EXT}[\phi_k]_a \longrightarrow \text{EXT}[\phi_k]_i \delta_{ia}.$$

If a field carries several indices, the replacement is applied index-wise:

$$\text{EXT}[\phi_k]_{a_1 \dots a_m} \longrightarrow \text{EXT}[\phi_k]_{i_1 \dots i_m} \delta_{i_1 a_1} \dots \delta_{i_m a_m}.$$

In the case of Lorentz indices, we use the metric tensor instead of Kronecker deltas.

### Implementation in Matchete: `AssignExternalFields`

The function `AssignExternalFields` builds a replacement that pairs exactly the external field to fields in the combinatorial factors. To do so from the fields in the combinatorial factor and `input`

`Field[ $\text{EXT}[\phi_k]$ ,  
type,  
{ $a, \dots$ },  
{ $\dots$ }]`  
Index List

the routine reads the `Index List` and creates the Kronecker deltas `CG[delta[Group], {i, a}]` for non-Lorentz indices. In case of Lorentz indices that occur in `type`, we tie them via `MetricTensor`<sup>5</sup>. Lastly, by applying the `Contract` routine, we obtain a simplified expression for the Feynman rules, which depends solely on the indices provided in the input and the dummy indices contracted within the term.

<sup>4</sup> $k$  is the index ranging from 1 to  $n_\phi$ .

<sup>5</sup>For example, if the placeholder was  $\text{EXT}[A_k]_\alpha$  and we had  $\text{EXT}[A_k]_\mu$  in the `input`, we replace it with  $\text{EXT}[A_k]_\mu \eta_{\mu\alpha}$  (in MATCHETE `MetricTensor[ $\mu, \alpha$ ] =  $\eta_{\mu\alpha}$` ).

## Appendix B

# MATCHETE: Electroweak Symmetry Breaking for $\tilde{S}_1$

### B.1 EWSB in the Standard Model

In this section, we implement EWSB for the  $\tilde{S}_1$  in MATCHETE. However, as  $\tilde{S}$  is a singlet under  $SU(2)_L$ , the modifications of EWSB for the LQ are straightforward. In this section, we follow the discussion of electroweak symmetry breaking (EWSB) as presented in [8]. For classes of BSM particles that are singlets under  $SU(2)_L$ , the steps remain almost the same. First, we need to define the electromagnetic gauge group  $U(1)_{\text{em}}$ . When defining the gauge group, we directly feed the name of the gauge field  $\mathcal{A}$  (photon) and the coupling of the gauge group  $e = \text{ge}$ . The `UFO$Options` is for MG5 to later identify this correctly as the photon from the standard model<sup>1</sup>

```
In[8]:= DefineGaugeGroup[U1em, U1, ge, A,
  UFO$Options -> <|"pdg" -> 22, "name" -> "A"|>];
```

Next, we define the couplings that arise after symmetry breaking. This include the  $Z$ -Boson coupling  $g_Z = \text{gZ}$ , as well as the Higgs vacuum expectation value  $v = \text{v}$  and CKM matrix  $V_{\text{CKM}} = \text{CKM}$ :

```
In[9]:= DefineCoupling[gZ, EFTOrder -> 0, Indices -> {}, SelfConjugate -> True];
DefineCoupling[v, EFTOrder -> 0, Indices -> {}, SelfConjugate -> True];
DefineCoupling[CKM, Indices -> {Flavor, Flavor}];
```

where  $\text{gZ}$  and  $\text{v}$  are real and have no group/flavor structure, and the CKM-matrix has two flavor indices. Next, we define the SM particles in the broken phase. We start with the  $Z$  and  $W$ -Bosons

---

<sup>1</sup>For further details on the Particle Data Group (PDG) numbering scheme and the complete list of SM particle identifiers, see [31].

```
In[10]:= DefineField[Z, Vector, SelfConjugate -> True, Mass -> Heavy,
UFO$Options -> <|"pdg" -> 23, "name" -> "Z"|>];
DefineField[W, Vector, Charges -> {U1em[1]}, Mass -> Heavy,
UFO$Options -> <|"pdg" -> 24, "name" -> "W"|>];
```

Next, the physical Higgs field

```
In[11]:= DefineField[h, Scalar, SelfConjugate -> True, Mass -> Heavy,
UFO$Options -> <|"pdg" -> 25|>];
```

And lastly, the fermionic fields

```
In[12]:= DefineField[u, Fermion, Indices -> {SU3c[fund], Flavor},
Charges -> {U1em[+2/3]}, Mass -> Heavy];
DefineField[d, Fermion, Indices -> {SU3c[fund], Flavor},
Charges -> {U1em[-1/3]}, Mass -> Heavy];
DefineField[e, Fermion, Indices -> {Flavor}, Mass -> Heavy,
Charges -> {U1em[-1]}];
DefineField[nu, Fermion, Indices -> {Flavor}, Mass -> Heavy,
Chiral -> LeftHanded];
```

As mentioned before, we also need to define the  $\tilde{S}_1$  in the broken phase:

```
In[13]:= DefineField[S1, Scalar, Indices -> {SU3c[fund]},
Charges -> {U1Y[-4/3]}, UFO$Options -> <|"pdg" -> "90023"|>,
Mass -> {Heavy, MS1t}];
```

where we have set the mass to `MS1t`, which is equal to `MS1` as the leptoquark mass is not affected by symmetry breaking. With all the necessary fields after EWSB defined, we explain how the original fields in the unbroken phase decompose into those defined above. For that, we first set how the SM gauge groups are broken. As the  $SU(2)_L \times U(1)_Y$  is broken into  $U(1)_{\text{em}}$ , we use the MATCHETE routine `SetSymmetryBreaking`:

```
In[14]:= SetSymmetryBreaking[
{SU2L, U1Y},
{U1em}
]
```

Additionally, we define how the respective representations of  $SU(2)_L$  are broken using:

```
In[15]:= RepresentationDecomposition[SU2L[adj],
{ComplexSinglet, ComplexSinglet, Singlet}];
RepresentationDecomposition[SU2L[fund], {Singlet, Singlet}];
```

The adjoint representation of  $SU(2)_L$  is three-dimensional (one gauge field for each generator). After electroweak symmetry breaking,  $SU(2)_L \times U(1)_Y \rightarrow U(1)_{\text{em}}$ , and the  $SU(2)_L$  triplet of gauge fields  $W_\mu^a$  must decomposes into  $U(1)_{\text{em}}$  charge eigenstates. Of those eigenstates, one is a complex singlet and the other one a singlet:

$$W_\mu^\pm \equiv \frac{W_\mu^1 \mp i W_\mu^2}{\sqrt{2}} \quad \text{and} \quad W_\mu^3.$$

Regarding their  $U(1)_{\text{em}}$  charge,  $Q_{W^\pm}$  has  $\pm 1$  and  $Q_{W_\mu^3}$  is charge neutral. While  $W_\mu^\pm$  are mass eigenstates, the  $W_\mu^3$  is not: it mixes with the hypercharge gauge field  $B_\mu$ . Introducing the mass eigenstates  $Z_\mu$  and the photon  $A_\mu$ , we can write

$$W_\mu^3 = \frac{g_L}{g_Z} \cos \theta Z_\mu + \frac{g_L}{e} \sin \theta A_\mu \quad (\text{B.1})$$

$$\text{and} \quad B_\mu = -\frac{g_Y}{g_Z} \sin \theta Z_\mu + \frac{g_Y}{e} \cos \theta A_\mu, \quad (\text{B.2})$$

with  $g_L$  the  $SU(2)_L$  and  $g_Y$  the  $U(1)_Y$  coupling. Then starting with  $W_\mu^I$ , its decomposition in MATCHETE is done using

```
In[16]:= FieldDecomposition[W[\mu, a], {Bar@W[\mu], W[\mu], (cθ*Z[\mu]/gZ[] + sθ*A[\mu]/ge[])*gL[]}];
```

Here  $\text{Bar}@W[\mu]$  corresponds to the  $W^-$  and  $W[\mu]$  to  $W^+$ . The third component is Equation (B.1). For  $B_\mu$ , we decompose it according to Equation (B.2)

```
In[17]:= FieldDecomposition[B[\mu], {(-sθ*Z[\mu]/gZ[] + cθ*A[\mu]/ge[])*gY[]}];
```

Next, to decompose the matter fields, we keep in mind that each component transforms as a singlet as well. We start with the quarks and leptons:

```
In[18]:= FieldDecomposition[q[a, i, p], {CKM[p, r] * u[a, r], d[a, p]}];
FieldDecomposition[u[a, p], {u[a, p]}];
FieldDecomposition[d[a, p], {d[a, p]}];
FieldDecomposition[l[i, p], {ν[p], e[p]}];
FieldDecomposition[e[p], {e[p]}];.
```

Even though this step was straightforward, it is worth noting that we have placed the  $V_{\text{CKM}}$  into the first component of the quark doublet, thereby eliminating the CKM matrix in the down sector. Additionally, the gothic letters signal that we are now using the particles in their broken phase.  $a$  corresponds to the color index,  $p$  to the flavor index.  $i$  corresponds to the  $SU(2)_L$  index and therefore omitted after field decomposition. Next, after EWSB, the Higgs boson in the unitary gauge is given by

$$H(x) = \frac{1}{\sqrt{2}} \begin{pmatrix} 0 \\ v + h(x) \end{pmatrix}, \quad (\text{B.3})$$

which can be implemented via

```
In[19]:= FieldDecomposition[H[i], {0, (v[] + h[])/Sqrt[2]}];
```

Even though we have decomposed the fields, we have not yet defined the fundamental generators in the charge eigenstate basis. For fields that transform in the fundamental representation of  $SU(2)_L$ , such as the Higgs doublet or the left-handed lepton and quark doublets, the generators can be represented as  $2 \times 2$  matrices. Following the same definition used for the adjoint representation, we write them as

$$T^+ = \frac{1}{\sqrt{2}} \begin{pmatrix} 0 & 1 \\ 0 & 0 \end{pmatrix}, \quad T^- = \frac{1}{\sqrt{2}} \begin{pmatrix} 0 & 0 \\ 1 & 0 \end{pmatrix}, \quad T^3 = \frac{1}{2} \begin{pmatrix} 1 & 0 \\ 0 & -1 \end{pmatrix}. \quad (\text{B.4})$$

The corresponding implementation in MATCHETE using the CGDecomposition routine is

```
In[20]:= CGDecomposition[
  CG[gen@SU2L@fund, {J, i, j}],
  Normal@SparseArray[{
    {1, 1, 2} -> +(1/Sqrt[2]) (*T+*),
    {2, 2, 1} -> +(1/Sqrt[2]) (*T-*),
    {3, 1, 1} -> +(1/2),
    {3, 2, 2} -> -(1/2) (*T3*)
  }]
];
```

```
In[21]:= Matchete`SSB`PackagePrivate`AddFStructDecomposition[SU2L, SU2L@fund];
```

The indices  $\{J, i, j\}$  correspond to the generator  $T^J$ 's matrix element  $(i, j)$ .

With the same logic, we define the epsilon tensor  $\epsilon_{ij}$  of  $SU(2)$  using

```
In[22]:= CGDecomposition[
  CG[eps@SU2L, {i, j}],
  Normal@SparseArray[
    {{1, 2} -> +1,
     {2, 1} -> -1
    }]];
];
```

Finally, we will break both the BSM and EFT Lagrangians

```
In[23]:=  $\mathcal{L}_{\text{BSM}}\$ \text{BrokenPhase} = \text{BrokenPhase}[\mathcal{L}_{\text{BSM}}];$ 
```

Additionally, using `Matchete`SSB`PackagePrivate`PrepareLagrangianForMatching`, `ReplaceEffectiveCouplings`, `GreensSimplify` enable us to bring the Lagrangians into a form suitable for further analysis.

**Note** The steps in this section are universal for all BSM models in which the BSM particle transformation is trivial under  $SU(2)_L$ . If the BSM physics includes non-trivial additions, such as a heavy Higgs, we will need to redefine the field decompositions.

## B.2 EWSB in the Standard Model EFT

In the case above, we have seen the implementation of EWSB for the  $\tilde{S}_1$  in MATCHETE. However, if working with SMEFT, EWSB involves a more complicated implementation. In Alonso *et al.* [32], as well as Dedes *et al.* [29], the general procedure for EWSB in SMEFT was outlined. Here we follow the convention used in [29] to implement EWSB for SMEFT at dimension 6. We start by importing the predefined SMEFT into our notebook

```
In[2]:=  $\mathcal{L}_{\text{SMEFT}} = \text{LoadModel}["\text{SMEFT}"]$ 
```

In the previous section, we first defined the fields and the group decomposition. Since SMEFT shares the same symmetries as the SM, these steps remain unchanged. However, by including higher-order terms, the Higgs field obtains a different vacuum expectation value. This stems from the fact that the Higgs potential  $V(H)$  is governed by

$$V(H) = \lambda \left( H^\dagger H - \frac{1}{2} v^2 \right)^2 - C_H \left( H^\dagger H \right)^3, \quad (\text{B.5})$$

yielding a new minimum at

$$\frac{v_T}{\sqrt{2}} \equiv \sqrt{\frac{2\mu^2}{\lambda}} + 3 \frac{\mu^3}{\sqrt{2}\lambda^{5/2}} C_H. \quad (\text{B.6})$$

Additionally, SMEFT operators modify the Higgs kinetic structure:

$$\mathcal{L}_{\text{Higgs, Kin.}} = (D_\mu H^\dagger)(D^\mu H) + C_{H\square} (H^\dagger H) \square (H^\dagger H) + C_{HD} (H^\dagger D^\mu H)^* (H^\dagger D_\mu H). \quad (\text{B.7})$$

Thus, after EWSB, the kinetic term is not canonical. Restoring canonical normalisation requires a field redefinition of the physical Higgs as follows:

$$H = \frac{1}{\sqrt{2}} \begin{pmatrix} 0 \\ [1 + c_{H,\text{kin}}] h + v_T \end{pmatrix}, \quad \text{with } c_{H,\text{kin}} \equiv \left( C_{H\square} - \frac{1}{4} C_{HD} \right) v^2. \quad (\text{B.8})$$

In MATCHETE , with  $\text{cHkin} = c_{H,\text{kin}}$  and  $\text{vT} = v_T$ , the decomposition is implemented via:

```
In[18]:= FieldDecomposition[H[i], {0, ((1+cHkin)*h[] + vT)/Sqrt[2]}]
```

Next, we turn to the gauge fields. As there are operators of type  $F_{\mu\nu}^2 H^\dagger H$ , the constant contributions  $F_{\mu\nu}^2 v_T^2 / 2$  lead to shifts in the kinetic terms. We illustrate this using the example of the kinetic terms of the gluon

$$\mathcal{L}_{\text{Kinetic, Gluon}} = -\frac{1}{4} \frac{1}{g_s^2} G_{\mu\nu}^A G^{A\mu\nu} + \frac{1}{2} \frac{1}{g_s^2} v_T^2 C_{HG} G_{\mu\nu}^A G^{A\mu\nu}. \quad (\text{B.9})$$

As the kinetic terms are no longer canonical, we redefine the coupling to get canonical kinetic terms. To this end, we do the following replacement:

$$g_s \rightarrow (1 - C_{HG} v_T^2) g_s. \quad (\text{B.10})$$

This does not alter the underlying physics, since the fields are defined to incorporate the coupling. As long as the physical interactions between particles are not redefined, the physics remains the same.<sup>2</sup> Similar replacement rules are done for the  $B_\mu$  and  $W_\mu^I$  bosons. Already in the SM, the electroweak sector mixes  $W_{\mu\nu}^3$  and  $B_{\mu\nu}$ , leading to the  $Z$  and  $A$  bosons in the mass eigenstates. In SMEFT, we want to achieve the same by going into a mass basis for the following electroweak Lagrangian:

$$\begin{aligned} \mathcal{L}_{\text{EW}} = & -\frac{1}{2} \frac{1}{g_L^2} W_{\mu\nu}^+ W_-^{\mu\nu} - \frac{1}{4} \frac{1}{g_L^2} W_{\mu\nu}^3 W_3^{\mu\nu} - \frac{1}{4} \frac{1}{g_Y^2} B_{\mu\nu} B^{\mu\nu} - \frac{1}{2} \frac{1}{g_Y g_L} (v_T^2 C_{HWB}) W_{\mu\nu}^3 B^{\mu\nu} \\ & + \frac{1}{4} v_T^2 W_\mu^+ W_-^{-\mu} + \frac{1}{8} v_T^2 (W_\mu^3 - B_\mu)^2 + \frac{1}{16} v_T^4 C_{HD} (W_\mu^3 - B_\mu)^2. \end{aligned} \quad (\text{B.11})$$

In SMEFT, the rotation required to go into mass eigenstates necessitates additional steps. In the end, we still want to obtain a massless boson  $A_\mu$  and a massive boson  $Z_\mu$ . To this end, we define the linear transformation  $N$  with

$$\begin{bmatrix} W_\mu^3 \\ B_\mu \end{bmatrix} = N \begin{bmatrix} Z_\mu \\ A_\mu \end{bmatrix},$$

As pointed out in [33], the matrix to go into eigenstates for SMEFT is a product of a rotation, a rescaling, and a second rotation. In [33] and [32], the couplings were explicit; therefore, in our implementation, the couplings have to be taken care of explicitly. This leaves us with

$$N = \begin{bmatrix} g_L & 0 \\ 0 & g_Y \end{bmatrix} \begin{bmatrix} 1 & -\frac{1}{2} v_T^2 C_{HWB} \\ -\frac{1}{2} v_T^2 C_{HWB} & 1 \end{bmatrix} \begin{bmatrix} \cos \bar{\theta} & \sin \bar{\theta} \\ -\sin \bar{\theta} & \cos \bar{\theta} \end{bmatrix} \begin{bmatrix} \frac{1}{g_Z} & 0 \\ 0 & \frac{1}{e} \end{bmatrix},$$

---

<sup>2</sup>This is in contrast to the definitions used in [29] and [32], where the coupling is written explicitly. In that case, a redefinition of the field and couplings is necessary.

where  $\bar{\theta}$  is given by

$$\tan \bar{\theta} = \frac{g_Y}{g_L} + \frac{v_T^2}{2} C_{HWB} \left[ 1 - \frac{g_Y^2}{g_L^2} \right].$$

This way, the neutral vector fields are given by

$$\begin{aligned} \text{W3Field} &= W_\mu^3 = \frac{1}{e} \left( g_L \sin \bar{\theta} - \frac{1}{2} v_T^2 g_L C_{HWB} \cos \bar{\theta} \right) A_\mu + \frac{1}{g_Z} \left( g_L \cos \bar{\theta} + \frac{1}{2} v_T^2 g_L C_{HWB} \sin \bar{\theta} \right) Z_\mu \\ \text{BField} &= B_\mu = \frac{1}{e} \left( g_Y \cos \bar{\theta} - \frac{1}{2} v_T^2 g_Y C_{HWB} \sin \bar{\theta} \right) A_\mu - \frac{1}{g_Z} \left( g_Y \sin \bar{\theta} - \frac{1}{2} v_T^2 g_Y C_{HWB} \cos \bar{\theta} \right) Z_\mu \end{aligned}$$

In MATCHETE, then the gauge fields are therefore decomposed as

```
In[19]:= FieldDecomposition[W[\mu], a], {Bar@W[\mu], W[\mu], W3Field}];  
FieldDecomposition[B[\mu], {BField}];
```

With these decompositions and redefinitions complete, we follow the same steps as in the previous section. Lastly, by keeping only terms up to mass dimension  $d = 6$ , we are left with the SMEFT Lagrangian in the broken phase.

## B.3 Generating the UFO Files

For this project, my co-worker Luis Hourtz and I independently implemented two codes to derive Feynman rules from a given Lagrangian. My co-worker developed the routine to export to the UFO format required by MG5. At the same time, I performed cross-checks by comparing cross sections from both implementations with those from the literature [29]. In parallel, I extended the EWSB functionality in MATCHETE to support the BSM models and added an option for SMEFT. Because these steps were cumbersome and offered limited conceptual insight, we split the workload accordingly. In what follows, I use the routine my co-worker wrote to create the UFO files.

For the UFO generation, we work in the mass basis and explicitly expand all flavour indices in the Lagrangian using the **DiagonaliseBrokenLagrangian** routine.

Additionally, we set a coupling-order hierarchy to suppress unwanted channels in simulations using the **DefineCouplingOrder** routine. We establish the hierarchy so that NP is dominant, followed by QCD, and QED last. Finally, we generate the UFO with

```
In[20]:= WriteToUFO[L, InputFile -> file]
```

where **L** is the Lagrangian and **file** is a .json specifying particles and parameters. The MATHEMATICA notebook used to implement, match, and export the BSM model into the UFO format is available in my [GitHub repository](#).



## Appendix C

# Scalar Leptoquark $\tilde{S}_1$ : EFT and BSM convergence

In this Appendix, we present additional simulation results for Section 4.

In Appendix C.1 we provide additional plots for the process  $pp \rightarrow \tau^+ \tau^-$ , for  $\lambda_t = 1.7$  and 2.5. Figure C.1 shows total cross sections. Figure C.2 gives the relative deviations for EFT truncated at dimension 6 and dimension 8. In Figure C.3 we provide an enlarged view of the deviations.

In Appendix C.2, we present the supplementary plots for the process  $pp \rightarrow \tau^+ \tau^- b$ . Figure C.4-C.6 show, for each topology from Section 4.4, the total cross sections and EFT deviations at  $\lambda_t = 1.7, 2.5$ . Finally, Figure C.7 presents the combined  $pp \rightarrow \tau^+ \tau^- b$  cross sections (all three topologies including interferences) and the corresponding relative deviations for  $\lambda_t = 1.7$  and 2.5.

## C.1 Hadronic Interaction without a final $b$ -quark: $pp \rightarrow \tau^+ \tau^-$

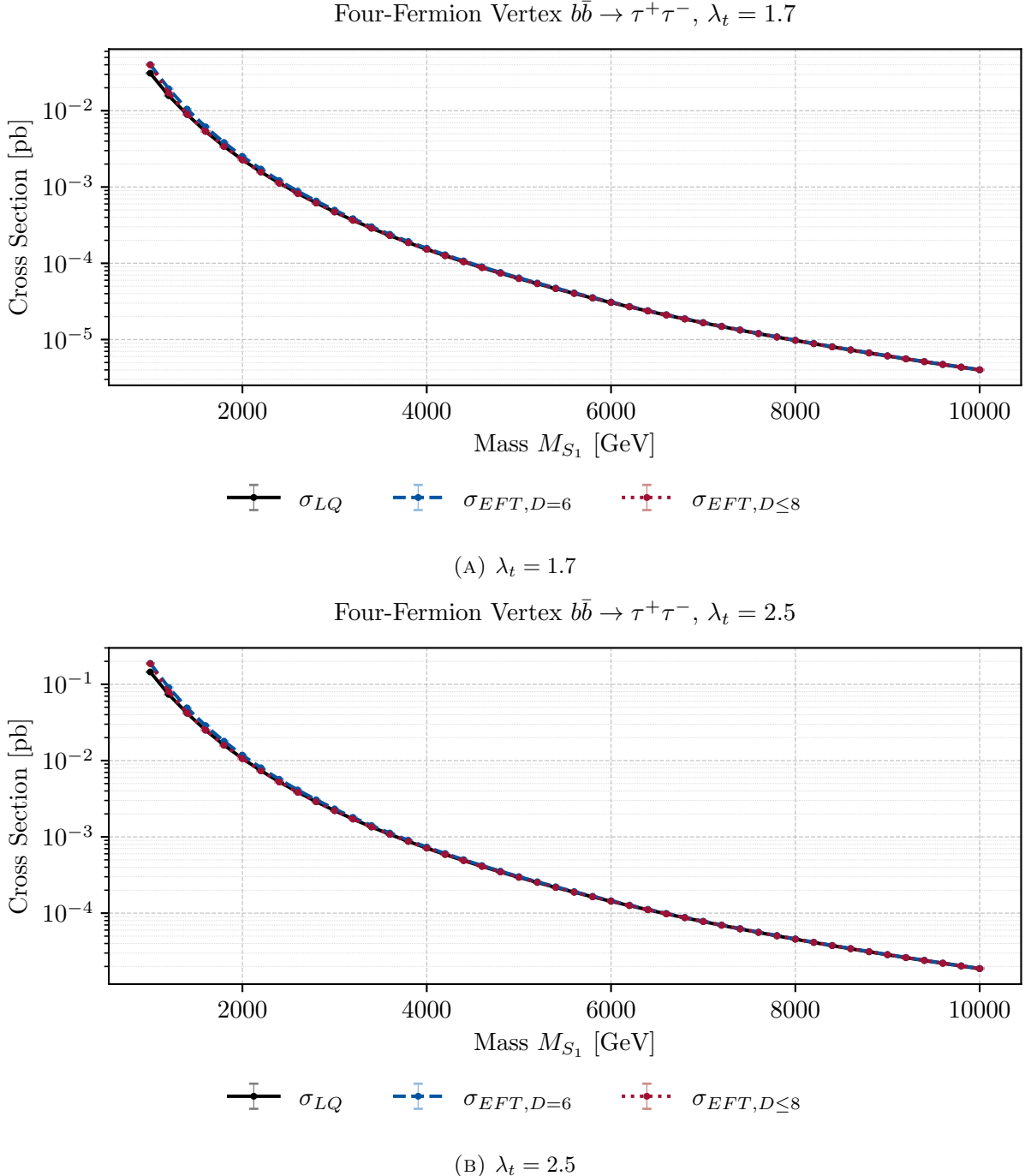


FIGURE C.1: Figure 4.4 for different  $\lambda_t$ . Comparison of  $\sigma(b\bar{b} \rightarrow \tau^+ \tau^-)$  in full BSM theory (black) and in EFT at  $D = 6$  (blue) and  $D \leq 8$  (red). Results are shown for leptoquark masses between 1 and 10 TeV.

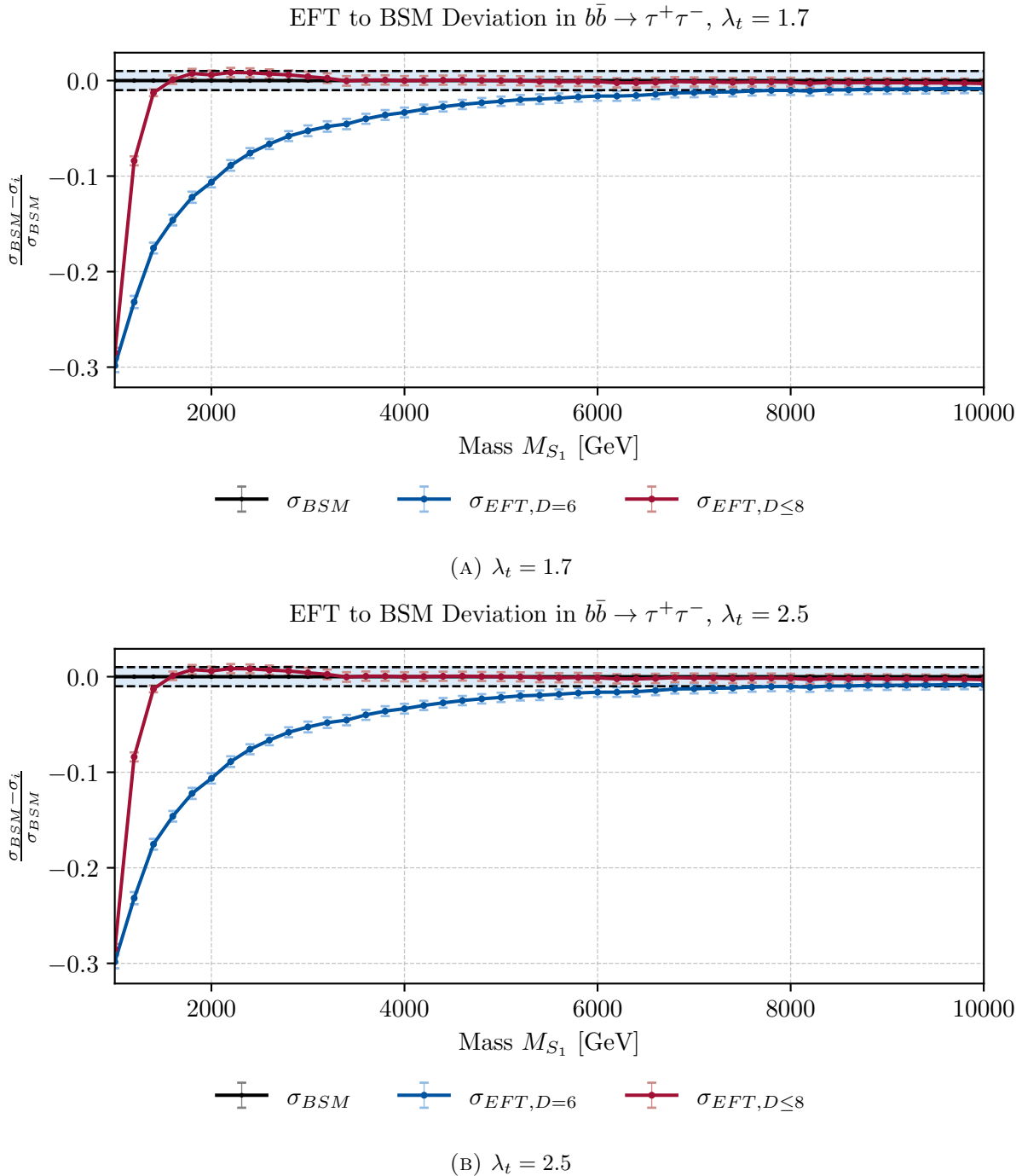


FIGURE C.2: Figure 4.15 for different  $\lambda_t$ . Relative deviation of the EFT predictions with respect to the full BSM theory, for  $\lambda_t = 1.7$  and 2.5. The blue area indicates a deviation below 1%.

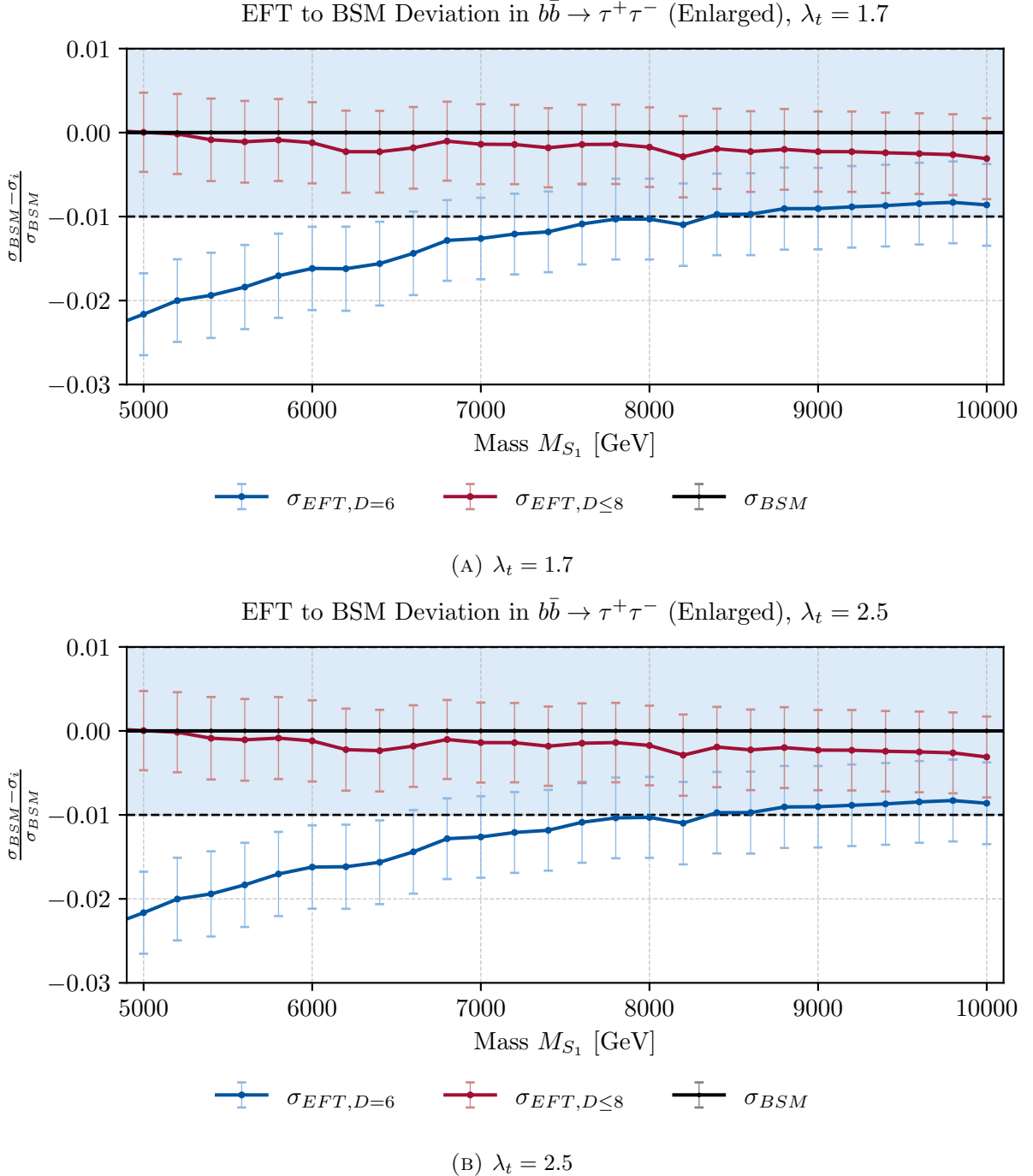


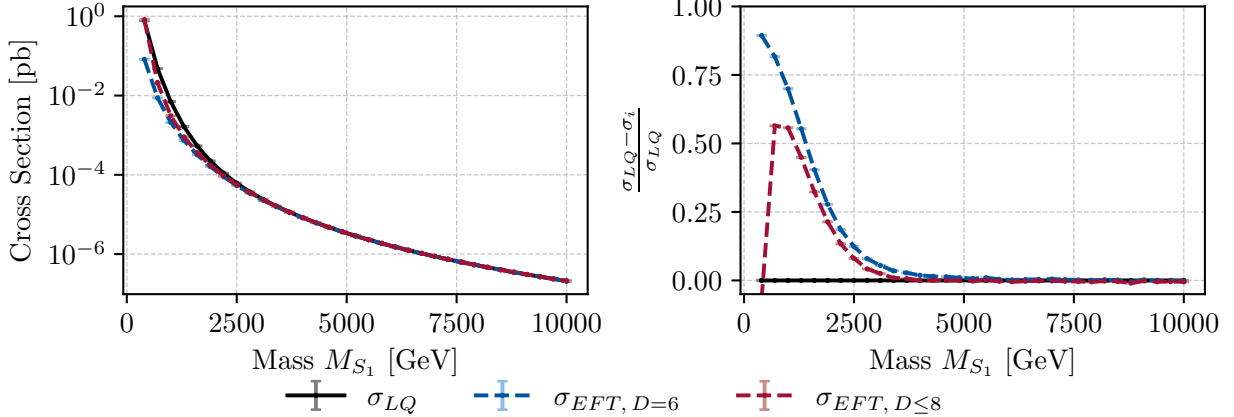
FIGURE C.3: Figure 4.15 for different  $\lambda_t$ . Relative deviation of the EFT predictions with respect to the full BSM theory for  $\lambda_t = 1.7$  and  $2.5$ . The blue band indicates the  $\pm 1\%$  accuracy interval.

## C.2 Hadronic Interaction with one final state $b$ -quark:

$$pp \rightarrow \tau^+ \tau^- b$$

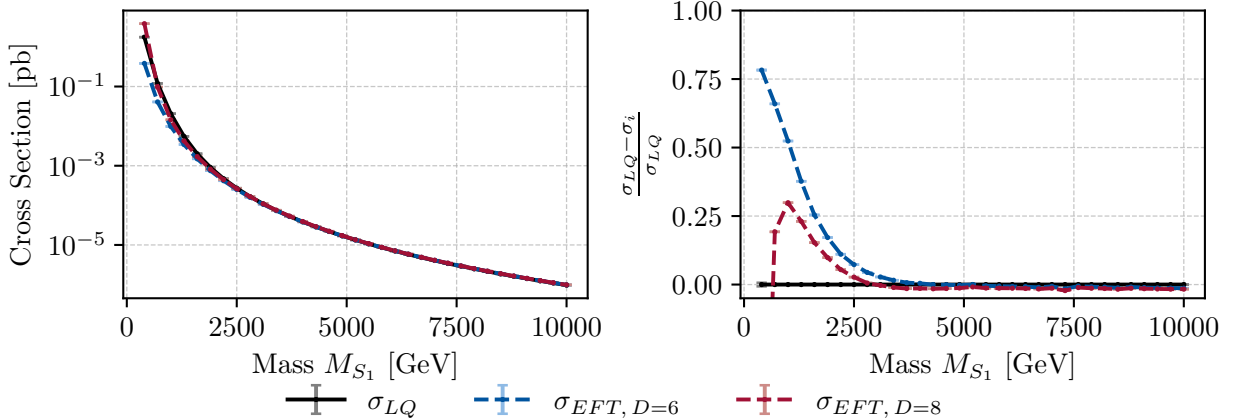
**Cross-Section of the Individual Processes -  $\lambda_t = 1.7$  and 2.5**

Diagram: 1,  $\lambda_t = 1.7$



(A) Diagram 1, with  $\lambda_t = 1.7$ .

Diagram: 1,  $\lambda_t = 2.5$



(B) Diagram 1, with  $\lambda_t = 2.5$ .

FIGURE C.4: Cross section for diagram in Figure 4.13a for different  $\lambda_t$ . On the left side, the absolute cross sections as a function of the leptoquark mass  $M_{S_1}$  for the BSM model  $\sigma_{LQ}$  and EFT at order  $D = 6$  and  $D \leq 8$ . On the right, the relative deviation  $\frac{\sigma_{LQ} - \sigma_i}{\sigma_{LQ}}$  for both EFT orders with respect to the full theory.

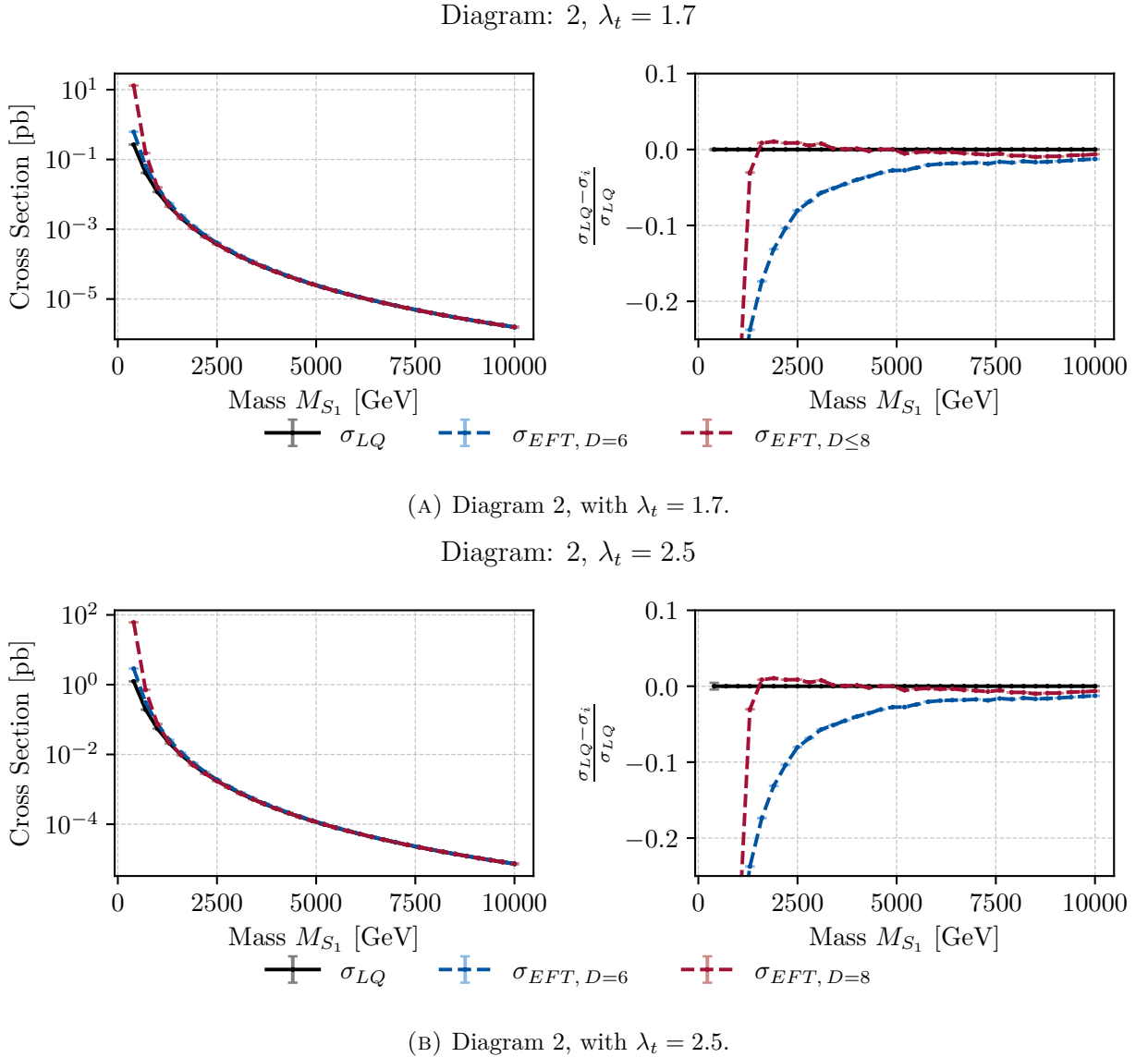


FIGURE C.5: Cross section for diagram in Figure 4.13b for different  $\lambda_t$ . On the left side, the absolute cross sections as a function of the leptoquark mass  $M_{S_1}$  for the BSM model  $\sigma_{LQ}$  and EFT at order  $D = 6$  and  $D \leq 8$ . On the right, the relative deviation  $\frac{\sigma_{LQ} - \sigma_i}{\sigma_{LQ}}$  for both EFT orders with respect to the full theory.

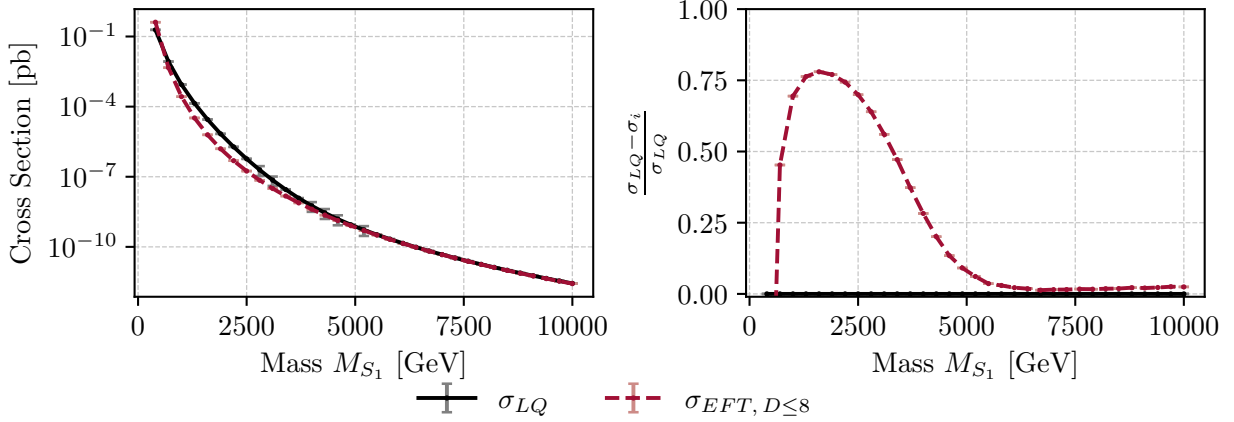
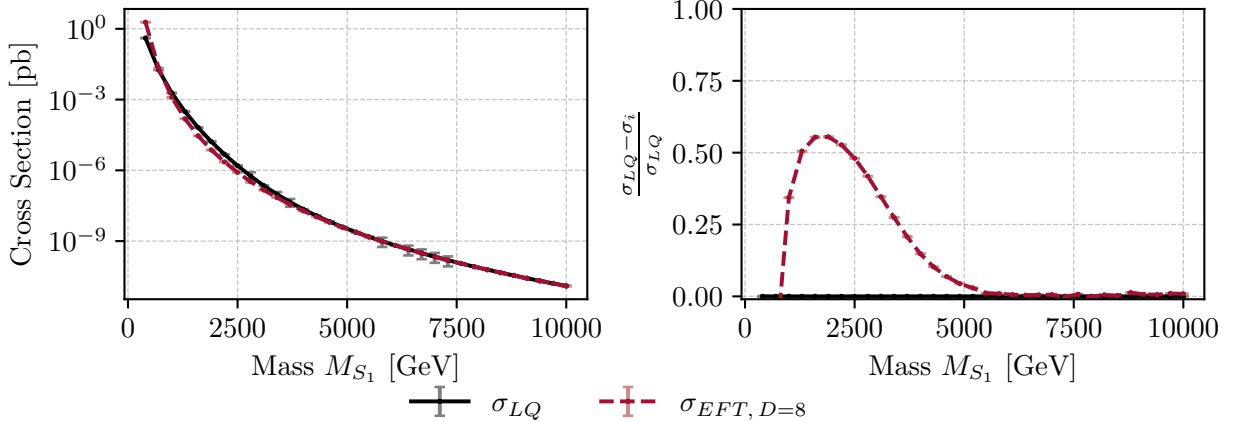
Diagram: 3,  $\lambda_t = 1.7$ (A) Diagram 3, with  $\lambda_t = 1.7$ .Diagram: 3,  $\lambda_t = 2.5$ (B) Diagram 3, with  $\lambda_t = 2.5$ .

FIGURE C.6: Cross section for diagram in Figure 4.13c for different  $\lambda_t$ . On the left side, the absolute cross sections as a function of the leptoquark mass  $M_{S_1}$  for the BSM model  $\sigma_{LQ}$  and EFT at order  $D = 6$  and  $D \leq 8$ . On the right, the relative deviation  $\frac{\sigma_{LQ} - \sigma_i}{\sigma_{LQ}}$  for both EFT orders with respect to the full theory.

### Total Cross-Section of $pp \rightarrow \tau^+ \tau^- b$

We now combine all three topologies, including their interferences, to obtain the full  $pp \rightarrow \tau^+ \tau^- b$  prediction in BSM and EFT:

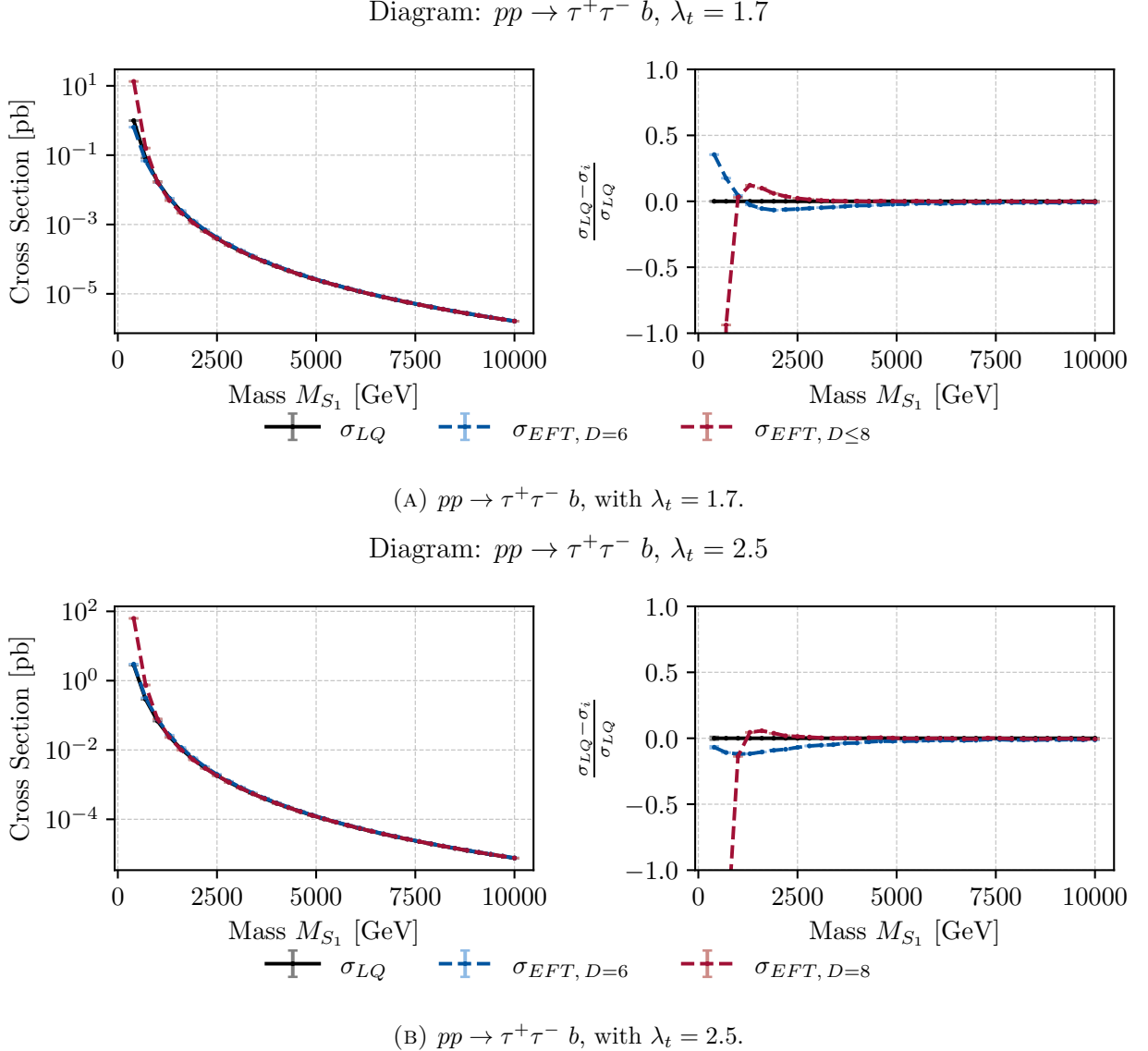


FIGURE C.7: Figure 4.15 for different  $\lambda_t$ . Comparison of cross sections for the hadronic process  $pp \rightarrow \tau^+ \tau^- b$ . On the left side, the absolute cross sections as a function of the leptoquark mass  $M_{S_1}$  for the BSM model  $\sigma_{LQ}$  and EFT at order  $D = 6$  and  $D \leq 8$ . On the right, the relative deviation  $\frac{\sigma_{LQ} - \sigma_i}{\sigma_{LQ}}$  for both EFT orders with respect to the full theory.

## Appendix D

# Numerical Stability of Monte Carlo Simulations

In this section, we evaluate the numerical stability of the  $pp \rightarrow \tau^+ \tau^-$  simulations. We assess how random seeds and event counts impact the EFT-BSM convergence shown in Chapter 4. In the analysis, we have set the random seed to 30 and generated  $N = 10.000$  events. Here, we vary the random seed and the number of events while keeping all other settings fixed as in Tables 4.2 and 4.3. Deviations are given relative to the seed 30 as

$$\Delta\sigma/\sigma \equiv \frac{\sigma_{\text{seed}} - \sigma_{30}}{\sigma_{30}}, \quad (\text{D.1})$$

and are shown separately for the BSM, the EFT truncated at dimension 6, and truncated at dimension 8.

Figures D.1-D.3 show the deviation for seeds 78 and 95.<sup>1</sup> For the EFTs, deviations remain below 2% across the mass range, indicating small seed-induced fluctuations. In contrast, for the BSM samples, the deviation grows with  $M_{\tilde{S}_1}$  and reaches about 4% for seed 78 at high masses. To exclude a model-file issue, Figure D.1 also includes results generated with the Dorsner *et al.* UFO model [6], which shows the same behaviour.

Because these seed-dependent fluctuations of a few percent are of same order as the BSM-EFT deviations from Figure 4.15, we also show the EFT-BSM ratio for different seeds in Figure D.4. In this case, the deviation plots do not follow a smooth curve and are prone to bumps. This implies that, to draw conclusions about convergence with accuracies below a few percent, we must be cautious about Monte Carlo uncertainties. Particularly for high LQ masses  $M_{\tilde{S}_1}$  or for very small cross sections  $\sigma$ , numerical issues will affect the convergence. To reduce statistical effects, in Figure D.5 we increase the event count from 10.000 to 20.000. Since the Monte Carlo error scales approximately as  $1/\sqrt{N}$ , to reduce a 4% fluctuation to 2% needs 40.000, and to 1% 160.000 events.

Finally, we note that this behaviour is setup-dependent. This issue does not arise on all PCs.

---

<sup>1</sup>We selected these seeds at random.

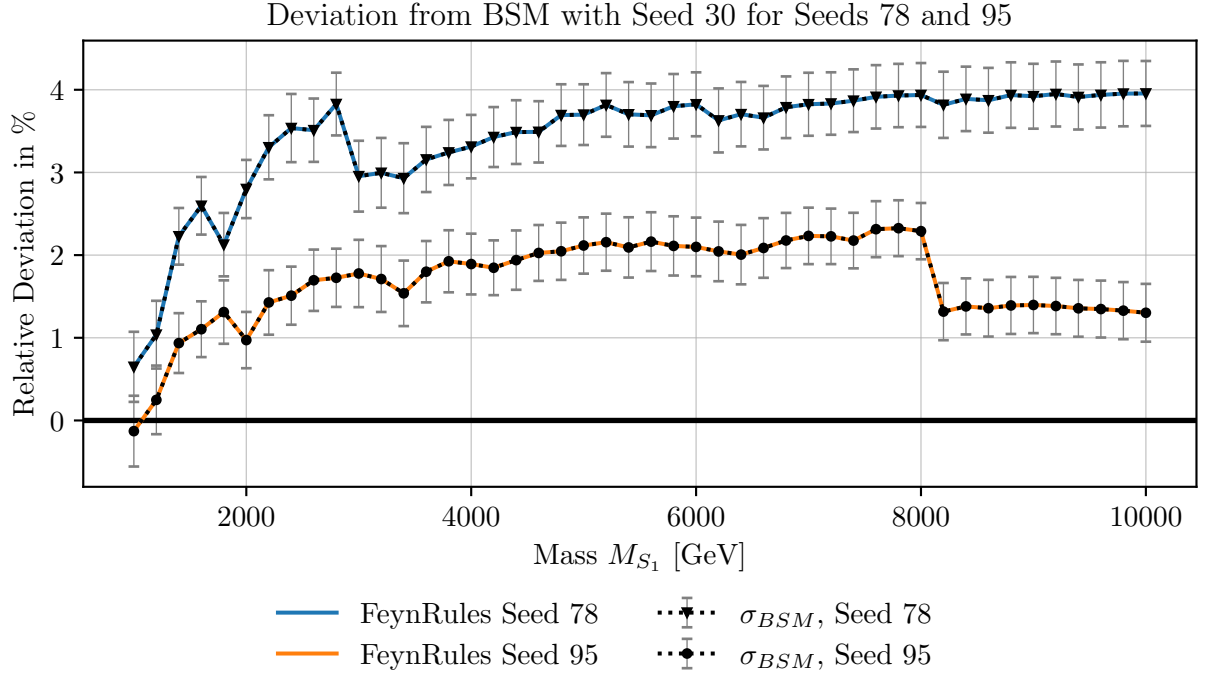


FIGURE D.1: Deviation of the BSM  $pp \rightarrow \tau^+\tau^-$  cross section obtained with random seeds 78 and 95, relative to the BSM prediction with seed 30.

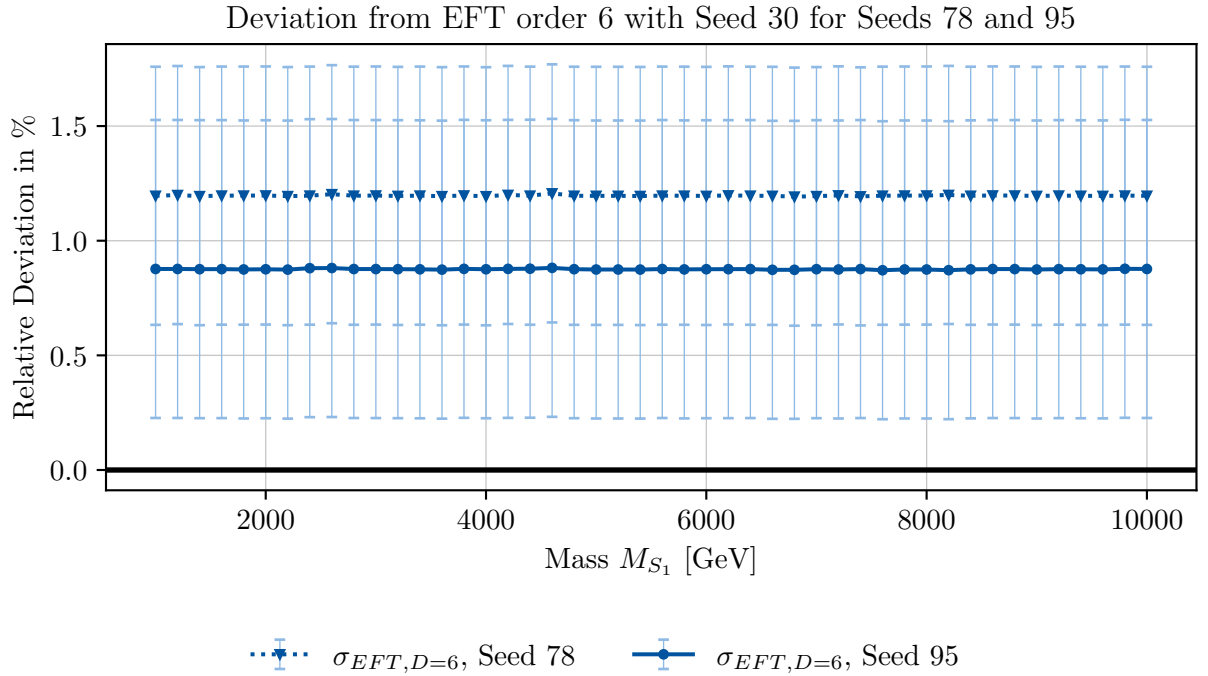


FIGURE D.2: Deviation of the EFT (dimension 6)  $pp \rightarrow \tau^+\tau^-$  cross section obtained with random seeds 78 and 95, relative to the EFT (dimension 6) prediction with seed 30.

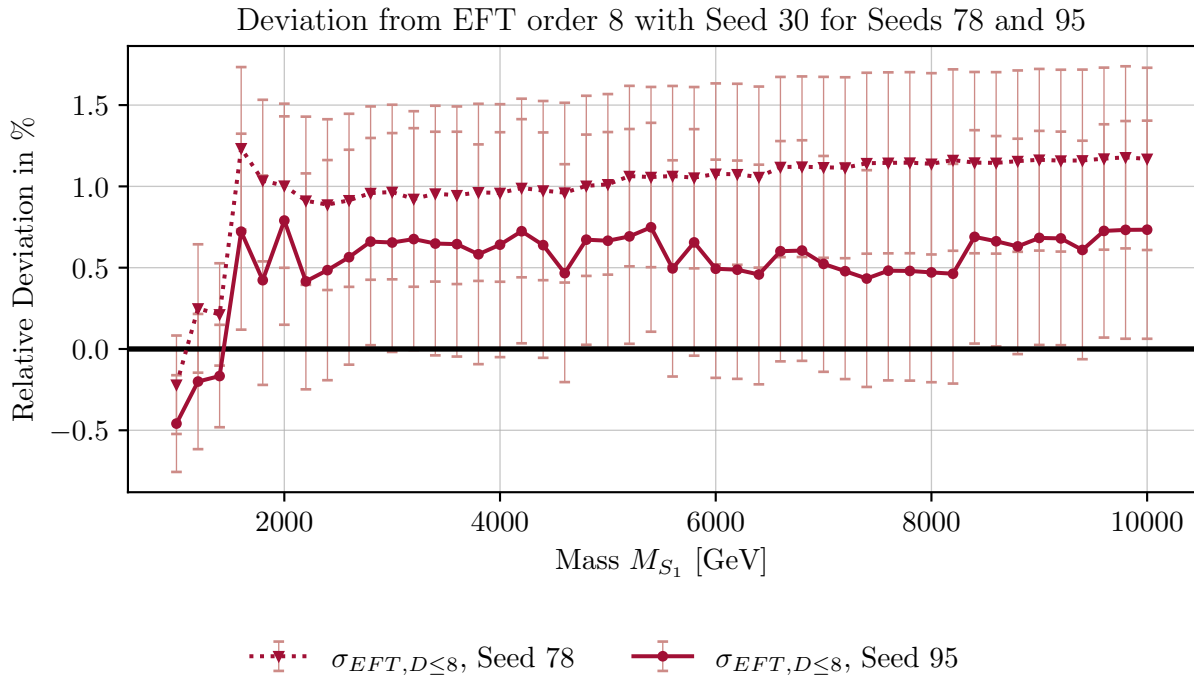


FIGURE D.3: Deviation of the EFT (dimension 8)  $pp \rightarrow \tau^+ \tau^-$  cross section obtained with random seeds 78 and 95, relative to the EFT (dimension 8) prediction with seed 30.

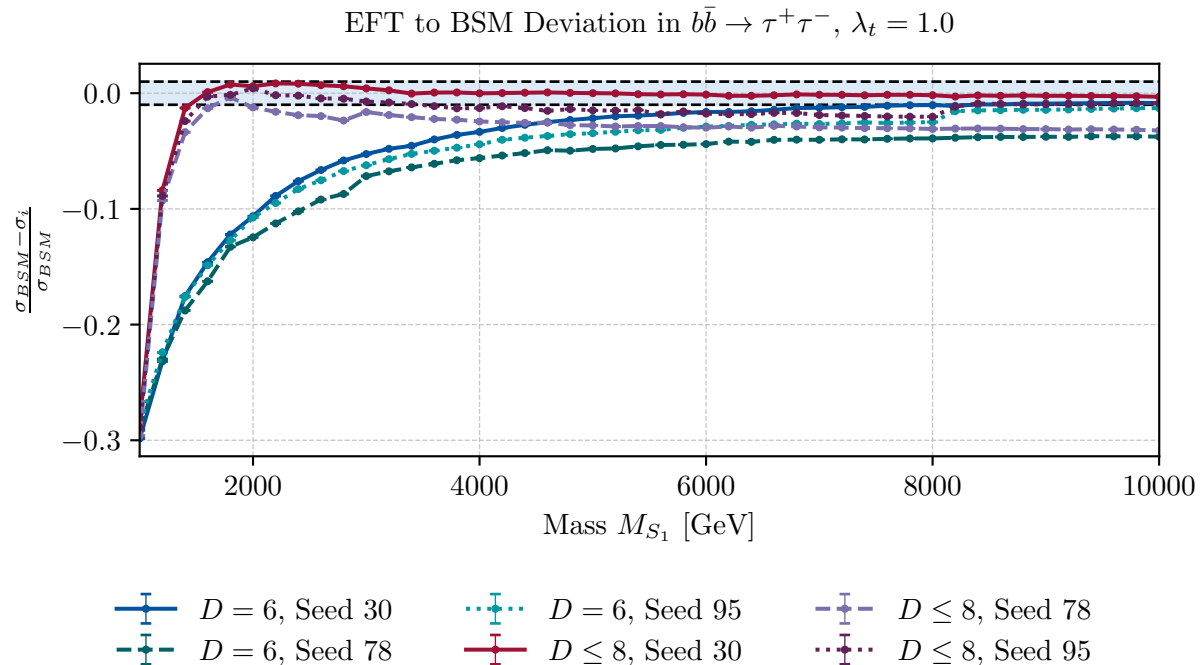


FIGURE D.4: Relative deviation of the EFT predictions with respect to the full BSM theory, for different seeds (30, 78, 95)

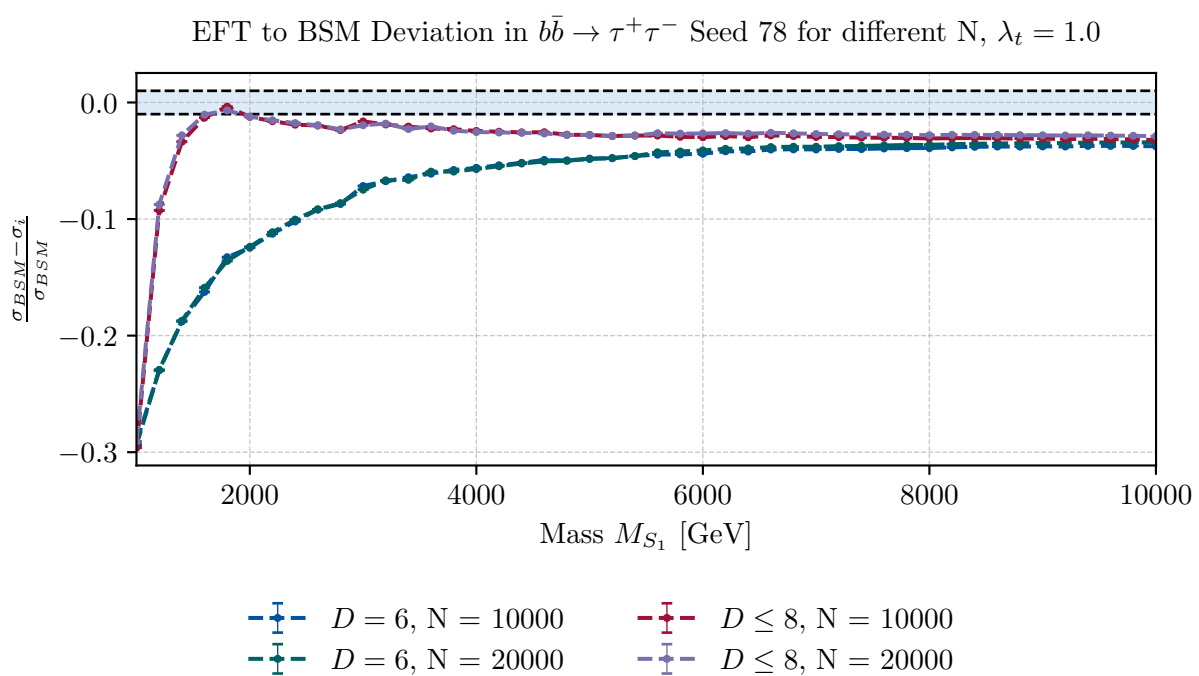


FIGURE D.5: Deviation of the cross section for Seed 78 with Number of Events 10000 and 20000.

# Bibliography

- <sup>1</sup>J. Alwall, R. Frederix, S. Frixione, V. Hirschi, F. Maltoni, O. Mattelaer, H.-S. Shao, T. Stelzer, P. Torrielli, and M. Zaro, “The automated computation of tree-level and next-to-leading order differential cross sections, and their matching to parton shower simulations”, *Journal of High Energy Physics* **2014**, [10.1007/jhep07\(2014\)079](https://doi.org/10.1007/jhep07(2014)079) (2014).
- <sup>2</sup>V. Hirschi and O. Mattelaer, *Automated event generation for loop-induced processes*, 2015.
- <sup>3</sup>L. Darmé, C. Degrande, C. Duhr, B. Fuks, M. Goodsell, G. Heinrich, V. Hirschi, S. Höche, M. Höfer, J. Isaacson, O. Mattelaer, T. Ohl, D. Pagani, J. Reuter, P. Richardson, S. Schumann, H.-S. Shao, F. Siegert, and M. Zaro, “Ufo 2.0: the ‘universal feynman output’ format”, *The European Physical Journal C* **83**, [10.1140/epjc/s10052-023-11780-9](https://doi.org/10.1140/epjc/s10052-023-11780-9) (2023).
- <sup>4</sup>A. Alloul, N. D. Christensen, C. Degrande, C. Duhr, and B. Fuks, “FeynRules 2.0 — a complete toolbox for tree-level phenomenology”, *Computer Physics Communications* **185**, 2250–2300 (2014).
- <sup>5</sup>J. Fuentes-Martín, M. König, J. Pagès, A. E. Thomsen, and F. Wilsch, “A proof of concept for matchete: an automated tool for matching effective theories”, *The European Physical Journal C* **83**, [10.1140/epjc/s10052-023-11726-1](https://doi.org/10.1140/epjc/s10052-023-11726-1) (2023).
- <sup>6</sup>I. Doršner and A. Greljo, “Leptoquark toolbox for precision collider studies”, *Journal of High Energy Physics* **2018**, [10.1007/jhep05\(2018\)126](https://doi.org/10.1007/jhep05(2018)126) (2018).
- <sup>7</sup>M. E. Peskin and D. V. Schroeder, *An Introduction to quantum field theory* (Addison-Wesley, Reading, USA, 1995).
- <sup>8</sup>M. D. Schwartz, *Quantum Field Theory and the Standard Model* (Cambridge University Press, Mar. 2014).
- <sup>9</sup>C. P. Burgess, *Introduction to effective field theory: thinking effectively about hierarchies of scale* (Cambridge University Press, 2020).
- <sup>10</sup>A. Falkowski, *Lectures on effective field theory approach to physics: lecture 1*, Lecture notes, Karlsruhe Institute of Technology (KIT), KCETA / GRK 1694, Sept. 2015.
- <sup>11</sup>G. Isidori, F. Wilsch, and D. Wyler, “The standard model effective field theory at work”, *Reviews of Modern Physics* **96**, [10.1103/revmodphys.96.015006](https://doi.org/10.1103/revmodphys.96.015006) (2024).

- <sup>12</sup>S. Weinberg, “Baryon and Lepton Nonconserving Processes”, *Phys. Rev. Lett.* **43**, 1566–1570 (1979).
- <sup>13</sup>B. Grzadkowski, M. Iskrzyński, M. Misiak, and J. Rosiek, “Dimension-six terms in the standard model lagrangian”, *Journal of High Energy Physics* **2010**, 10.1007/jhep10(2010)085 (2010).
- <sup>14</sup>H. S. Reall and C. M. Warnick, “Effective field theory and classical equations of motion”, *Journal of Mathematical Physics* **63**, 10.1063/5.0075455 (2022).
- <sup>15</sup>A. Hebecker, *Quantum field theory ii: notes of lecture course*, <https://www.thphys.uni-heidelberg.de/~hebecker/QFTII/qft.html>, Lecture course SS 2016, 2016.
- <sup>16</sup>U. Nierste, *Flavour anomalies and new physics*, Talk at Bethe Center for Theoretical Physics, Bonn, Available at [https://indico.hiskp.uni-bonn.de/event/633/attachments/984/1816/nierste\\_bonn2024.pdf](https://indico.hiskp.uni-bonn.de/event/633/attachments/984/1816/nierste_bonn2024.pdf), May 2024.
- <sup>17</sup>M. Thomson, *Modern particle physics* (Cambridge University Press, New York, Oct. 2013).
- <sup>18</sup>G. M. Ciezarek, *First joint measurement of  $R(D^*)$  and  $R(D^0)$  at lhcb, LHC Seminar*, CERN, Council Chamber (503/1-001), CERN. Slides and recording available on the event page. Indico event #1187939, Geneva, Switzerland: CERN, Oct. 2022.
- <sup>19</sup>B. Capdevila, A. Crivellin, and J. Matias, “Review of semileptonic b anomalies”, *The European Physical Journal Special Topics* **233**, 409–428 (2023).
- <sup>20</sup>I. Doršner, S. Fajfer, A. Greljo, J. Kamenik, and N. Košnik, “Physics of leptoquarks in precision experiments and at particle colliders”, *Physics Reports* **641**, 1–68 (2016).
- <sup>21</sup>I. Doršner, S. Fajfer, and N. Košnik, “Heavy and light scalar leptoquarks in proton decay”, *Physical Review D* **86**, 10.1103/physrevd.86.015013 (2012).
- <sup>22</sup>G. Aad et al., “Search for leptoquarks decaying into the b final state in pp collisions at  $\sqrt{s} = 13$  tev with the atlas detector”, *Journal of High Energy Physics* **2023**, 10.1007/jhep10(2023)001 (2023).
- <sup>23</sup>R. D. Ball, V. Bertone, S. Carrazza, C. S. Deans, L. Del Debbio, S. Forte, A. Guffanti, N. P. Hartland, J. I. Latorre, J. Rojo, and M. Ubiali, “Parton distributions for the lhc run ii”, *Journal of High Energy Physics* **2015**, 10.1007/jhep04(2015)040 (2015).
- <sup>24</sup>A. Buckley, J. Ferrando, S. Lloyd, K. Nordstroem, B. Page, M. Ruefenacht, M. Schoenherr, and G. Watt, “Lhapdf6: parton density access in the lhc precision era”, *The European Physical Journal C* **75**, 10.1140/epjc/s10052-015-3318-8 (2015).
- <sup>25</sup>K. Ostrolenk and O. Mattelaer, *Speeding up MadGraph5\_aMC@NLO*, 2021.
- <sup>26</sup>J. Butterworth et al., “PDF4LHC recommendations for LHC Run II”, *J. Phys. G* **43**, 023001 (2016).

- <sup>27</sup>A. Denner, H. Eck, O. Hahn, and J. Kublbeck, “Feynman rules for fermion number violating interactions”, *Nucl. Phys. B* **387**, 467–481 (1992).
- <sup>28</sup>L. Allwicher, D. A. Faroughy, F. Jaffredo, O. Sumensari, and F. Wilsch, “HighPT: A Tool for high- $p_T$  Drell-Yan Tails Beyond the Standard Model”, (2022).
- <sup>29</sup>A. Dedes, W. Matherkowska, M. Paraskevas, J. Rosiek, and K. Suxho, “Feynman rules for the standard model effective field theory in  $r\xi$ -gauges”, *Journal of High Energy Physics* **2017**, 10.1007/jhep06(2017)143 (2017).
- <sup>30</sup>C. Itzykson and J. B. Zuber, *Quantum Field Theory*, International Series In Pure and Applied Physics (McGraw-Hill, New York, 1980).
- <sup>31</sup>A. Buckley, F. Krauss, S. Navas, P. Richardson, and P. D. Group), “Monte carlo particle numbering scheme”, *Progress of Theoretical and Experimental Physics* **2024**, Review in the 2024 edition of the Particle Data Group, 083C01 (2024).
- <sup>32</sup>R. Alonso, E. E. Jenkins, A. V. Manohar, and M. Trott, “Renormalization group evolution of the standard model dimension six operators iii: gauge coupling dependence and phenomenology”, *Journal of High Energy Physics* **2014**, 10.1007/jhep04(2014)159 (2014).
- <sup>33</sup>B. Grinstein and M. B. Wise, “Operator analysis for precision electroweak physics”, *Phys. Lett. B* **265**, 326–334 (1991).
- <sup>34</sup>A. Crivellin and L. Schnell, “Complete lagrangian and set of feynman rules for scalar leptoquarks”, *Computer Physics Communications* **271**, 108188 (2022).
- <sup>35</sup>J. Aebischer, G. Isidori, M. Pesut, B. A. Stefanek, and F. Wilsch, “Confronting the vector leptoquark hypothesis with new low- and high-energy data”, *The European Physical Journal C* **83**, 10.1140/epjc/s10052-023-11304-5 (2023).
- <sup>36</sup>L. Allwicher, D. A. Faroughy, F. Jaffredo, O. Sumensari, and F. Wilsch, “Drell-Yan Tails Beyond the Standard Model”, (2022).
- <sup>37</sup>A. Falkowski and R. Rattazzi, “Which eft”, *Journal of High Energy Physics* **2019**, 10 . 1007/jhep10(2019)255 (2019).
- <sup>38</sup>A. Hayrapetyan et al., “Search for a third-generation leptoquark coupled to a lepton and a b quark through single, pair, and nonresonant production in proton-proton collisions at  $\sqrt{s} = 13$  tev”, *Journal of High Energy Physics* **2024**, 10.1007/jhep05(2024)311 (2024).